NASA CONTRACTOR REPORT

NASA CR-2489

NASA CR-2489

ANALYTICAL COMPARISON OF HYPERSONIC FLIGHT AND WIND TUNNEL VISCOUS/INVISCID FLOW FIELDS

H. J. Fivel, R. V. Masek, and L. J. Mockapetris

Prepared by
MCDONNELL DOUGLAS ASTRONAUTICS COMPANY-EAST
St. Louis, Mo. 63166
for Langley Research Center

NATIONAL AERONAUTICS AND SPACE ADMINISTRATION • WASHINGTON, D. C. • FEBRUARY 1975

1. Report No.	2. Government Accession No.	3. Recipient's Catalog No.
NASA CR-2489		

4. Title and Subtitle	5. Report Date
ANALYTICAL COMPARISON OF HYPERSONIC FLIGHT AND WIND TUNNEL VISCOUS/INVISCID FLOW FIELDS	February 1975
	6. Performing Organization Code

7. Author(s)	8. Performing Organization Report No.
H. J. Fivel, R. V. Masek, and L. J. Mockapetris	
	10. Work Unit No.

9. Performing Organization Name and Address	11. Contract or Grant No.
McDonnell Douglas Astronautics Company-East St. Louis, Missouri 63166	NAS1-11728
	13. Type of Report and Period Covered
12. Sponsoring Agency Name and Address	Contractor Report
National Aeronautics and Space Administration Washington, D. C. 20546	14. Sponsoring Agency Code

15. Supplementary Notes

Final report.

16. Abstract

Flow fields were computed about blunted 0.524 and 0.698 radians (30 and 40 degree) cone configurations to assess the effects of nonequilibrium chemistry on the flow field geometry, boundary layer edge conditions, boundary layer profiles, and heat transfer and skin friction. Analyses were conducted at typical Space Shuttle entry conditions for both laminar and turbulent boundary layer flow. In these calculations, a wall temperature of 1365°F (2000°F) was assumed. The viscous computer program used in this investigation was a modification of the Blottner non-similar viscous code which incorporated a turbulent eddy viscosity model after Cebeci. The results were compared with equivalent calculations for similar (scaled) configurations at typical wind tunnel conditions. Wind tunnel test gases included air, nitrogen, CF_4 and helium. The viscous computer program used for wind tunnel conditions was the Cebeci turbulent non-similar computer code.

17. Key Words (Suggested by Author(s))	18. Distribution Statement
	STAR Category 12

19. Security Classif. (of this report)	20. Security Classif. (of this page)	21. No. of Pages	22. Price*
Unclassified	Unclassified	123	$5.25

*For sale by the National Technical Information Service, Springfield, Virginia 22151

Page Intentionally Left Blank

TABLE OF CONTENTS

1.0 INTRODUCTION AND SUMMARY

Critical heating on windward surfaces of the Space Shuttle are expected to occur at altitudes between 61 and 76 kilometers (200,000 and 250,000 feet). At these altitudes, the flow field is expected to be in a nonequilibrium state over much of the total vehicle length. A recent study by Lordi and Vidal (Reference 1) has indicated that these effects may have a significant effect on boundary layer growth, skin friction, and heat transfer. However, the work of Reference 1 did not address the effect of entropy swallowing by the boundary layer and thus did not provide a quantitative assessment of the phenomena. Analysis techniques are not available to define an exact windward flow field for the Space Shuttle configuration, but are available for more simple geometries (e.g. blunted cones). Flow field visualization and aerodynamic heating data have indicated that the windward flow field on the Shuttle is essentially conical at the reentry angles of attack planned for Shuttle. Therefore, total flow fields were calculated for blunted cone configurations to simulate the Shuttle flow field. The analyses consisted of defining the complete flow field around blunted cones for assumed equilibrium and reacting gas cases. Inviscid and viscous flow fields were separately computed and coupled. The axial length of the blunted cones was assumed to be 30.5 meters (100 feet). Two nose bluntnesses, corresponding to ratios of nose radius to cone length of 0.01 and 0.02, were analyzed for cones having semivertex angles of 0.524 and 0.698 radians (30 and 40 degrees). Four altitude-velocity combinations were assumed to permit definition of the flight regime for which chemical nonequilibrium effects are important. The nonequilibrium analyses were made for a noncatalytic wall at a temperature of 1365°K (2000°F). The results indicated that nonequilibrium effects in the inviscid flow field become insignificant (except in the nose region) at altitudes below 64 kilometers (210,000 feet), but that the boundary layer is affected and the resulting skin friction and heat transfer are significantly reduced below the equilibrium values. The entropy swallowing phenomena (based on the axial location at which equivalent sharp cone boundary layer edge velocity was achieved) was only slightly affected by nonequilibrium effects. Boundary layer bulk parameters (Θ and δ^*) and boundary layer profiles were strongly affected by nonequilibrium effects. However, the local Reynolds numbers based on Θ and δ^* were only slightly affected.

The degree of simulation provided by wind tunnels was also assessed. This was accomplished by conducting equivalent analyses on scaled configurations for four wind tunnels: the Mach 8 Langley Variable Density Wind Tunnel, Mach 20 Helium Tunnel, Mach 20 Nitrogen Tunnel and the Mach 6 Freon (CF_4) Tunnel. The results showed that the best simulation of the inviscid flow field (shock stand-off distance, edge Mach number) was provided by the CF_4 facility. However, the Reynolds numbers were low and turbulent heat transfer simulation would be poor. The laminar heating simulation (distribution of local to stagnation point heating) provided by all facilities was equivalent. The laminar heating distribution on the nose for the wind tunnel conditions agreed well with laminar equilibrium calculations, but on the cone surface better

agreement with the nonequilibrium values was noted. Natural boundary layer transition is unlikely except in the Variable Density Wind Tunnel. The wind tunnels provide relatively poor simulation of the boundary layer profiles and the scaled boundary layer thickness is smaller in flight than wind tunnel. This is due to the lower wall to edge temperature in flight (compared to wind tunnel) and the Reynolds number limits of the facilities.

2.0 FLOW FIELD SOLUTION TECHNIQUES

The calculations required to delineate chemical nonequilibrium effects for the shuttle spacecraft were made using previously developed computer codes to define inviscid and viscous flow fields. Solutions were coupled at the boundary layer edge by iteratively adjusting boundary layer edge conditions until the mass flow in the boundary layer was equal to the inviscid mass flow between the wall and the inviscid flow field point having the properties (P_e, V_e, T_e) corresponding to the edge conditions. A schematic of the flow field on a blunted cone is shown in Figure 1. For the example streamline shown, the mass flow in the boundary layer bounded by the streamline and the edge conditions are thus uniquely defined.

Inviscid Flow Field Solutions - The inviscid flow field analysis programs are well documented and have been proven successful in numerous applications. Detailed shock layer properties were computed in two steps consisting of subsonic nose cap region solutions and supersonic aft body solutions. The flow field properties along rays normal to the surface were obtained at selected stations along the body and were the primary output of these programs to be used in definition of boundary layer edge conditions. The equilibrium inviscid flow calculations required a separate computer program for each region, subsonic and supersonic; the nonequilibrium inviscid flow analysis combined the computer code for each region.

Equilibrium Blunt Body Solution - This modified NASA/Ames computer program (Reference 2) was used to solve the mixed subsonic/supersonic flow over the nose cap. The method is an inverse one; that is, the shock shape is specified and the gas properties and body shape determined. Convergence is obtained when a shock shape is chosen which results in the desired body shape. The inputs include the free stream conditions, shock wave, and nose bluntness. The output includes stagnation point data, shock shape coordinates, and flow field properties along the rays. Data on rays equally spaced between the stagnation point and the sonic point were obtained, including a ray in the supersonic flow field to be used as a starting line for supersonic calculations.

Supersonic Method of Characteristics Solution - The flow field properties on the aft part of the vehicle were determined by the Method of Characteristics program (MOC) developed by NASA/Ames. The principal details of this well known technique are documented in Reference 3. Numerous modifications have been made to the program but the methods are basically the same. Some of these modifications include the ability to compute vertical characteristics, mesh point constraints to allow good definition of properties in the shock layer, and equilibrium chemical species concentrations along the rays.

For stations "far" downstream of the stagnation point where the entropy layer is less than 1/10 of the shock layer, the method of characteristics solution was discontinued and a conical flow field computed. This was accomplished for reasons of economy and accuracy of flow field requirements. In the conical region the nose bluntness effects are concentrated in very thin layers near the surface which lie inside the boundary layer and therefore can be neglected for inviscid computations. Reference 4 provided estimates of the thickness of the entropy layer as functions of axial distance. The results of these calculations indicate that the entropy layers for 0.524 radian and 0.698 radian cones are independent of free stream Mach number and are 1/20 of the shock layer thickness at 6 S/R_N for the 0.698 radian cone and at 15 S/R_N for the 0.524 radian cone, which at these distances should be swallowed by the boundary layer.

Modified Curtis and Strom Unified Nonequilibrium Flow Field - A modified version of the Curtis and Strom Unified Flow Field Program (Reference 5) calculates the inviscid/viscous, nonequilibrium flow about blunt axisymmetric bodies. This program uses an iterated inverse method in the subsonic/transonic region and a method of characteristics in the supersonic region. The displacement effect of the frozen boundary layer is accounted for by matching viscous and inviscid mass fluxes at the edge of the velocity boundary layer. The blunt body solution is obtained by integrating the conservation equations along rays from the shock toward the body. The process is repeated until integration from the iterated shock shape predicts the desired body surface. Converged flow field and stream composition data in the supersonic stream are transferred to the method of characteristics solution. The Hartree method is used so that the solution may be defined along streamlines. Thus, when using the similar solution boundary layer option with the characteristic method, it is possible to drop mesh points as inviscid streamlines enter the viscous boundary layer. This results in a computational time saving device when determining the flow field over long vehicles.

Viscous Flow Field Solutions - Two viscous computer codes were used in this study. All flight calculations were made using a modified version of the viscous reacting gas computer code developed by Blottner and described in Reference 6. This program computes the nonequilibrium fluid properties and chemical species profiles for a multi-component gaseous mixture considering either binary or multi-component transport properties and finite rate chemistry. Ablation products or other added mass, varying in composition and flux along the vehicle, may be included in the solution. The partial differential equations are replaced with finite-difference equations in the program. Only one dependent variable exists in each equation and each dependent variable is solved separately using an implicit technique similar to the Crank-Nicolson method.

A description of the modified code with a check case and user's manual (Reference 7) is available to qualified requesters. The major modifications made to the computer solutions included (1) addition of eddy viscosity terms in the boundary layer equations to allow computation of turbulent boundary layers, and

(2) addition of provisions for computing an equilibrium boundary layer by bypassing the reaction rate subroutine and using equilibrium chemistry tables to define species concentrations. The eddy viscosity model is discussed in Appendix A. The equilibrium chemical composition tables were generated with a modified version of the computer program described in Reference 8. All nonequilibrium calculations were made for a noncatalytic wall. For the nonequilibrium calculations 8 reactions were assumed. These reactions and the corresponding reaction rate constants are summarized in Appendix B.

The boundary layers for the wind tunnel conditions were made with the nonsimilar turbulent viscous code developed by Cebeci for ideal gas flow. (References 9 and 10). The program is capable of computing laminar or turbulent flows for various ideal gases. The transport property data for the wind tunnel gases are summarized in Table I.

Inviscid/Viscous Flow Field Matching - The procedure utilized in this study decoupled the two phases of flow field computations, the viscous phase (boundary layer) and the inviscid phase (inviscid flow field properties) and interfaced these two independent phases through a viscous/inviscid mass flux matching in the shock layer along points at the edge of the boundary layer. Preliminary studies on the viscous/inviscid matching methods have indicated that the boundary layer thickness effects (displacement thickness corrections to the surface) are small, and at least for these cases, analyzed, the displacement thickness correction need not be considered in the inviscid flow field computation.

Initial estimates of the edge conditions for the boundary layer are made and the computations carried out. The resulting boundary layer mass flow is then used to interpolate along the previously computed inviscid field rays to determine flow conditions in the inviscid field at a point corresponding to the boundary layer mass flow value using the relation:

$$2\pi\left[\int_0^{y_\delta} r\rho\ (u + \frac{\partial v}{\partial y}\, dy)\ dy\right]_{inv} = 2\pi\left[\int_0^{\delta} r\rho\ (u + \frac{\partial v}{\partial y}\, dy)\ dy\right]_{vis}$$

where

y_δ = normal distance from surface to location in inviscid flow field corresponding to edge of the boundary layer

ρ = local density

u, v = local parallel and normal velocities

δ = edge of boundary layer (from boundary layer solution)

r = distance from axis of symmetry to location in the boundary layer

inv = inviscid solution

vis = boundary layer solution

Subsequent boundary layer iterations are made utilizing the "latest" edge conditions, and the process repeated until successive iterations yield a change in mass flow of less than a specified convergence criterion.

Initial estimates of the boundary layer edge conditions were obtained by various means. For laminar equilibrium flight cases, the initial estimates were determined from the results of a specialized computer program which calculates the variation of boundary layer edge conditions over spherically blunted cones. The boundary layer solution built into the nonequilibrium inviscid flow field program provided initial nonequilibrium laminar edge conditions and iterated laminar edge conditions were used as initial estimates for the turbulent cases. Surface conditions determined from the equilibrium inviscid flow field calculations provided initial estimates of the edge conditions for the ideal gas tunnel boundary layer computations.

3.0 DELINEATION OF NONEQUILIBRIUM EFFECTS

In order to ascertain the significance of nonequilibrium chemistry on Shuttle flow fields, analyses were conducted for representative combinations of velocity and altitude. Four analysis conditions were selected for altitudes between 61 and 76.2 km (200,000 and 250,000 ft) at free stream velocities between 4.88 and 7.32 km/sec (16 to 24 thousand ft/second). These are shown in Figure 2. Superimposed on the figure are representative Shuttle entry trajectories corresponding to reentry angles of attack of 0.506 and 0.68 radians (29 and 39 degrees). To establish the effect of altitude on nonequilibrium chemistry at critical laminar heating, two points at 7.32 km/sec (24,000 ft/sec) were used. The corresponding altitudes were 70.2 and 76.2 km (230,000 and 250,000 ft). The high altitude point is identical to that used in the study by Lordi and Vidal in Reference 1. As indicated in Figure 2, both the shock layer flow field and the boundary layer are expected to be significantly affected by nonequilibrium chemistry for these two points. The remaining points were selected to evaluate the effect of free stream velocity when the nonequilibrium effects in the inviscid flow field are of second order importance. For these latter two points, at an altitude of 64.1 km (210,000 ft), less than twenty percent of the vehicle experienced nonequilibrium edge conditions. The point at 6.1 km/sec (20,000 ft/sec) corresponds approximately to peak turbulent heating during reentry.

The geometry used to simulate the Shuttle lower surface was a blunt axisymmetric cone. Calculations were made for two cone angles and nose bluntnesses to evaluate the sensitivity of the nonequilibrium phenomena to these two parameters. A summary of the calculation matrix is included in Table II. Both laminar and turbulent viscous calculations were made for each point using the methods described in Section 2.0. A cone axial length of 30.5 meters (100 ft) was assumed.

The principal effects of nonequilibrium chemistry on the inviscid flow field is an increase in shock stand-off distance, an increase in static temperature and a reduction in Mach number at the edge of the boundary layer. The surface pressure and local velocity were only slightly affected by nonequilibrium chemistry. The major effect of nonequilibrium chemistry occurred in the boundary layer and brought about increases in the peak static temperature and modifications to the velocity profile. This results in increases in the boundary layer velocity and displacement thicknesses and decreases in the local heating rate and skin friction.

Delineation of Nonequilibrium Effects (Shock Shapes) - Inviscid equilibrium and nonequilibrium characteristics were computed for blunted cones of 0.524 radian (30 degrees) and 0.698 radian (40 degrees) half angles. The computations were conducted for the flight conditions as summarized in Table II to

define nonequilibrium chemistry effects on the shock shape and related flow field characteristics. Figure 3 presents a sample comparison of shock shape characteristics for the 0.524 radian half angle cone with a 0.6096 meter nose radius. The sample shock shapes shown reflect the 76.2 km maximum altitude computation at a velocity of 7.32 km/sec where nonequilibrium effects would be most prominent. The shock shapes are very similar with the primary chemistry sensitivity displayed in the thicker shock layer of the nonequilibrium case. This typical effect can be attributed to the "stiffness" of the relaxing gas which produces a smaller degree of compressibility compared to the equilibrium case. The standoff distance at the stagnation point is shown to be increased by approximately 80 percent due to nonequilibrium chemistry at these flight conditions. Shock shapes for the entire set of equilibrium inviscid flow fields are tabulated in Appendix C.

Figure 4 presents a summarization of shock standoff distance ratio, nondimensionalized by equilibrium chemistry results, for the flight condition computations. The standoff distance ratio is presented as a function of stagnation point density ratio and the figure shows the standoff distance ratio to increase with decreasing density ratio. The highest standoff distance values indicated reflect the 76.2 altitude computations with nose radii of 0.3048 and 0.6096 meters.

Pressure Distribution - Nonequilibrium chemistry has little effect on the boundary layer edge pressure. As can be seen in Figures 5 and 6, pressure is only slightly affected at the high altitude and only in the nose region. The nonequilibrium pressure is lower than the corresponding equilibrium pressure. On the afterbody at the high altitude and over the entire body at low altitude the nonequilibrium pressure equals the equilibrium value. Aft of the shock overexpansion, as indicated by the minimum point in the pressure curves, nose bluntness effects disappear and the pressures approach sharp cone values. Nonequilibrium effects are experienced on the first ten to fifteen percent of the vehicle length. The nonequilibrium effects on the laminar boundary layer edge pressure as shown in the above figures are identical for the turbulent boundary layer pressure distribution.

Velocity Distribution - Like the pressure, the boundary layer edge velocity distribution, shown in Figures 7 and 8, is relatively unaffected by nonequilibrium flow. There are some differences, however, between laminar and turbulent flow in the high entropy nose region forward of swallowing. In general, the nonequilibrium velocity for the sharper nose laminar case tends to be lower than the equilibrium velocity, and the nonequilibrium velocity for the blunter nose laminar case tends to be higher than the equilibrium velocity. It appears that the trend is reversed for turbulent flow. Here, the sharper nose nonequilibrium velocity is greater than the equilibrium value and the blunter nose nonequilibrium velocity is less than the equilibrium value. In the sharp cone region of the flow field, nonequilibrium velocities are lower than, and tend to approach, the equilibrium sharp cone values.

Entropy Layer - As shown in Figures 7 and 8, the boundary layer edge velocity reaches the sharp cone velocity within the first ten percent of the vehicle for laminar and within the first eight percent for turbulent flow. If the inviscid entropy layer is defined as the inviscid region containing the gases processed by the high entropy portion of the curved nose shock, this layer extends to the location at which the boundary layer edge velocity first becomes equal to the sharp cone value. Because of the inflection in the shock system the local velocity actually exceeds the sharp cone value for some distance before constant cone velocity is reached. The locations at which sharp cone velocity is first reached for flight are summarized in Table III. As expected, the percentage of the vehicle experiencing high entropy flow is increased as nose diameter is increased and/or altitude and cone angle are lowered. The effect of nonequilibrium on this phenomena is generally small for the laminar cases except for the high altitude cases for which sharp cone velocity is reached very near the nose-cone juncture. For turbulent boundary layer conditions the axial extent of the entropy layer for nonequilibrium was greater than or equal to the equilibrium values.

Temperature Distribution - Boundary layer temperature is most affected by nonequilibrium chemistry. Both altitude and nose bluntness effects for laminar and turbulent flow are compared in Figures 9 through 12. There is little difference between the laminar and turbulent temperatures at either the high or low altitudes. Nonequilibrium effects at the high altitude persist for the entire vehicle length, as can be seen in Figure 9. The sharper nose produces nonequilibrium temperatures in the stagnation region which are almost three times as great as the equilibrium values; and the blunter nose, approximately twice the equilibrium values at the stagnation point. Nose bluntness effects are relatively nil on the afterbody, with nonequilibrium temperatures approximately 50 percent greater than the equilibrium value.

At the lowest altitude condition the nonequilibrium effects are small, with considerably less nose bluntness effects at the stagnation point. Nonequilibrium stagnation temperatures are about 30 percent greater than the equilibrium values, but the nonequilibrium effects are dissipated in the vicinity of the hemisphere-cone tangency point, or shoulder.

Mach Number - The range of local Mach number for the two cone angles over the entire flight regime is presented in Figures 13 and 14. Equilibrium flow is represented by the entire band width, while nonequilibrium occupies a much narrower portion in the lower part of the same band. Mach numbers on the afterbody of the larger cone lie between 3 and 4; values on the afterbody of the smaller cone lie between 4 and 5.5. The hump in the band corresponds to the velocity overshoot on the afterbody.

Local Reynolds Number - The range of local Reynolds number over the entire flight regime for the two cone angles is presented in Figures 15 and 16. Here, nonequilibrium flow is represented by the entire band width, with only a narrow strip not representing also equilibrium flow.

Momentum Thickness Distribution - Momentum thickness is important in transition analyses and is presented in Figures 17 and 18. At the high altitude condition, nonequilibrium increases the momentum thickness. At the low altitude condition however, there are no nonequilibrium effects.

Displacement Thickness Distribution - The displacement thickness distributions for the altitude extremes are presented in Figures 19 and 20. In general, nonequilibrium effects tend to increase the displacement thickness at all altitudes, with the exception of the near nose region at the high altitude condition. It appears also, that there is an additional nose bluntness effect at the vehicle base for the high altitude case.

Momentum Thickness Reynolds Number - The local momentum thickness Reynolds number distribution is presented in Figures 21 and 22. Like the momentum thickness itself, this parameter is also important in transition analyses. These data reflect the trends of both the local Reynolds number and the momentum thickness. Nonequilibrium effects are present at the high altitude condition and result in lower values. At the low altitude condition, as with the momentum thickness, there are no nonequilibrium effects on the momentum thickness Reynolds number.

Laminar Sublayer - Comparisons of the turbulent boundary layer laminar sublayer thickness with the laminar boundary layer thickness are made in Figures 23 and 24. The sublayer thickness is defined as the point in the boundary layer where the velocity is equal to 10 percent of the edge value. As can be seen from these figures, the sublayer growth follows the same trends as does the complete boundary layer. In the near nose region at these altitude conditions the boundary layer is practically all sublayer, indicating that transition probably really starts aft of this location, although this study was carried out assuming turbulent flow over the entire vehicle. Table IV compares the nonequilibrium and equilibrium sublayer thicknesses at the base for all flight conditions considered. Nonequilibrium effects increase with increasing altitude and tend to increase the sublayer thickness. There is no apparent effect of nose radius for these cases.

Heat Transfer - The heating rate distribution for laminar and turbulent flow at two altitudes is presented in Figures 25 through 28. It may be seen from the figures that laminar and turbulent heating are equal in the stagnation region where the major portion of the turbulent boundary layer is laminar sublayer. Turbulent effects are present mainly on the afterbody. Nonequilibrium effects at the stagnation point may be seen from Table V, which presents the ratio of nonequilibrium to equilibrium heating for both nose bluntnesses. It is apparent that there is a significant reduction in stagnation point heating due to nonequilibrium effects, the smaller nose being closer to equilibrium heating than the larger nose. In general, the nonequilibrium heating tends to approach equilibrium with decreasing altitude and velocity although the nonequilibrium effects are greatest at the intermediate altitude.

There remains a significant reduction of heating due to nonequilibrium flow on the afterbody at all altitudes, although there is little nonequilibrium effect on the edge properties at the lower altitudes. The nonequilibrium to equilibrium heating ratio at the base is presented in Table VI. It can be seen that the nonequilibrium heating reduction at the base is greater in the turbulent case than for the laminar case. This can also be seen from Figure 29 which presents the distribution of the nonequilibrium to equilibrium heating ratio. Table VI further shows a nose bluntness effect on the laminar nonequilibrium heating at the base, but none on the turbulent heating. The laminar nonequilibrium heating at the base is affected by nose bluntness and altitude in a fashion similar to the stagnation point heating discussed above.

Nonequilibrium effects on heating in the near-nose region are shown in Figure 29. Because the boundary layer is included in the matching between the viscous and inviscid flow fields, the nonequilibrium edge lies between the surface streamline and the shock, in a highly nonequilibrium flow region. As was pointed out previously, the stagnation point heating experiences a significant reduction caused by nonequilibrium effects. Moving away from the stagnation point, nonequilibrium effects are reduced, thereby approaching equilibrium values. In the vicinity of the shoulder the inviscid flow becomes frozen in the overexpansion region and nonequilibrium effects are more important again. This curve can be compared to a similar figure prepared by Lordi in Reference 1, which assumes the surface streamline is the edge. The referenced curve shows no nonequilibrium effects at the stagnation point, for the reason explained above, but does indicate nonequilibrium effects at the shoulder. The first peak in the curve of Figure 29 probably corresponds to some point on the referenced curve and the curves are similar to the shoulder, although Figure 29 shows an undershoot. The figure also indicates little difference in the nonequilibrium heating reduction along the afterbody.

Figure 30 indicates the extent of flow field condition on the nonequilibrium effects at the lowest altitude. Nonequilibrium heating distributions for both laminar and turbulent boundary layers are compared using both

an equilibrium and a nonequilibrium inviscid flow field edge. The nonequilibrium heating in the stagnation region is greater for the nonequilibrium edge than for the equilibrium edge. Moving aft however, the heating for the two converge until all differences disappear at 20 feet. It may be concluded from this that nonequilibrium effects are greater in the boundary layer itself rather than resulting from nonequilibrium effects in the inviscid flow field.

Boundary Layer Transition Parameters - The more significant effects of chemical nonequilibrium are manifested in the boundary layer and result in higher peak temperature, lower peak density, smaller δ^* and larger Θ than for equilibrium for the laminar flow cases. It is therefore expected that boundary layer transition from laminar to turbulent flow (or at least the values of transition parameters) may differ for the two cases. Much research has been conducted to better understand and correlate boundary layer transition data from both flight and ground test. However, fundamental understanding of this phenomena is still lacking for flight and (at best) limited success in correlating compressible wind tunnel data has been obtained. The fluid dynamic parameters which have been found to have a major influence on the boundary layer transition process include the Reynolds number, Mach number, and boundary layer profile parameters such as δ^* and Θ. Correlations for Shuttle configurations have been made for groupings of the above parameters by a number of investigators (References 11, 12, and 13).

The correlating forms included $Re_\Theta/M_L]_T$ = const; $Re_\Theta/M_L(Re/\ell)^{-2}]_T = f(\alpha)$; $Re_L]_T = f(M_L)$; $Re_L]_T = f(M_L, T_w/T_{T_\infty})$ and $Re_{\delta^*}]_T = f(Re/\ell, Me)$. The correlations were generally limited to ground test data since the flight data on lifting entry vehicles are limited. Extrapolation of the various correlating forms to flight has been shown (Reference 11) to produce widely different transition altitudes. This suggested that a number of correlating forms be investigated in the delineation of nonequilibrium effects. This was done by comparing the axial location of boundary layer transition onset predicted by the various correlating forms for the equilibrium and nonequilibrium calculations at each flight point. A summary of the predicted location of transition for three correlating froms: Re_Θ/M_L = const; $Re_\Theta/M_L(Re/\ell)\cdot 2=f(\alpha)$; and $Re_L]_T = f(M_L, T_w/T_{T_\infty})$ are included in Table VII.

Scottoline in Reference 12 indicated that the Shuttle wind tunnel transition data could be correlated in terms of $Re_\Theta/M_L]_T = 272$. For this value of transition parameter, boundary layer transition would not occur for the flight conditions included in this study. More recent experiments have indicated that lower surface centerline transition may occur on the Shuttle at values of $Re_\Theta/M_L]_T$ between 150 and 200, and predicted locations of transition are included in the table for both values. As shown in the table, transition is predicted for the two low altitude trajectory points only.

The two other correlating forms used to fit the wind tunnel data (which have been reported in Reference 11 used to predict the location of transition are:

$$0.79 \times Re_\Theta/M_L (Re/\ell)^{.2}\Big]_T = \text{PAR 1} = 10 \text{ and } \frac{Re_L}{M_L^{1.05}(T_w/T_{T_\infty})^{1.04}}\Big]_T = \text{PAR 2} = 2.3 \times 10^6$$

A major portion of the cone would experience transitional or turbulent boundary layer flow based on these parameters for altitudes below 70.2 km (230,000 feet).

Effect of Nose Radius - The transition locations predected by all the parameters are aft of the entropy swallowing points on the cone except for the blunt nose low altitude conditions. The use of PAR 1 as a transition criterion would predict transition very near the nose for these low altitude cases, and results from a near-nose peak in the value of this parameter which is caused by the combined effects of locally high momentum thickness and low local Mach number and unit Reynolds number. This variation for two low altitude cases is shown in Figure 31. Similar characteristics were found for $Re_\Theta/M_L]_T$, but the values were less than the critical value. This is shown in Figure 32. Thus, the predicted location of transitiin is essentially independent of nose radius for the majority of conditions considered.

Effect of Cone Angle - Based on the results shown in Table VII, increasing the cone angle (or equivalent angle of attack of a Shuttle configuration) from 0.524 to 0.698 radians (30 to 40 degrees) would move the transition location forward at the same altitude and velocity. This is primarily due to the reduced local Mach number for the larger cone angle. It should be noted that the local Reynolds number is also lower for the larger cone angle but, since all criteria assume Mach number dependence, the net effect is a forward movement of transition onset.

Effect of Chemical Nonequilibrium - The predicted effect of chemical nonequilibrium is found to be a function of the criterion used. Using Re_Θ/M_L or PAR 2 as criteria, the predicted location of transition onset for the nonequilibrium case is equal or aft of the corresponding equilibrium value. Using PAR 1, on the other hand, the nonequilibrium transition location is generally predicted forward of the equilibrium case. This is due to lower local unit Reynolds numbers for the nonequilibrium cases than for the equilibrium at the same physical location. The effect of nonequilibrium chemistry on the various transition parameters can be seen by comparing the results of Table VIII. The table contains the ratio of equilibrium to nonequilibrium values of the various transition parameters for $X/L = 1.0$. PAR 1 and Re_Θ/M_L are only slightly affected by nonequilibrium chemistry whereas Re_L and PAR 2 are greatly affected at altitudes above 70.2 km (230,000 feet).

Viscous/Inviscid Flow Field Profiles - The analyses of equilibrium flow fields also included the definition of properties within the shock layer itself. Comparisons were made of the flow properties in the hemisphere/cone junction region ($S/R_N = 0.5$) and at a point mid-way aft on the cone ($S/R_N = 20$). Comparisons of equilibrium and nonequilibrium conditions in these regions included the definition of local temperature, velocity, and electron concentration profiles in the shock layer. The results are summarized in Figures 33, 34 and 35. The nonequilibrium effects on termperature shown in Figure 33 are relatively small in the nose region ($S/R_N = 0.5$) with a large increase in sensitivity at the downstream location. The velocity comparisons of Figure 34 show much less sensitivity to nonequilibrium chemistry with the largest influence observed near the body in the nose region. The electron concentration comparisons of Figure 35 exhibit a similar behavior since the electron densities are directly affected by temperature. The electron conectrations converge towards zero at the shock for the nonequilibrium flow since it is assumed that the flow is frozen in the shock itself. Pressure distributions, although not shown, were relatively insensitive to nonequilibrium influence.

Boundary Layer Profiles - The finite difference viscous solution used to delineate nonequilibrium effects provided not only the local heat transfer, skin friction and boundary layer integral parameters, but also well defined the boundary layer profiles of velocity, temperature, density and species. Examples of the results are included in Figures 36 and 37. The case selected for this example is one for which the inviscid flow field is very near equilibrium at the edge of the boundary layer and any differences in the profile are due to boundary layer chemistry. The laminar velocity profiles in Figure 36 show that the axial velocity at a given height above the cone surface is greater for the equilibrium than the nonequilibrium case and that the boundary layer is slightly thinner. In contrast to this, the turbulent boundary layer velocity profile, shown in Figure 37, is essentially unaffected by nonequilibrium effects. This figure also illustrates the change in profile from the near laminar shape at $S/L = 0.01$ to the fuller turbulent profile at $S/L = 0.67$.

The effect of nonequilibrium chemistry on the static temperature distribution is shown in Figure 38 for laminar flow. For the equilibrium case, the peak temperature in the boundary layer is approximately five percent greater than the edge temperature (except in the stagnation region) and the values correspond closely to similar boundary layer solution results. In the nonequilibrium case, on the other hand, the peak temperature is approximately thirty percent higher than the boundary layer edge value. The turbulent results are summarized in Figure 39. The peak temperatures occur very near the wall and reach values higher than for the laminar case (except at $S/L = 0.01$ and 0.09 which are close to the laminar values).

These results confirm the importance of nonequilibrium chemistry in the boundary layer at altitudes of 64 km (210,000 ft) and below, even though the inviscid flow field is near equilibrium.

The differences are even more pronounced at the high altitude condition since the inviscid flow field is also in a nonequilibrium state. For example the peak nonequilibrium temperature in the boundary layer is 60 percent greater than the equilibrium value at 76.2 km (see Figures 33 and 34 for the inviscid flow field profiles) for a turbulent boundary layer and 65 percent higher for the laminar case.

From a communications blackout and observables standpoint, the electrons present in the flow field are important. Since the NO^+ reaction was included in this study, data are available to assess the effect of nonequilibrium chemistry on the electrons in the flow field. An example of these effects (Figure 40) shows the free electrons present in the boundary layer as a function of axial location at 64 km. As shown by the dashed lines, the free electrons would be reduced sharply as the boundary layer edge temperature drops from the stagnation value to sharp cone values (at S/L = 0.1) and then increase (as the boundary layer thickness increases) toward the rear of the cone. This would suggest, for example, that an appropriate place to install antennas is near the front of the cone and that the number of free electrons would be nearly two orders of magnitude less than at the rear (or at the stagnation point) of the cone. But, a completely different conclusion is reached if one considers the results of the nonequilibrium calculations. The finite reaction rates produce a nearly constant quantity of free electrons - only a slight reduction from stagnation point value occurs with movement aft on the cone. The primary reason for this change in characteristics is the thicker boundary layer for the nonequilibrium case and reduced recombination near the wall because of the finite reaction rates.

4.0 ASSESSMENT OF WIND TUNNEL SIMULATION

A variety of wind tunnels are available and have been used in aerothermodynamic tests of Shuttle configurations. The degree of simulation provided by a number of these facilities has been assessed by comparing predicted flow field properties, surface heat transfer and skin friction with flight values. Total flow fields were computed for scaled cone configurations idential to those for which flight calculations were made for seven tunnel free stream conditions.

The tunnel free stream conditions were based on the operating range available in four Langley Research Center wind tunnels: The Mach 8 Variable Density Air Tunnel, the Mach 20 Nitrogen Tunnel, the Mach 20 Helium Tunnel, and the Mach 6 Freon (CF_4) Tunnel. A summary of the twenty-eight cases for which calculations were made is included in Table IX. It should be pointed out here that the CF_4 tunnel facility is capable of operating at pressures as high as 3000 psi, although a lower value was used in the present analysis. All tunnel calculations were made assuming the test gas behaved as an ideal gas (γ = const) and the model temperature was assumed to be 338°K (150°F).

Blunt body and method of characteristic solutions for the inviscid flow field were coupled with laminar and turbulent viscous solutions in the manner described in Section 2. Comparison of the wind tunnel calculations with the corresponding flight values indicates that the best simulation of the shock shape and boundary layer edge Mach number is provided by the Freon (CF_4) tunnel. The laminar heating distributions (referenced to the stagnation point value) are similar for all facilities and match the equilibrium flight values near the nose, but agree more closely with nonequilibrium flight values on the aft portion of the cone. Natural transition from laminar to turbulent flow is unlikely for the selected model sizes except for the high pressure air test conditions (Cases T-5 through T-8). The ratio of turbulent to laminar Stanton number and skin friction coefficient correlate well with local Reynolds number for all wind tunnel calculations. However, at the same local Reynolds number, the Stanton number ratio is less for flight than for the wind tunnel, and the skin friction coefficient ratio is greater for flight than for wind tunnel conditions.

The best simulation of the boundary layer profile parameters is provided by the air wind tunnel, but the ratio of wall to edge temperature is higher than flight for all tunnel conditions.

Comparisons of Wind Tunnel with Flight Shock Standoff Distance - The geometric characteristic of the flow field which differs most between wind tunnel and flight is the shock stand-off distance. For a M=8 air wind tunnel the scaled standoff distance is between 2 and 3 times the equilibrium flight

value. The results of the inviscid flow field calculations for flight and wind tunnel are compared in Figure 41. A reasonable correlation of the stand-off distance was achieved in terms of the stagnation density behind the normal shock at the stagnation point. This curve shows that the Freon tunnel provide best simulation of this parameter. In all other tunnels, the shock is located well outboard of the expected flight location and use of these tunnels to establish the location of nose/wing shock intersection of more complex configurations is likely to be misleading since the wind tunnel shock intersection would be located outboard of the shock present in the flight situation.

Local Mach Number - Direct comparisons of wind tunnel and flight boundary layer edge conditions for similar configurations indicates that the local Mach number distribution in flight is best matched in the CF_4 tunnel. In fact, aft of the location where the gases in the high entropy shock layer are swallowed, the agreement with the nonequilibrium calculations is excellent for the 0.698 radian (40°) cone. The local Mach number for all other test gases is lower than the predicted flight values. This is shown for the blunter configurations ($R_N/L = 0.02$) in Figures 42 and 43.

Edge Entropy - It can be seen by comparing the Mach number distributions in Figures 42 and 43 that a larger fraction of the cone is affected by the high entropy shock layer for wind tunnel conditions than is expected in flight. This is shown even more clearly in Figures 44 and 45. which compare the axial extent of high entropy inviscid flow for wind tunnel with the flight values, as a function of bluntness Reynolds number based on free stream properties. The curves show that the sharp cone velocity would be reached aft of the predicted flight location in wind tunnel tests if the free stream Reynolds number is simulated. An interesting characteristic of the figures is the apparent insensitivity to wind tunnel test gas and a Mach number sensitivity. This suggests that better correlation could be achieved if a Mach number dependent Reynolds number were used, e.g., Reynolds number behind the normal shock. Figure 46 shows the results for the 0.524 radian (30°) cones. Good correlation of the air, nitrogen, and helium results is achieved, but the Freon data fall below the other results. This parameter seems to overcorrect the flight results, which lie above the wind tunnel values for this form of correlation.

Boundary Layer Profile Parameters - A comparison of the scaled displacement thickness to the flight values is shown for one configuration in Figures 47 and 48. Reasonably good simulation of the turbulent displacement thickness is provided by the air wind tunnel on the cone surface, but for all other facilities the displacement thickness is greater than the flight values. This is due to the lower Reynolds numbers for these test conditions and effect of higher wall to boundary layer edge temperature than for flight. It can be noted that the nonequilibrium flight values (1) follow a different trend with Reynolds number than the wind tunnel and equilibrium flight values and (2) are greater than the equilibrium flight values.

Different characteristics were found for the momentum thickness. Figures 49 and 50 show that a good correlation exists between the momentum thickness and local Reynolds number. Only the turbulent helium wind tunnel results and the laminar air wind tunnel results fall off the correlation lines. This good correlation suggests that simulation of local Reynolds number is the only necessary condition to match the flight momentum thickness. Table X compares the sublayer thicknesses at the base for all tunnel conditions considered. As with the flight conditions, there is no apparent effect of nose radius. The scaled thicknesses are, in general, greater than those predicted for flight. It appears that the variable density air tunnel best simulates the nonequilibrium sublayer thickness.

Heating Rate Simulation - The laminar heating rate simulation provided by the wind tunnels is shown in Figure 51. Superimposed in the figure are laminar equilibrium and nonequilibrium distributions of local to equilibrium stagnation point heating for flight and wind tunnel calculations for the 0.698 radian (40°) cone configuration. The distribution on the nose cap for wind tunnel conditions is in good agreement with the equilibrium flight values. Little effect of test gas or Mach number is present. Aft of the hemisphere-cone juncture the various wind tunnel points show a sensitivity to test gas and Reynolds number. This is due to the difference in entropy swallowing for the various conditions. At the rear of the cone, close correspondence in the wind tunnel heating is again noted; but the wind tunnel values are all lower than the equilibrium flight values and approach the lower nonequilibrium flight results. The close agreement between the various wind tunnel distributions was surprising since the viscosity relations and surface pressures differ considerably.

A summary of the ratio of local to stagnation point heating all wind tunnel cases at four selected locations is summarized in Table XI for the 0.524 radian (30°) cone and Table XII for the 0.698 radian (40°) cone. Evaluation of these results suggests that better simulation of equilibrium flight heating on a 0.524 radian (30°) cone is achievable by testing at a higher cone angle. As a test of this hypothesis the wind tunnel results for the 0.698 radian (40°) cone were compared with the equilibrium flight predictions for the 0.524 radian (30°) cone. On the aft 60 percent of the cone excellent agreement occurred, but very poor simulation was provided in the entropy layer.

The turbulent heating rate distributions for the tunnel conditions produced a number of interesting results. The laminar and turbulent heating rates were nearly identical for the low Reynolds number nitrogen conditions; whereas the turbulent heating was nearly six times the laminar values for the air calculations. This can be seen by comparing the results of Figures 52 and 53. This phenomena results from the sensitivity of the boundary layer eddy viscosity to Reynolds number. At the low Reynolds numbers for the nitrogen test conditions the eddy viscosity is small compared to the dynamic viscosity, thus the "turbulent" flow is really "laminar". As shown in Figure 54, the ratio of turbulent to laminar heating at the aft end of the cones correlated

with local Reynolds number and is independent of test gas, nose diameter and cone angle. For comparison, corresponding flight values are included in the figure. The flight values (at the same Reynolds number) are lower than the tunnel results, are a function of the cone angle, and are lower for the non-equilibrium cases than for equilibrium. Similar results are shown for skin friction in Figure 55. Again, good correlation of the tunnel results is achieved. However, the ratio of skin friction coefficients in flight is actually higher than predicted for wind tunnel conditions.

Boundary Layer Transition Parameters - The axial distribution of parameters used to predict the location of boundary layer transition onset were computed for all the laminar wind tunnel cases. Assuming that the critical value of the parameters is the same as used in the flight evaluation, it was found that the transition parameters do not exceed critical values for the majority of tunnel conditions. This is shown in Table XIII. For the model sizes selected in this analysis, the local Reynolds numbers at the aft end of the vehicle are less than 1.5 million for all wind tunnel cases except the high pressure air cases. In much the same manner as flight, the various parameters predict transition at different locations for the same configuration and test condition. However, the differences are smaller. For the high pressure air case, increasing bluntness appears to move the transition location aft and earlier transition is predicted for the 0.698 radian (40°) cone than the 0.524 radian (30°) cone. An investigation was made to evaluate in more detail the effect of nose bluntness on critical transition parameters. In this comparison the results of an independent research and development analysis for a blunter $R_N/L = 0.06$ cone were compared with the results of the air cases for the 0.698 radian cone. The local Reynolds number at the aft end of the cone was essentially independent of nose radius since all cones had the same axial length. However, the high entropy shock layer extended over a greater portion of the cone as nose bluntness increased. This results in lower length Reynolds numbers and Mach numbers on the forward half of the cone. For the very blunt nose configuration it was found that the displacement thickness on the nose cap was much lower than the sharper configurations for the same surface distance. This would make a blunt nose configuration more sensitive to roughness induced boundary layer transition. Table XIV summarizes the displacement thickness at the sonic point for these cases. At this location the blunter nose has a greater displacement thickness since the surface distance to the sonic point scales directly with nose diameter. The variation of momentum thickness at the sonic point with nose radius is shown for the two test Reynolds numbers in Figure 56. The values are below typical blunt body criteria (Re_θ = 150 to 200) and natural transition on the nose would not be expected for these test conditions.

An estimate of the ability of the tunnels to simulate the flight values of the transition parameters can be made by comparing the results shown in Table XV. In this table the range in the values of the parameter is summarized for the aft end of the cones. These results show that the local Reynolds number and Re_θ/M_L for high altitudes can be simulated in the helium and Freon tunnels, but PAR 1 and PAR 2 are not simulated. The air tunnel

is the only facility which fits the flight range of transition parameters at the aft end of the cone for all parameters.

Boundary Layer Profiles - As was shown in Figures 49 and 50, reasonably good scaling of the momentum thickness could be achieved in the wind tunnels, but the boundary layer velocity and displacement thicknesses did not correlate directly with the flight values. The reason for the difference can be seen by comparing the boundary layer profiles for the wind tunnel conditions with equivalent flight profiles. This has been done for a location midway on the cones. In Figures 57 through 60, the ratio of boundary layer static temperature to edge static temperature is plotted as a function of scaled height above the cone surface for laminar boundary layers in air, nitrogen, helium and Freon, respectively. Included on each curve are corresponding values for flight conditions encompassing the range studied. Both equilibrium and nonequilibrium results are included. The figures show that the best simulations of the profiles are provided by the air cases. All other wind tunnel conditions produce boundary layers much thicker than the air case. The ratio of peak to edge temperature, on the other hand, was simulated better by the nitrogen and Freon facilities than the air facility, except for the low altitude nonequilibrium flight condition.

Figures 61 through 64 show equivalent results from the turbulent boundary layer calculations. In general, boundary layer profile simulation was not good even though the profile parameter θ/L and δ^*/L correlated reasonably well with local Reynolds number. This is of course due to the fact that poor Reynolds number simulation is provided by all facilities (except the Mach 8 air tunnel) for the model scale limits provided.

5.0 CONCLUSIONS AND RECOMMENDATIONS

The conclusions arrived at in this study are logically divided into two categories: (1) delineation of nonequilibrium effects for flight conditions and (2) flight aerothermodynamic simulation provided by wind tunnel test facilities.

Nonequilibrium Effects for Flight Conditions -

1. The nonequilibrium inviscid shock is geometrically similar to the equilibrium flow field, but the stand-off distance at the shock is greater for the nonequilibrium than for the equilibrium case. The stand-off distance was found to correlate with density ratio across the normal shock and was less then twice the equilibrium stand-off distance for the flight velocity-altitude range considered.

2. At the lowest altitude condition, 64.1 km (210,000 feet), the inviscid flow field was essentially in chemical equilibrium over the majority of the cone.

3. The entropy layer extended over less than 15 percent of the cone surface, and there was no significant effect of chemical nonequilibrium on the location where sharp cone velocity was reached. Entropy layer effects, as expected, were less significant for the turbulent than for the laminar flight cases.

4. The boundary layer edge Mach number and Reynolds number were lower for nonequilibrium than equilibrium. This was due to the higher edge temperature for the nonequilibrium case.

5. The static pressure at the boundary layer edge was essentially unaffected by nonequilibrium chemistry.

6. The aerodynamic heating and skin friction were found to be affected by nonequilibrium chemistry for all flight conditions (for the assumed noncatalytic wall boundary condition). Finite wall catalycity would increase the nonequilibrium heating so that nonequilibrium values would be closer to the equilibrium predictions.

7. Because of the low Reynolds numbers on the nose, the eddy viscosity was low and laminar and turbulent heating on the nose were the same for the 76.2 km (250,000 feet) and 70.2 km (230,000 feet) altitude conditions.

8. The heating reduction caused by nonequilibrium chemistry was greater for the turbulent boundary layer calculations than for the laminar case. At the cone base the reduction was between 10 and 30 percent for laminar flow while the reduction was between 35 and 40 percent for the turbulent calculations.

9. The effect of nonequilibrium on representative boundary layer transition parameters was found to be a function of the parameter. Parameters utilizing Re_θ/M_L were found to be relatively insensitive, whereas those containing Re_s were found to indicate delayed transition when nonequilibrium effects are considered.

10. Predicted transition locations were found to be essentially independent of nose diameter for flight; but increasing cone angle (from 0.524 to 0.698 radians) produced a forward movement of the transition location.

11. Boundary layer profiles for laminar flow indicated a thicker boundary layer and higher peak temperature in the nonequilibrium case. Considerably lower velocities existed at a fixed height in the boundary layer for the nonequilibrium case. Only slight differences in velocity were noted in the turbulent cases, but the peak temperature was much higher for nonequilibrium flow.

12. More electrons were produced near the forward end of the cone, but fewer at the base for nonequilibrium flow.

Aerothermodynamic Simulation Capabilities - Conclusions derived by comparing the flight calculations with equivalent calculations for four wind tunnels; the Mach 8 Variable Density Air Wind Tunnel, Mach 20 Nitrogen Tunnel, Mach 20 Helium Tunnel, and the Mach 6 Freon (CF_4) Tunnel are:

1. Shock stand-off distance when scaled to nose radius is greater than flight for all tunnels but the Freon tunnel.

2. The extent of entropy layer effects is greater for the wind tunnel than flight at scaled free stream Reynolds number. Lower Reynolds number testing is required to match the entropy layers.

3. There is minimal effect of test gas on the laminar axial heating rate (q/q_s) distribution except in the entropy layer. The wind tunnel distributions agree with the equilibrium flight distributions on the nose and with the nonequilibrium values on the afterbody. In all cases, the ratio of local to stagnation point heating at the cone base is less than predicted flight values.

4. The ratio of turbulent to laminar heating scales with local Reynolds number for the wind tunnel calculations. At the same Reynolds number the ratio obtained from the flight calculations is lower than wind tunnel values. To match this ratio it would be necessary to test at a lower Reynolds number. By so doing, both this ratio and the entropy layer would better match the flight values. However, a poorer match of skin friction would result since the predicted flight values of the ratio of turbulent to laminar skin friction is higher than the correlated tunnel values.

5. Natural transition from laminar to turbulent flow is (1) unlikely in the nitrogen and Freon tunnels, (2) marginally possible is the helium tunnel, and (3) likely for the high Reynolds number air tunnel conditions. If the relatively small model sizes (0.153 m (0.5 feet) for the nitrogen tunnel and 0.2155 m (0.7 feet) for the other wind tunnels) were increased, natural transition is possible in the helium and Freon tunnels.

6. As with the flight calculations, nose diameter is predicted to have a slight effect on cone transition, but a larger nose may be more prone to roughness induced transition. However, in contrast to flight predictions, transition on the 0.524 radian (30^{o}) cone is predicted to be farther forward than for the 0.698 radian (40^{o}) cone.

7. Scaled boundary layer velocity, displacement and momentum thickness are greater in ground test than flight (except for the Mach 8 air tunnel). Both tunnel and flight scaled momentum thickness at the vehicle base correlate well with local Reynolds number.

Based on this study, it is recommended that additional research be conducted to meet three major objectives: (1) verification of the analytic results, (2) incorporation of the effect of finite catalycity on the study results, and (3) evaluate various boundary layer transition criteria.

Verification of the analytic results (for nonequilibrium chemistry) is, at best, difficult. However, plasma tunnels can provide a gross verification for laminar flow. For turbulent flow, wind tunnel tests can assist in verifying the eddy viscosity model. Investigations of two types would be required: (a) basic investigations of boundary layer profiles combined with skin friction and heat transfer measurements on relatively simple cylindrical shapes, and (b) aerodynamic heating tests of blunt cone configurations of the type analyzed to verify the results predicted with various eddy viscosity models. Larger scale models or artifical trips would be required to obtain transition in the helium and Freon facilities. These latter group of tests could also provide an empirical assessment of various transition criteria. As noted in this study, the relationships between edge Reynolds

number, displacement thickness, momentum thickness, edge Mach number, and wall to edge temperature are uniquely different for the various facilities. Thus, a broader base of data would be provided to verify various correlating approaches. These data should be supplemented by acoustic measurements in the tunnel to verify that the results are not uniquely due to tunnel free stream disturbances.

The results of this study indicate a large effect of nonequilibrium chemistry on turbulent heating for the noncatalytic wall assumption. Few surfaces are truly noncatalytic. Investigations have shown that catalytic efficiencies of silica/silicon carbide materials may be between 10^{-3} and 10^{-2}. The corresponding reduction in heating from equilibrium values for laminar boundary layers has been shown to be less than half the amount predicted for a noncatalytic wall, but no analyses are available to predict the effect for the turbulent case. This can be accomplished by additional calculations with the turbulent viscous code with a changed wall boundary condition.

6.0 REFERENCES

1. Lordi, J. A., Vidal, R. J., and Johnson, C. B., "Chemical Nonequilibrium Effects on the Inviscid Flow in the Windward Plane of Symmetry of Two Simplified Shuttle Configurations," NASA TN D-7189, March 1973.

2. Lomax, H., and Inouye, M., "Numerical Analysis of Flow Properties About Blunt Bodies Moving at Supersonic Speeds in an Equilibrium Gas," NASA TR-R-204, July 1964.

3. Inouye, M., Rakich, J. W., and Lomax, H., "A Description of Numerical Methods and Computer Programs for Two-Dimensional and Axisymmetric Supersonic Flow Over Blunt-Nosed and Flared Bodies," NASA TN D-2970, August 1965.

4. Moretti, G. and Pandolfi, A., "Entropy Layers," Pibal Rpt. No. 71-33, Nov. 1971.

5. Curtis, J. T., and Strom, C. R., "Computations of the Nonequilibrium Flow of a Viscous, Radiating Fluid About a Blunt Axisymmetric Body, Volume I: Equations and Results," AFFDL-TR-67-40, Volume 1, June 1967.

6. Blottner, F. G., "Chemical Nonequilibrium Boundary Layer," AIAA Paper No. 63-443, August 1963.

7. Fivel, H. J., and Masek, R. V., "Analytical Comparison of Hypersonic Flight and Wind Tunnel Viscous/Inviscid Flow Fields - Check Case and Users Manual," NASA CR-132359, July 1973.

8. Horton, T. E., "The JPL Thermochemistry and Normal Shock Computer Program," California Institute of Technology JPL Technical Report No. 32-660, 1 November 1964.

9. Cebeci, T., Smith, A.M.O., and Wang, L. D., "A Finite-Difference Method for Calculating Compressible Laminar and Turbulent Boundary Layers," McDonnell Douglas Report DAC-67131, Part I, March 1969.

10. Cebeci, T., Smith, A.M.O., and Mosinskis, G., "Calculation of Compressible Adiabatic Turbulent Boundary Layers," AIAA Paper No. 69-687, June 1969.

11. Fehrman, A. L. and Masek, R. V., "Study of Uncertainties of Predicting Space Shuttle Thermal Environment - Final Report," MDC Report E0639, June 1972.

12. Scottoline, C. A., "Determination of Aerothermodynamic Environment Uncertainties with Application to Space Shuttle Vehicles," Space Shuttle Aerothermodynamics Technology Conference, Vol. II - Heating, NASA TM X-2507, February 1972.

13. Johnson, C. B., "Boundary Layer Transition and Heating Criteria Applicable to Space Shuttle Configurations from Flight and Ground Tests," NASA Space Shuttle Technology Conference, Volume I-Aerothermodynamics, Configurations and Flight Mechanics, NASA TM X-2272, April 1971.

7.0 LIST OF SYMBOLS

CF	skin friction coefficient
C_p	specific heat
h	enthalpy
L	vehicle or model axial length
M	Mach number
P	pressure
PAR 1	transition parameter 1
PAR 2	transition parameter 2
Q	heating rate
$Q_{STAG, EQUIL}$	laminar equilibrium heating rate at the stagnation point
r	distance from axis of symmetry to location in the boundary layer
R_N	nose radius
Re	Reynolds number
Re_θ	momentum thickness Reynolds number
Re/ℓ	unit Reynolds number (m^{-1})
S	surface distance
ST	Stanton number
T	temperature
u	local streamwise velocity
v	local normal velocity
V	velocity
X	axial distance
X_S	axial shock swallowing length
X_T	axial location of transition
Y	radial distance from axis or distance through boundary layer
y_δ	distance normal from surface to location in inviscid flow field corresponding to boundary layer edge
γ	ratio of specific heats
δ	baoundary layer thickness
δ_{INNER}	turbulent boundary layer inner layer thickness

δ_{SUB}	turbulent boundary layer laminar sublayer thickness
δ^*	displacement thickness
Δ	shock standoff distance
θ	momentum thickness
μ	viscosity
ρ	density

Subscripts

D	nose diameter
e	boundary layer edge
E	equilibrium
EDGE	boundary layer edge
inv	inviscid solution
L	local conditions
LAM	laminar
NE	nonequilibrium
ref	reference conditions
S	stagnation
sonic	sonic point
TURB	turbulent
vis	boundary layer solution
∞	free stream
2	behind shock

Superscript

'	behind shock

TABLE I

TRANSPORT PROPERTIES FOR WIND TUNNEL GASES

GAS	γ	PRANDTL NUMBER	C_p (joules/g°K)	μ (N sec/cm^2)
AIR	1.4	0.70	1.01	$\mu_{ref}\left(\frac{h}{h_{ref}}\right)^{1.5}\left[\frac{h_{ref} + 1.1949 \times 10^6}{h + 1.1949 \times 10^6}\right]$
NITROGEN	1.4	0.70	1.05	
HELIUM	1.67	0.69	5.19	$5.03 \times 10^{-7}\ (T)^{0.649}$
FREON (CF_4)	1.12	0.65	0.88	$1.0 \times 10^{-6}\ (T)^{0.5} \Big/ \left[0.64625 + 103.0/T - 3.42714/T^2\right]$

* T in °K

** h_{ref} evaluated at static temperature behind normal shock

$$\mu_{ref} \times 10^6 = 0.07783\ T + 59.30 - \left[4.2222 \times 10^{-3} T^2 + 1.5810\ T + 3292.42\right]^{0.5}$$

TABLE II

CALCULATION MATRIX FOR FLIGHT

CASE	ALTITUDE		VELOCITY		L/R_N	CONE ANGLE	
	(km)	(ft)	(km/sec)	(ft/sec)		(radians)	(degrees)
F-1	76.2	250,000	7.32	24,000	50	0.524	30
F-2	70.1	230,000	7.32	24,000			
F-3	64.0	210,000	6.10	20,000			
F-4	64.0	210,000	4.88	16,000			
F-5	76.2	250,000	7.32	24,000	100		
F-6	70.1	230,000	7.32	24,000			
F-7	64.0	210,000	6.10	20,000			
F-8	64.0	210,000	4.88	16,000			
F-9	76.2	250,000	7.32	24,000	50	0.698	40
F-10	70.1	230,000	7.32	24,000			
F-11	64.0	210,000	6.10	20,000			
F-12	64.0	210,000	4.88	16,000			
F-13	76.2	250,000	7.32	24,000	100		
F-14	70.1	230,000	7.32	24,000			
F-15	64.0	210,000	6.10	20,000			
F-16	64.0	210,000	4.88	16,000			

TABLE III

AXIAL EXTENT OF HIGH ENTROPY INVISCID FLOW

ALTITUDE (km)	VELOCITY (km/sec)	L/R_N	CONE ANGLE (radians)	X_S/L			
				NONEQUILIBRIUM		EQUILIBRIUM	
				LAMINAR	TURBULENT	LAMINAR	TURBULENT
76.2	7.32	50	0.524	0.06	0.052	0.06	0.035
70.1	7.32			0.063	0.058	0.076	0.047
64.0	6.10			0.127	0.068	0.127	0.062
64.0	4.88			0.140	0.075	0.143	0.070
76.2	7.32	100		0.0177	0.014	0.0177	0.014
70.1	7.32			0.03	0.024	0.0265	0.019
64.0	6.10			0.039	0.030	0.039	0.027
64.0	4.88			0.045	0.034	0.043	0.031
76.2	7.32	50	0.698	0.025	0.0185	0.032	0.015
70.1	7.32			0.035	0.029	0.038	0.029
64.0	6.10			0.055	0.038	0.055	0.038
64.0	4.88			0.063	0.045	0.063	0.045
76.2	7.32	100		0.008	0.007	0.013	0.007
70.1	7.32			0.013	0.012	0.016	0.012
64.0	6.10			0.022	0.015	0.022	0.015
64.0	4.88			0.023	0.016	0.023	0.016

TABLE IV

INNER LAYER THICKNESS FOR FLIGHT TURBULENT BOUNDARY LAYERS

ALTITUDE (km)	VELOCITY (km/sec)	CONE ANGLE (RADIANS)	$\delta_{INNER}/L \times 10^5$	
			EQUILIBRIUM	NONEQUILIBRIUM
76.2	7.32	0.524	8.9	19.5
70.1	7.32		5.0	10.0
64.0	6.10		3.2	5.4
64.0	4.88		3.7	5.6
76.2	7.32	0.698	6.5	14.2
70.1	7.32		4.0	6.2
64.0	6.10		2.1	3.8
64.0	4.88		2.6	3.9

TABLE V

NONEQUILIBRIUM HEATING

AT THE STAGNATION POINT

ALTITUDE (km)	VELOCITY (km/sec)	Q_{NE}/Q_E	
		$L/R_N = 100$	$L/R_N = 50$
76.2	7.32	0.59	0.49
70.1	7.32	0.51	0.44
64.0	6.10	0.69	0.66
64.0	4.88	0.83	0.77

TABLE VI

RATIO OF NONEQUILIBRIUM TO EQUILIBRIUM HEATING AT BASE

ALTITUDE (km)	VELOCITY (km/sec)	Q_{NE}/Q_E – LAMINAR		Q_{NE}/Q_E – TURBULENT	
		$R_N/L = 0.01$	$R_N/L = 0.02$	$R_N/L = 0.01$	$R_N/L = 0.02$
76.2	7.32	0.75	0.72	0.62	0.60
70.1	7.32	0.72	0.70	0.59	0.58
64.0	6.10	0.86	0.80	0.60	0.60
64.0	4.88	0.92	0.83	0.65	0.65

TABLE VII

PREDICTED FLIGHT TRANSITION LOCATION

ALTITUDE (km)	VELOCITY (km/sec)	CONE ANGLE (RADIANS)	L/R_N	X_T/L							
				NONEQUILIBRIUM				EQUILIBRIUM			
				Re_Θ/M_L=150	Re_Θ/M_L=200	PAR 1=10	PAR 2= 2.3×10^6	Re_Θ/M_L=150	Re_Θ/M_L=200	PAR 1=10	PAR 2= 2.3×10^6
76.2	7.32	0.524	50	> 1	> 1	0.65	0.82	> 1	> 1	0.69	0.61
70.1	7.32	↓	↓	> 1	> 1	0.39	0.33	> 1	> 1	0.38	0.24
64.0	6.10	↓	↓	0.95	> 1	0.06	0.19	0.94	> 1	0.155	0.18
64.0	4.88	↓	↓	0.94	> 1	0.054	0.34	0.93	> 1	0.135	0.34
76.2	7.32	0.524	100	> 1	> 1	0.63	0.82	> 1	> 1	0.69	0.61
70.1	7.32	↓	↓	> 1	> 1	0.38	0.33	> 1	> 1	0.39	0.24
64.0	6.10	↓	↓	0.91	> 1	0.28	0.18	0.89	> 1	0.24	0.18
64.0	4.88	↓	↓	0.97	> 1	0.27	0.34	0.91	> 1	0.24	0.34
76.2	7.32	0.698	50	> 1	> 1	0.34	0.72	> 1	> 1	0.37	0.57
70.1	7.32	↓	↓	> 1	> 1	0.20	0.28	1.00	> 1	0.21	0.23
64.0	6.10	↓	↓	0.50	0.87	0.02	0.13	0.47	0.84	0.115	0.155
64.0	4.88	↓	↓	0.51	0.89	0.02	0.24	0.49	0.86	0.02	0.24
76.2	7.32	0.698	100	> 1	> 1	0.34	0.72	> 1	> 1	0.37	0.57
70.1	7.32	↓	↓	> 1	> 1	0.192	0.29	> 1	> 1	0.215	0.23
64.0	6.10	↓	↓	0.50	0.90	0.12	0.13	0.48	0.86	0.12	0.155
64.0	4.88	↓	↓	0.51	0.90	0.138	0.24	0.48	0.86	0.13	0.24

TABLE VIII

RATIO OF NONEQUILIBRIUM TO EQUILIBRIUM VALUE OF TRANSITION PARAMETERS AT END OF CONE

ALTITUDE (km)	VELOCITY (km/sec	CONE ANGLE (RADIANS)	L/R_N	$PAR]_{NE} / PAR]_E$			
				Re_L	Re_θ/M_L	PAR 1	PAR 2
76.2	7.32	0.524	50	0.64	0.87	0.93	0.75
70.1	7.32	↓	↓	1.0	0.89	0.93	0.82
64.0	6.10			1.0	0.97	0.96	1.0
64.0	4.88			1.0	0.98	0.95	1.0
76.2	7.32	0.524	100	0.64	0.86	1.0	0.75
70.1	7.32	↓	↓	0.71	0.89	0.96	0.82
64.0	6.10			1.0	0.96	1.0	1.0
64.0	4.88			1.0	0.98	0.95	1.0
76.2	7.32	0.698	50	0.73	0.95	1.01	0.85
70.1	7.32	↓	↓	0.80	0.96	1.01	0.94
64.0	6.10			1.0	0.97	0.95	1.0
64.0	4.88			1.0	0.98	0.98	1.0
76.2	7.32	0.698	100	0.69	0.97	1.04	0.85
70.1	7.32	↓	↓	0.80	0.99	1.03	0.94
64.0	6.10			1.0	0.97	0.97	1.0
64.0	4.88			1.0	0.97	0.98	1.0

TABLE IX

SUMMARY OF WIND TUNNEL CASES

CASE	TEST GAS	MACH NUMBER	SPECIFIC HEAT RATIO	TOTAL TEMPERATURE		TOTAL PRESSURE		CONE ANGLE		L/R_N
				(K)	(F)	(N/m^2)	(psi)	(radians)	(degrees)	
T-1	*AIR	8	1.4	812	1000	3.45×10^6	500	0.524	30	100
T-2										50
T-3								0.698	40	100
T-4										50
T-5						2.07×10^7	3000	0.524	30	100
T-6										50
T-7								0.698	40	100
T-8										50
T-9	**NITROGEN	20	1.4	1644	2500	1.38×10^7	2000	0.524	30	100
T-10										50
T-11								0.698	40	100
T-12										50
T-13						5.52×10^7	8000	0.524	30	100
T-14										50
T-15								0.698	40	100
T-16										50
T-17	*HELIUM	20	1.67	590	600	6.89×10^6	1000	0.524	30	100
T-18										50
T-19								0.698	40	100
T-20										50
T-21	*FREON	6.2	1.12	700	800	2.28×10^6	330	0.524	30	100
T-22										50
T-23								0.698	40	100
T-24										50
T-25						1.32×10^7	1915	0.524	30	100
T-26										50
T-27								0.698	40	100
T-28										50

* MODEL LENGTH 0.214m (0.7 FT) ** MODEL LENGTH 0.153m (0.5 FT)

TABLE X

SUBLAYER THICKNESS FOR TUNNEL TURBULENT BOUNDARY LAYERS

GAS	PRESSURE (N/m^2)	$\delta_{SUB}/L \times 10^5$	
		0.524 rad	0.698 rad
AIR	3.45×10^6	14.0	11.4
	2.07×10^7	2.8	2.1
NITROGEN	1.38×10^7	336.0	270.0
	5.52×10^7	95.0	77.0
HELIUM	6.89×10^6	57.0	46.0
FREON	2.28×10^6	70.0	54.0
	1.32×10^7	14.0	11.0

TABLE XI

WIND TUNNEL HEATING RATE DISTRIBUTION FOR 0.524 RADIAN (30^{o}) CONES

GAS	PRESSURE (N/m^2)	L/R_N	Q/Q_S			
			X/L = 0.002	X/L = 0.006	X/L = 0.1	X/L = 1
AIR	3.45×10^6	100	0.715	0.325	0.152	0.055
	2.07×10^7		0.71	0.32	0.15	0.05
NITROGEN	1.38×10^7		0.76	0.465	0.125	0.042
	5.52×10^6		0.74	0.39	0.14	0.045
HELIUM	6.89×10^6		0.765	0.3	0.145	0.42
FREON	2.28×10^7		0.735	0.355	0.114	0.038
	1.32×10^7		0.715	0.315	0.13	0.045
AIR	3.45×10^6	50	0.85	0.56	0.19	0.065
	2.07×10^7		0.86	0.58	0.17	0.065
NITROGEN	1.38×10^7		0.84	0.63	0.18	0.06
	5.52×10^6		0.84	0.595	0.20	0.065
HELIUM	6.89×10^6		0.84	0.56	0.172	0.055
FREON	2.28×10^7		0.825	0.56	0.150	0.055
	1.32×10^7		0.83	0.56	0.195	0.065

TABLE XII

WIND TUNNEL HEATING RATE DISTRIBUTION FOR 0.698 RADIAN (40^{o}) CONES

GAS	PRESSURE (N/m^2)	L/R_N	Q/Q_S			
			X/L = 0.002	X/L = 0.006	X/L = 0.1	X/L = 1
AIR	3.45×10^6	100	0.73	0.40	0.15	0.05
	2.07×10^7		0.71	0.40	0.165	0.055
NITROGEN	1.38×10^7		0.76	0.47	0.14	0.045
	5.52×10^6		0.74	0.435	0.155	0.05
HELIUM	6.89×10^6		0.70	0.39	0.144	0.045
FREON	2.28×10^7		0.74	0.395	0.132	0.045
	1.32×10^7		0.72	0.415	0.155	0.05
AIR	3.45×10^6	50	0.84	0.55	0.24	0.07
	2.07×10^7		0.84	0.57	0.20	0.075
NITROGEN	1.38×10^7		0.84	0.635	0.19	0.065
	5.52×10^6		0.82	0.595	0.205	0.07
HELIUM	6.89×10^6		0.845	0.558	0.195	0.065
FREON	2.28×10^7		0.82	0.565	0.18	0.06
	1.32×10^7		0.825	0.555	0.203	0.07

TABLE XIII

PREDICTED TUNNEL TRANSITION LOCATION

GAS	PRESSURE (N/m^2)	CONE ANGLE (RADIANS)	* L/R_N	X_T/L			
				Re_θ/M_L = 150	Re_θ/M_L = 200	PAR 1 = 10	PAR 2 = 2.3×10^6
AIR	3.45×10^6	0.524		0.98	> 1	> 1	> 1
		0.698		0.56	> 1	0.70	> 1
	2.07×10^7	0.524	100	0.18	0.27	0.46	0.32
			50	0.19	0.34	0.53	0.32
		0.698	100	0.10	0.15	0.22	0.29
			50	0.098	0.21	0.26	0.28
NITROGEN	1.38×10^7	0.524		> 1	> 1	> 1	> 1
		0.698		↓	↓	↓	↓
	5.52×10^7	0.524					
		0.698					
HELIUM	6.89×10^6	0.524		> 1	> 1	> 1	> 1
		0.698		> 1	> 1	0.89	> 1
FREON	2.28×10^6	0.524		> 1	> 1	> 1	> 1
		0.698		↓	↓	↓	↓
	1.32×10^7	0.524					
		0.698					

* NOSE RADIUS EFFECTS IMPORTANT FOR HIGH PRESSURE AIR CASES ONLY.

TABLE XIV

DISPLACEMENT THICKNESS AT SONIC POINT ON NOSE

GAS	PRESSURE (N/m^2)	L/R_N	δ^*_{SONIC}/L	S_{SONIC}/L
AIR ↓	3.45×10^6 ↓	100	4.03×10^{-5}	6.8×10^{-3}
		50	5.7×10^{-5}	13.8×10^{-3}
		16.67	9.7×10^{-5}	41.1×10^{-3}
	2.07×10^7 ↓	100	1.7×10^{-5}	6.8×10^{-3}
		50	2.37×10^{-7}	13.8×10^{-3}
		16.67	4.1×10^{-7}	41.1×10^{-3}

TABLE XV

COMPARISON OF TRANSITION PARAMETERS AT END OF CONE

CONDITION/GAS	CONE ANGLE (RADIANS)	Re_L (MILLIONS)	Re_θ/M_L	PAR 1	PAR 2 (MILLIONS)
AIR	0.524	1.46-8.8	150-370	8.4-14.4	1.18-7.2
NITROGEN		0.023-0.11	19.2-37.8	2.3-3.4	0.04-0.16
HELIUM		0.49	101	7.0	0.35
FREON		0.17-1.04	35.3-97	3.4-5.8	0.09-0.54
FLIGHT (EQUILIBRIUM)		1.02-3.3	77.4-174	12.6-21.2	3.75-12.5
FLIGHT (NONEQUILIBRIUM)		0.65-3.3	66.5-168	12.2-21	2.8-12.5
AIR	0.698	1.12-6.7	197-483	12-19.9	1.3-7.8
NITROGEN		0.023-0.079	26-51.3	3.5-4.95	0.04-0.173
HELIUM		0.33	137	10.6	0.37
FREON		0.18-1.1	52.5-129	4.6-7.8	0.12-0.72
FLIGHT (EQUILIBRIUM)		0.8-3.4	94-230	16.5-29.7	4.04-14.6
FLIGHT (NONEQUILIBRIUM)		0.55-3.8	91-222	17-28.6	3.4-14.6

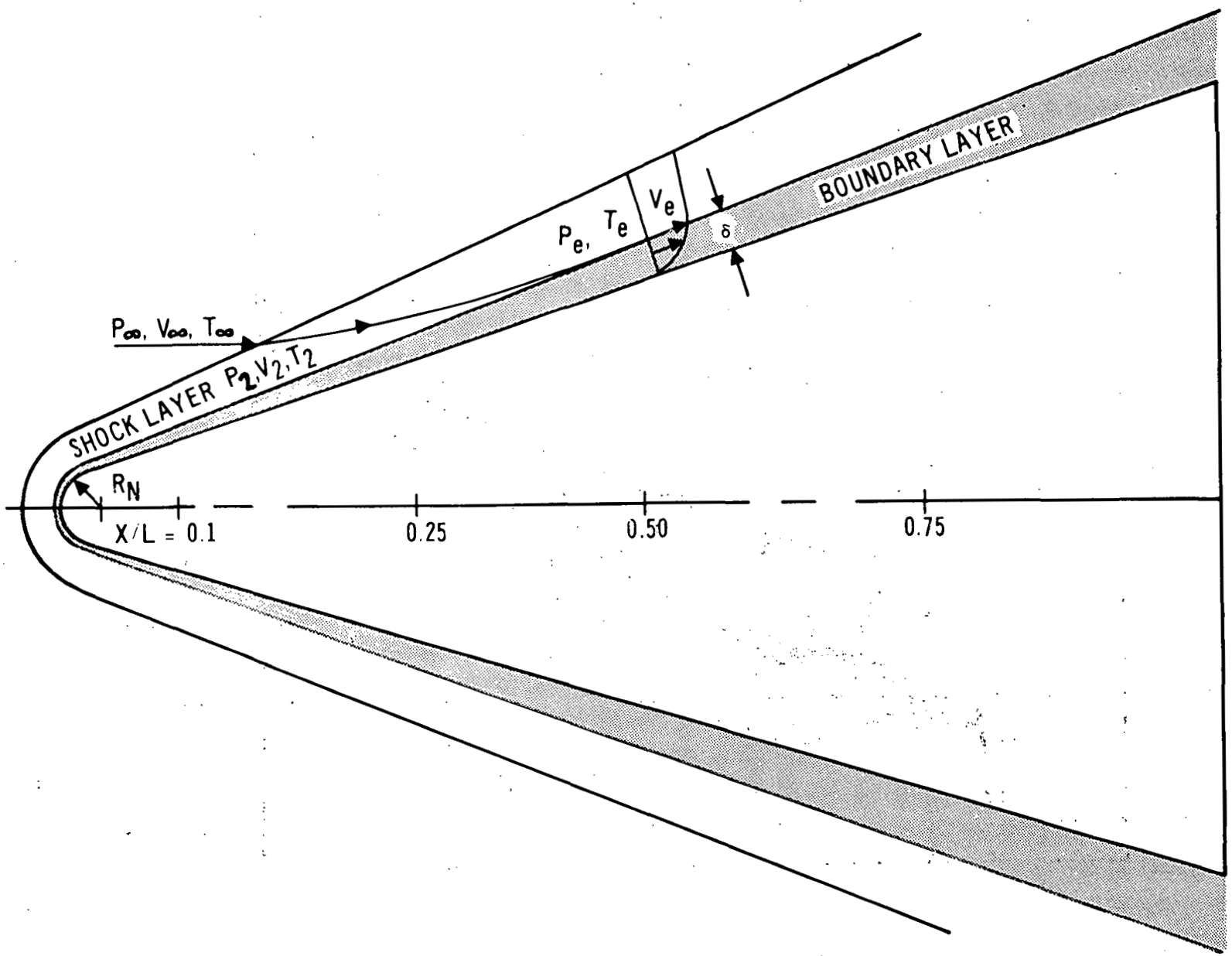

Figure 1. - Blunt Cone Flow Field.

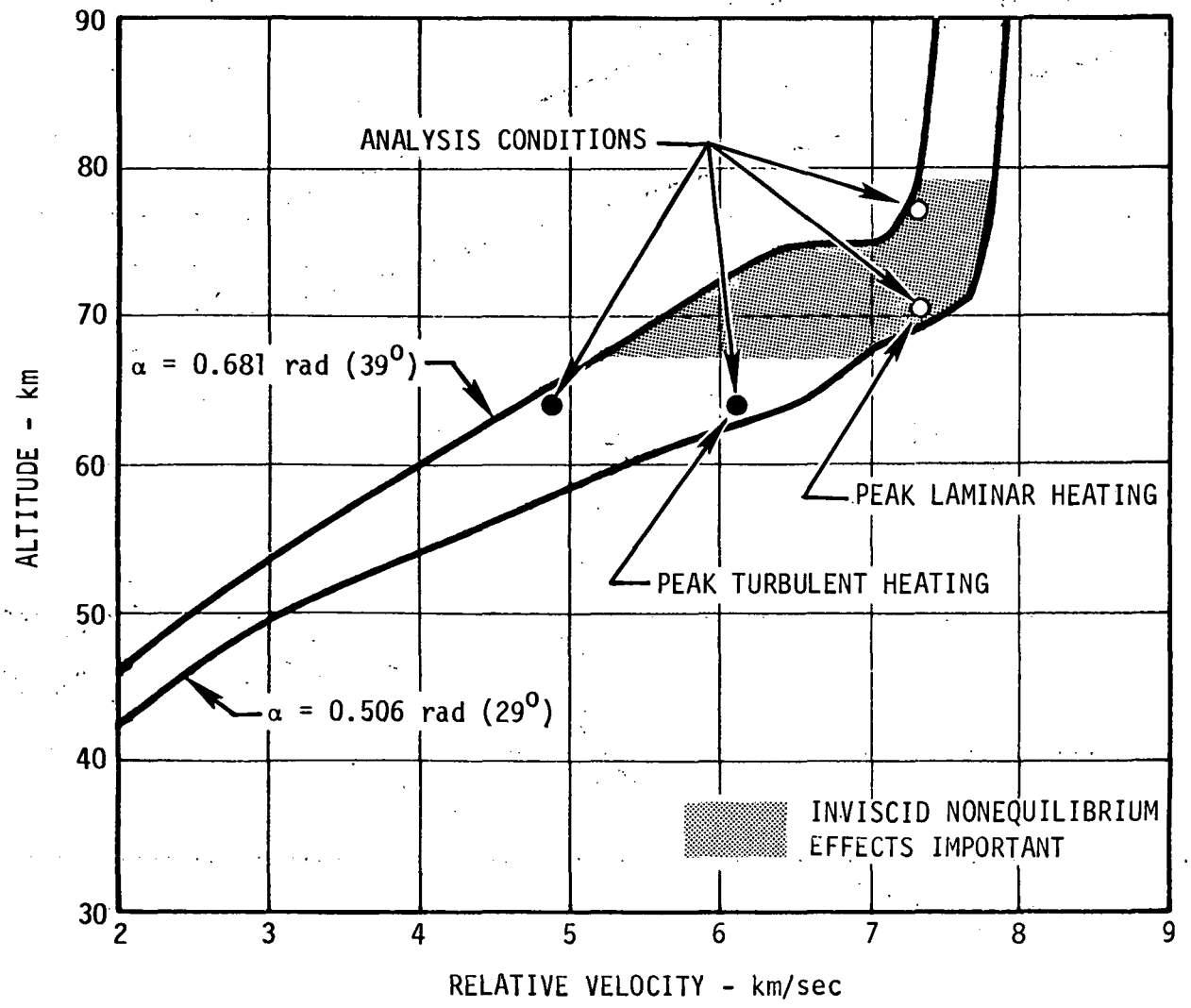

Figure 2. - Analysis Conditions Within the Shuttle Flight Envelope.

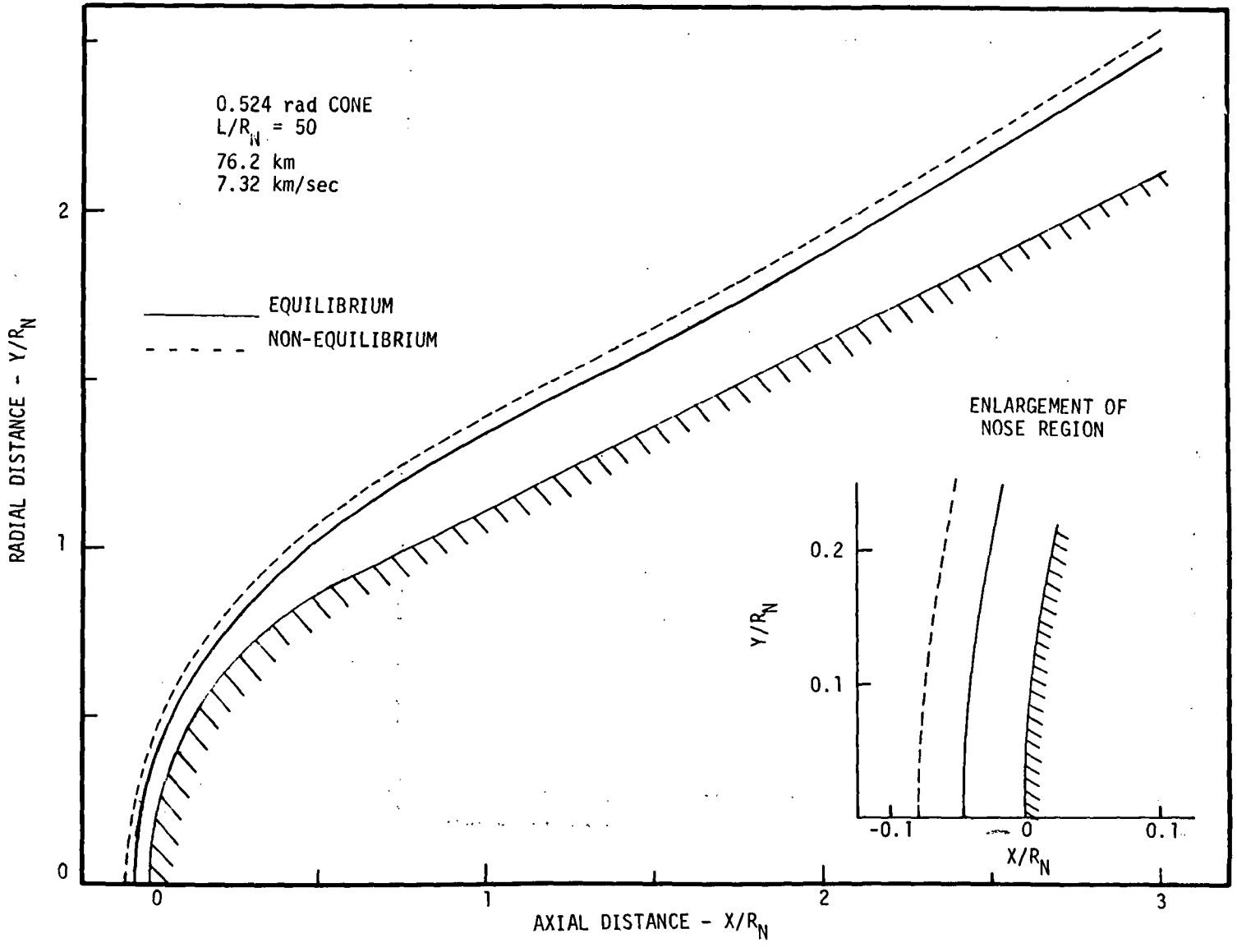

Figure 3. - Comparison of Equilibrium and Nonequilibrium Shock Shapes.

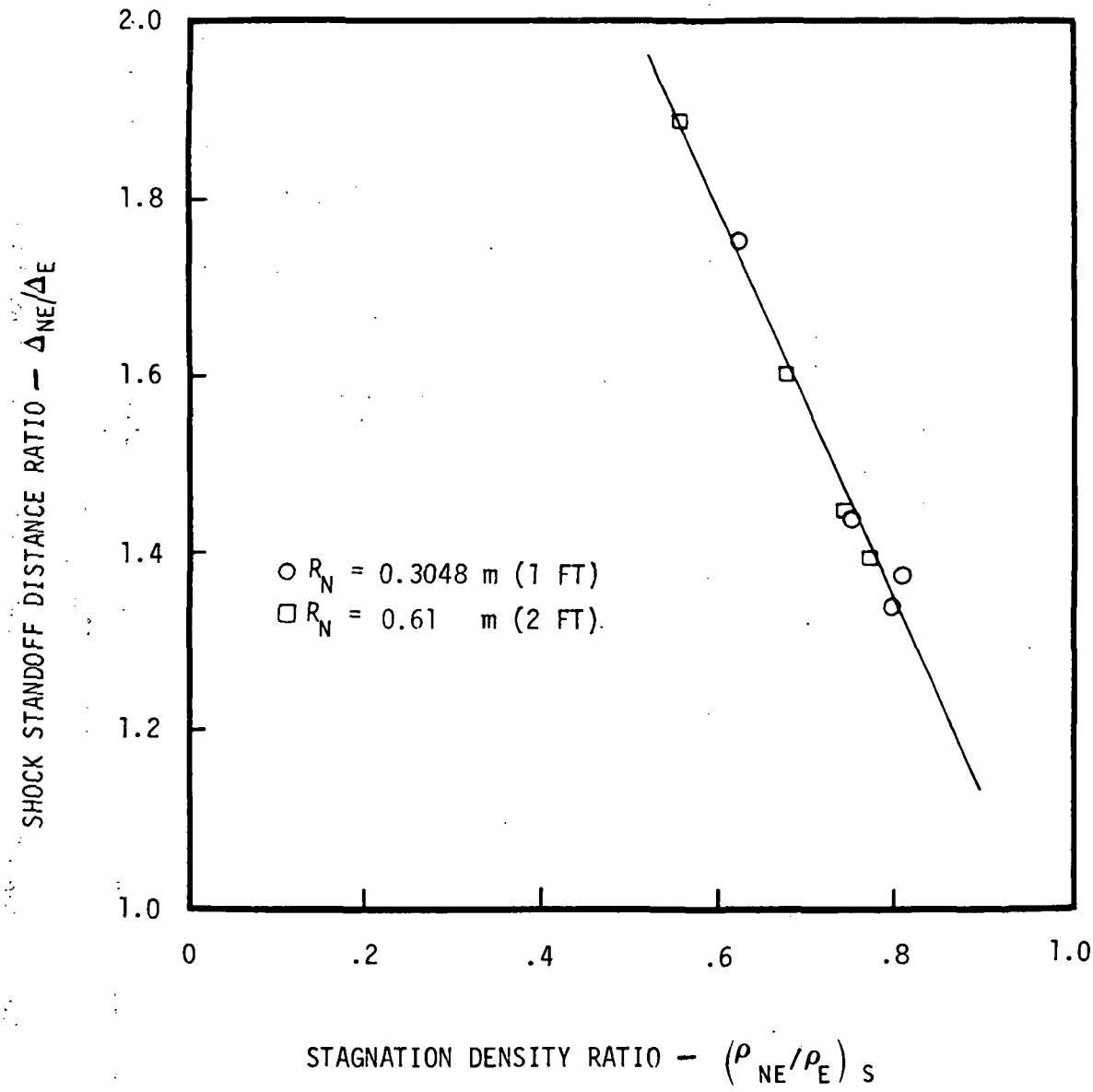

Figure 4. – Nonequilibrium Effects on Shock Standoff Distance.

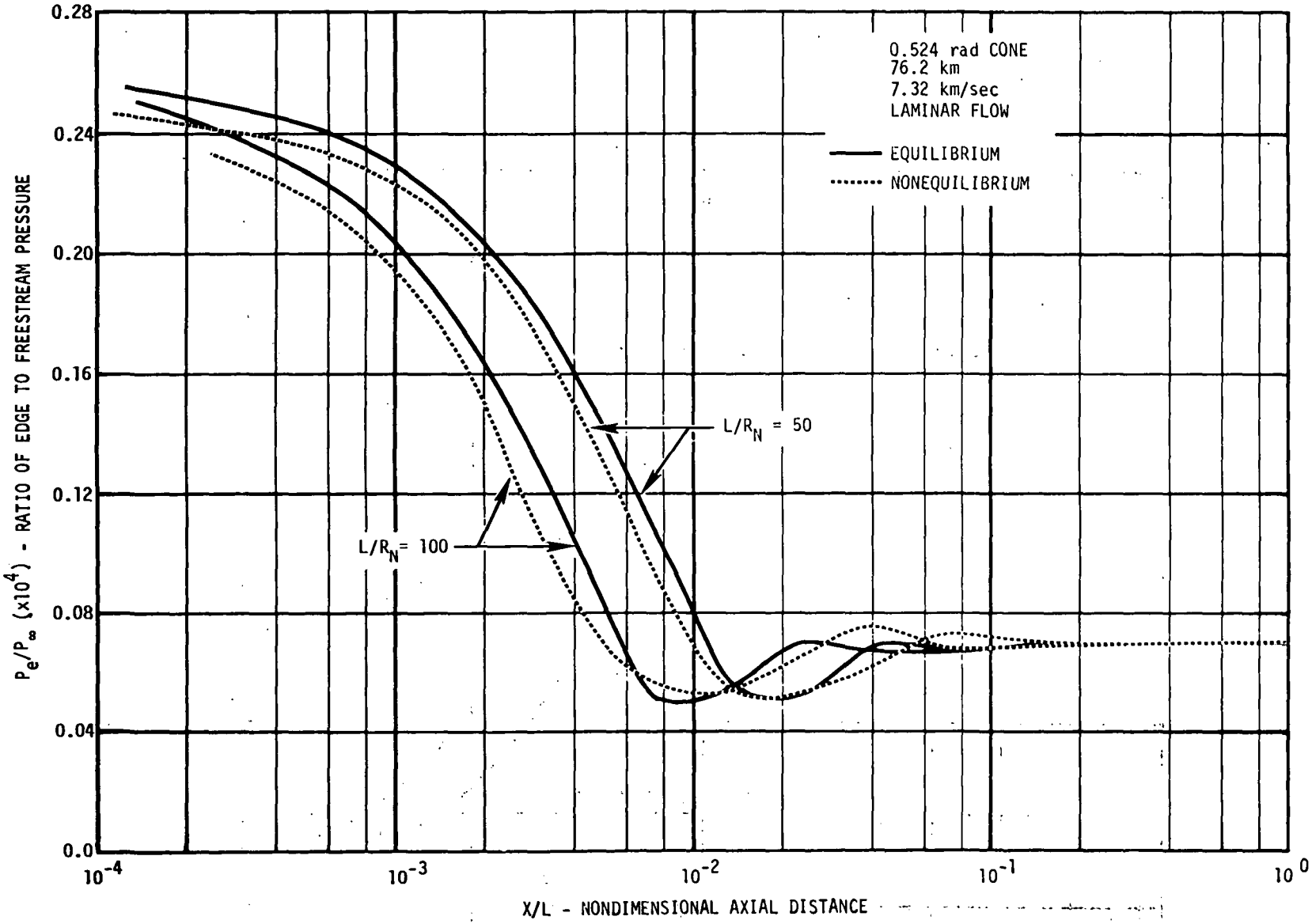

Figure 5. - Boundary Layer Edge Static Pressure Distribution at 76.2 km.

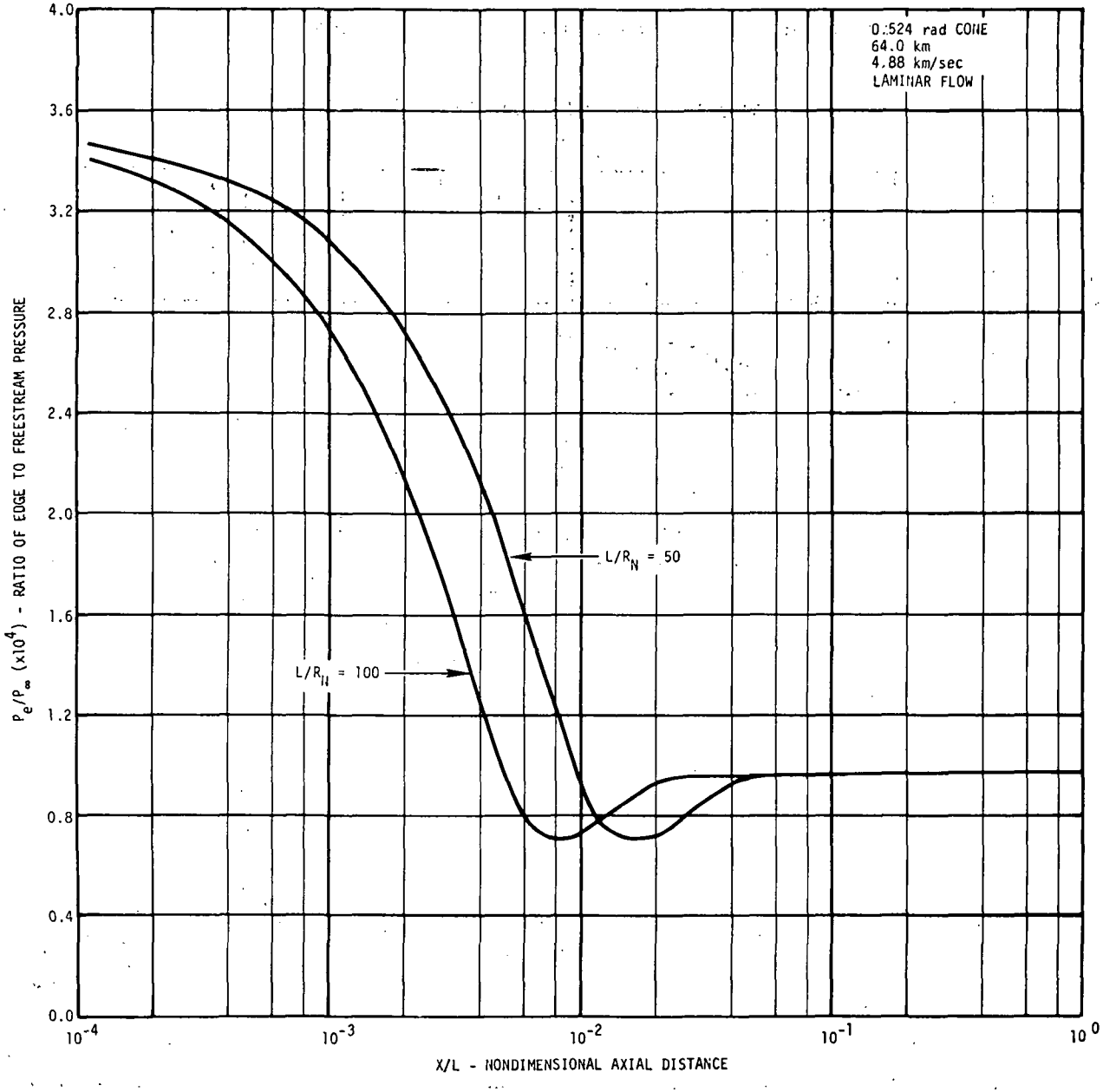

Figure 6. - Boundary Layer Edge Static Pressure Distribution at 64.0 km.

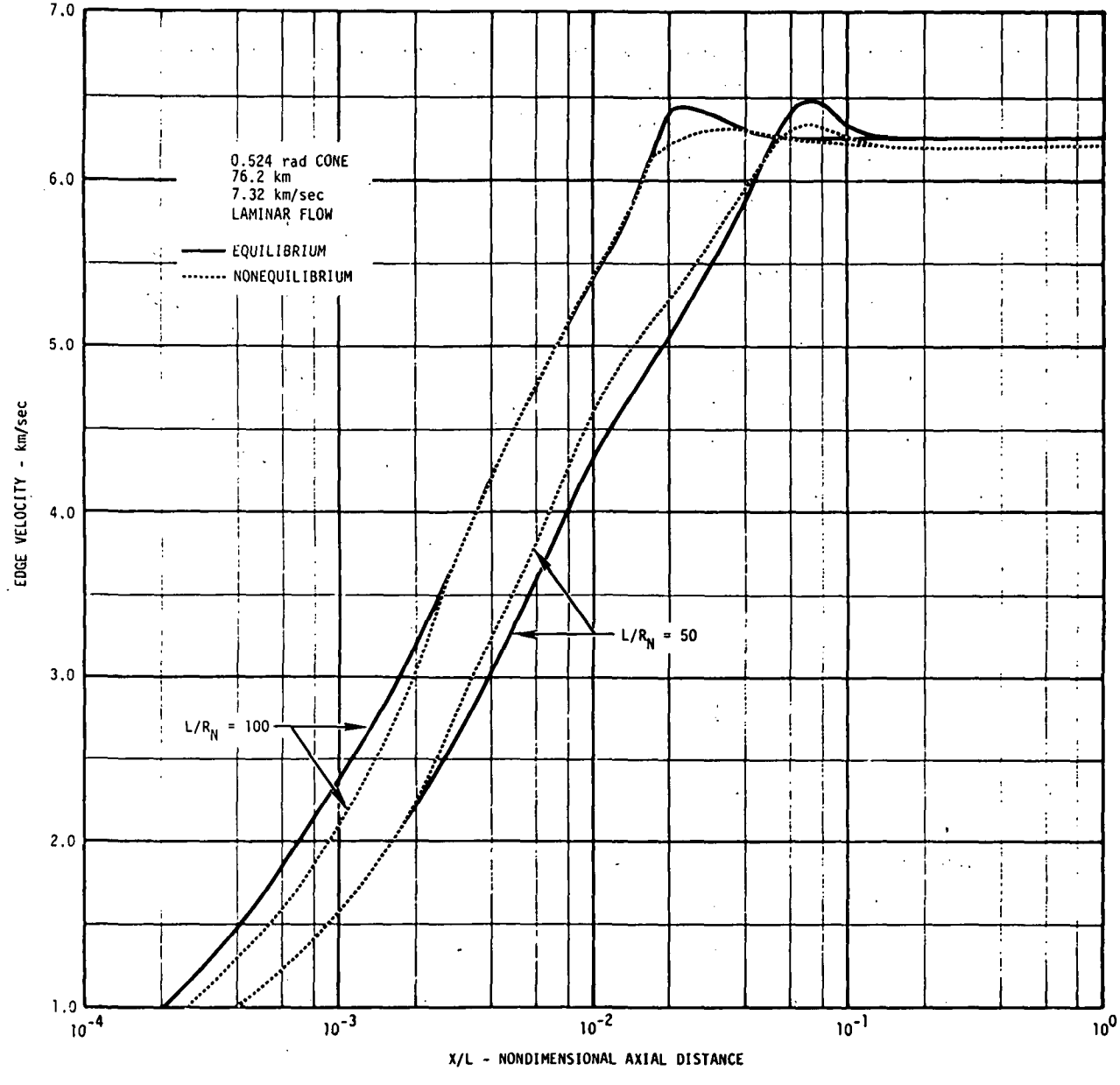

Figure 7. - Laminar Boundary Layer Edge Velocity Distribution at 76.2 km.

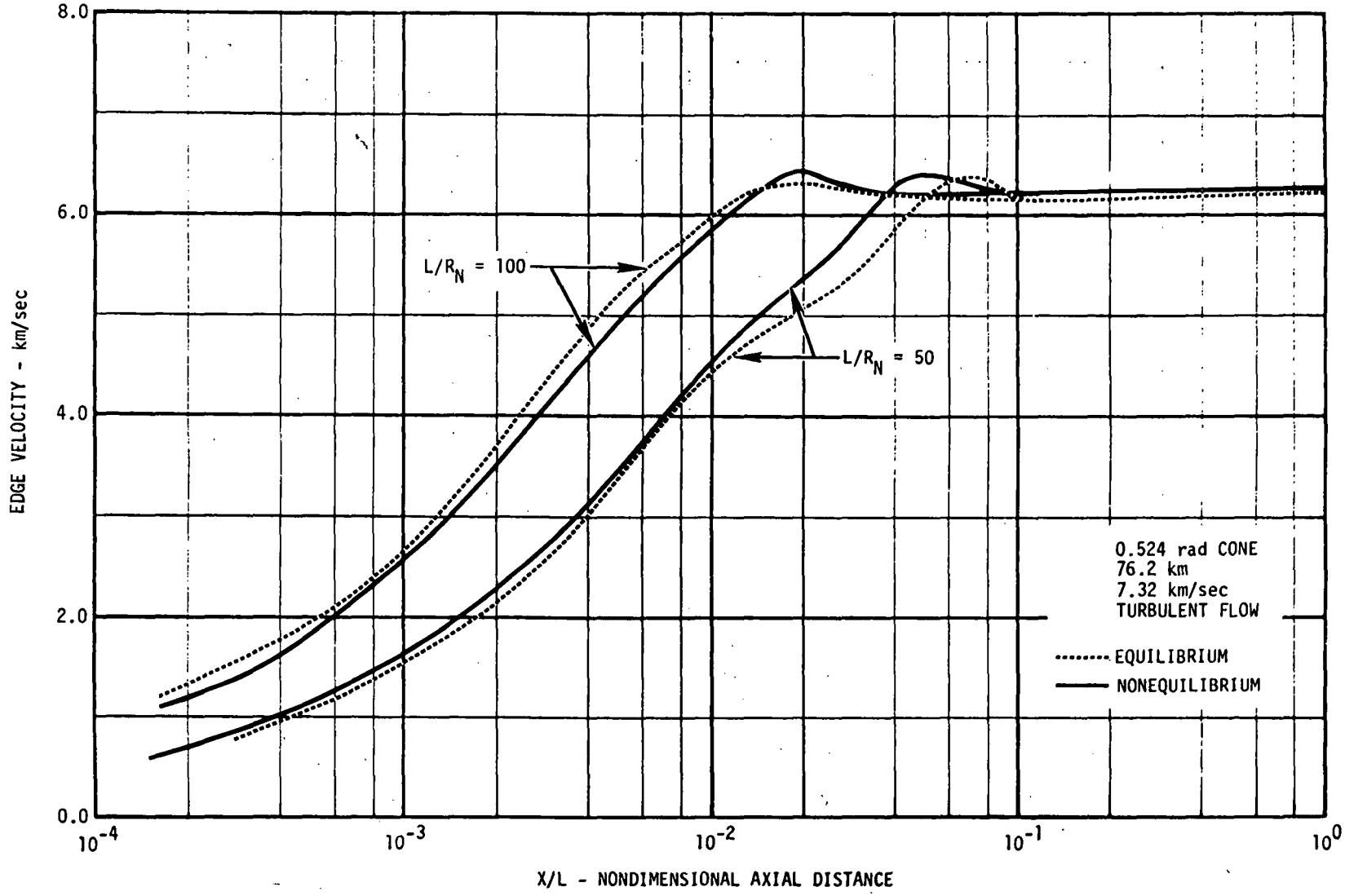

Figure 8. - Turbulent Boundary Layer Edge Velocity Distribution at 76.2 km.

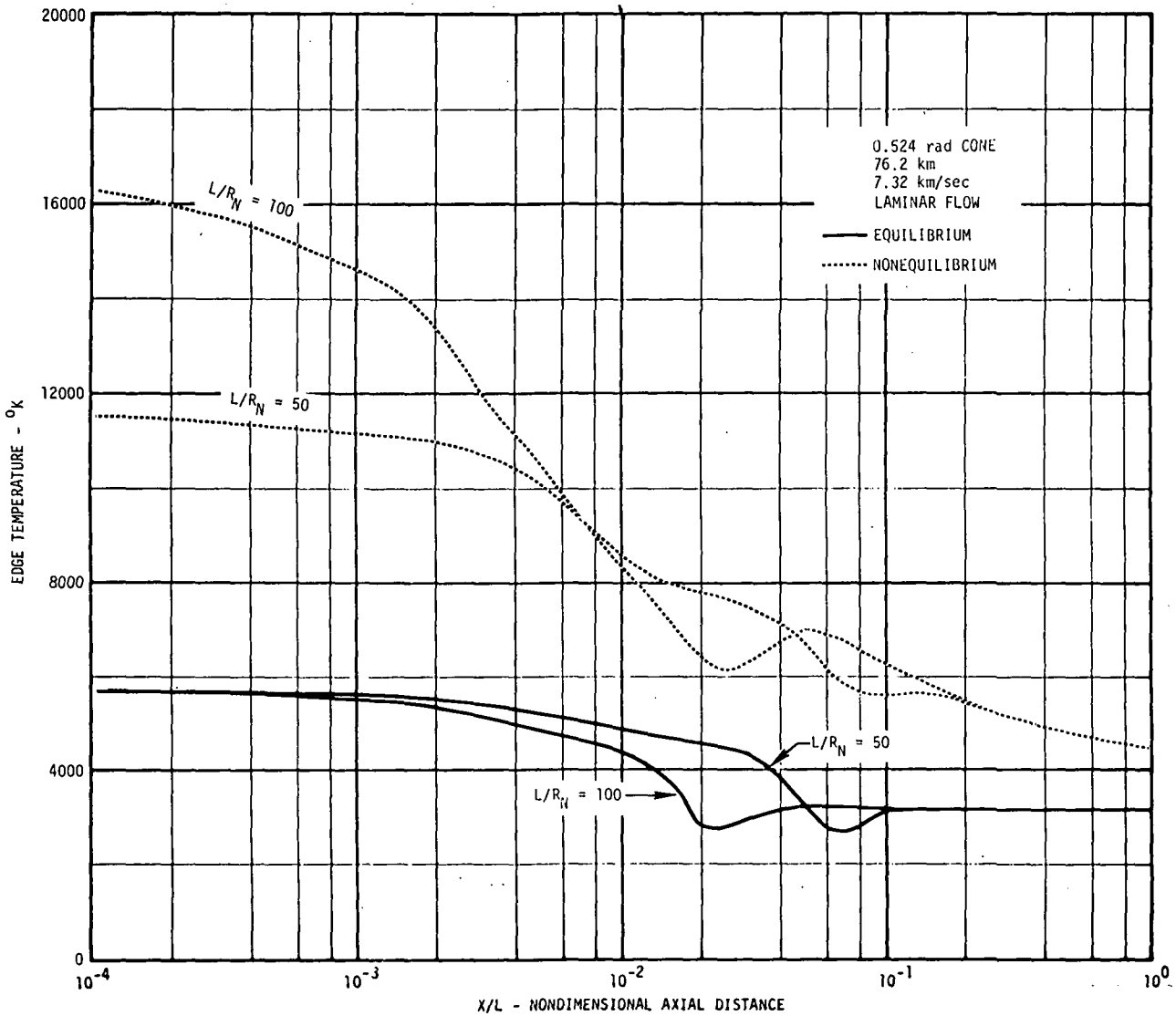

Figure 9. - Laminar Boundary Layer Edge Temperature Distribution at 76.2 km.

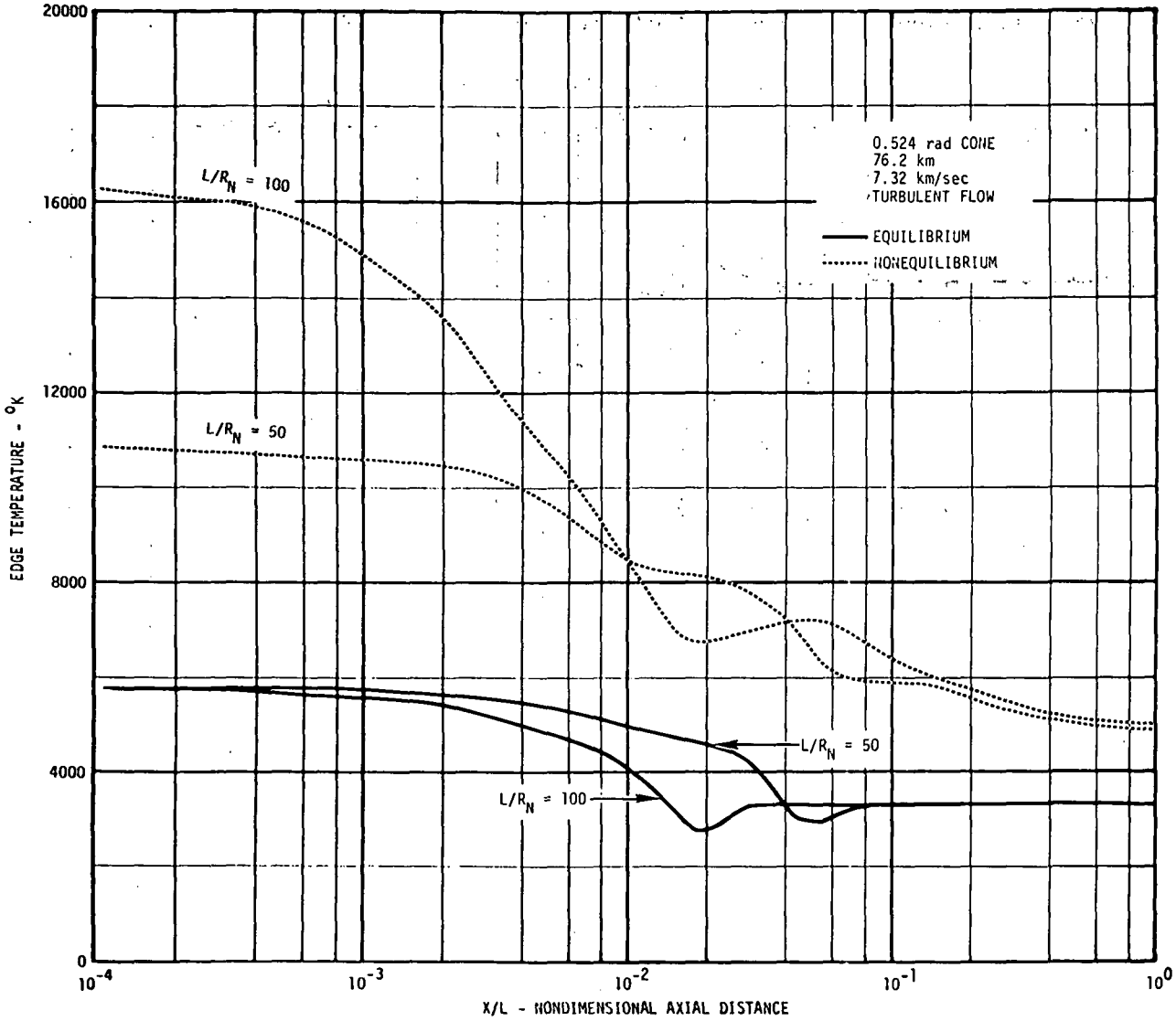

Figure 10. - Turbulent Boundary Layer Edge Temperature Distribution at 76.2 km.

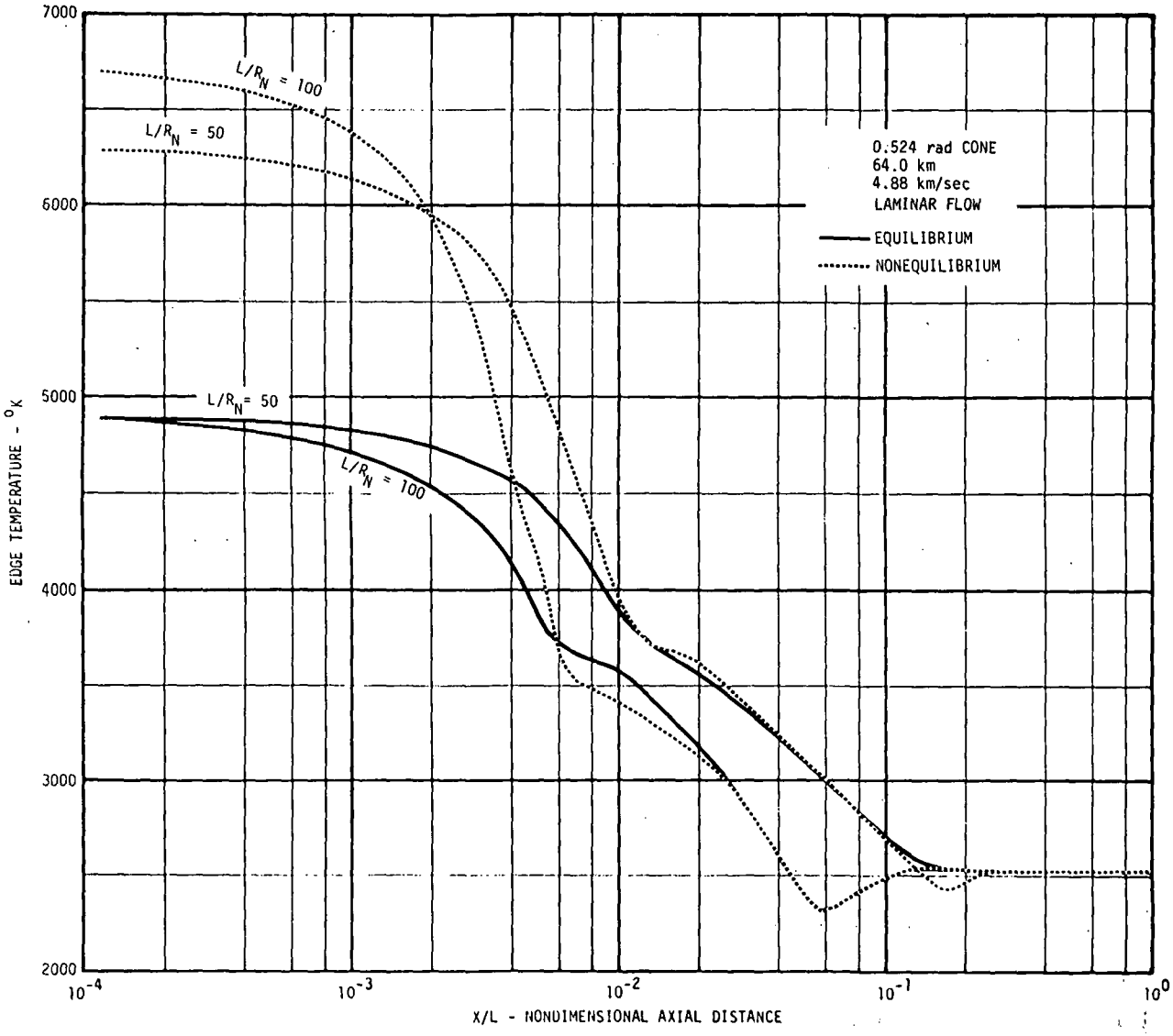

Figure 11. - Laminar Boundary Layer Edge Temperature Distribution at 64.0 km.

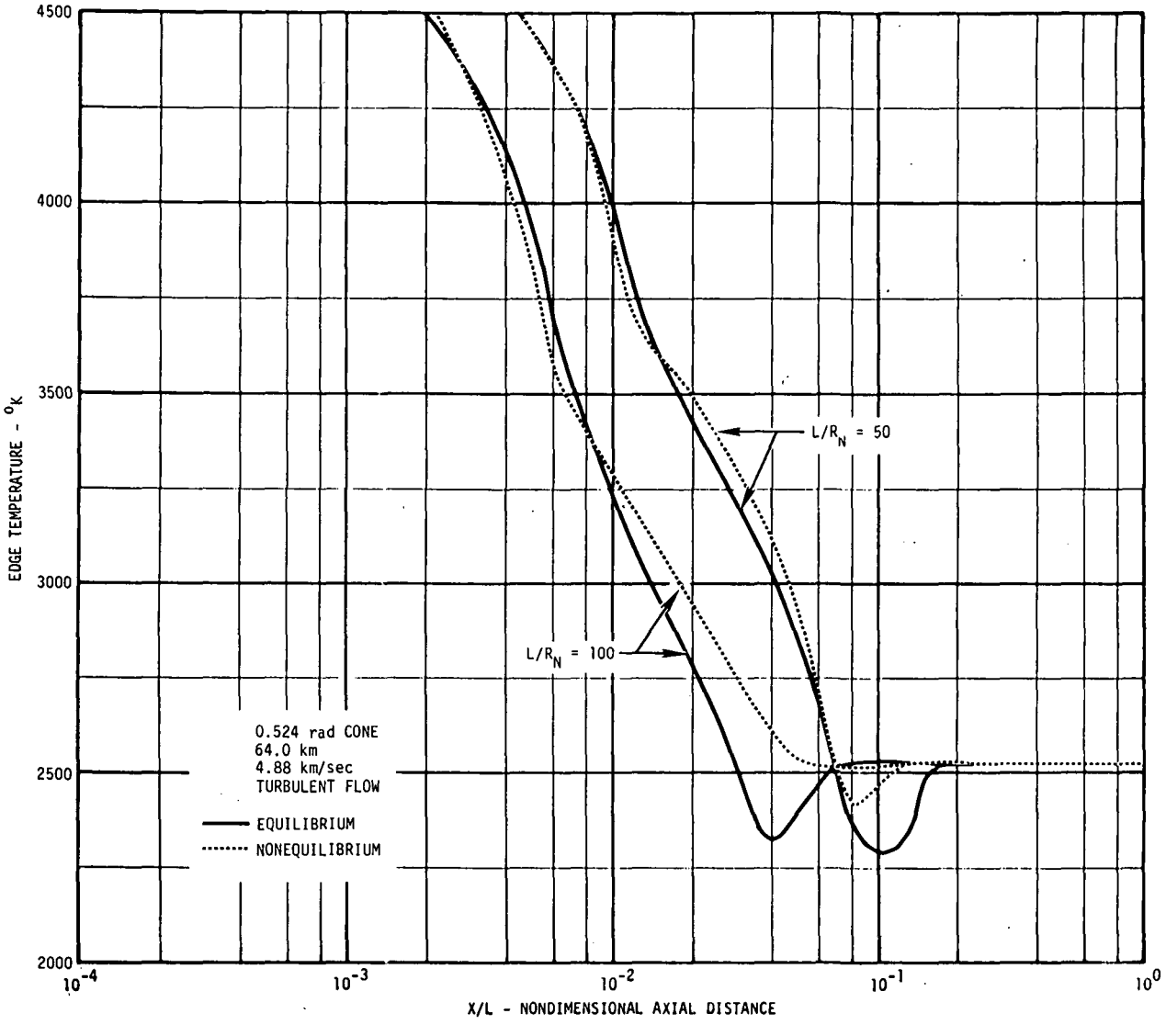

Figure 12. - Turbulent Boundary Layer Edge Temperature Distribution at 64.0 km.

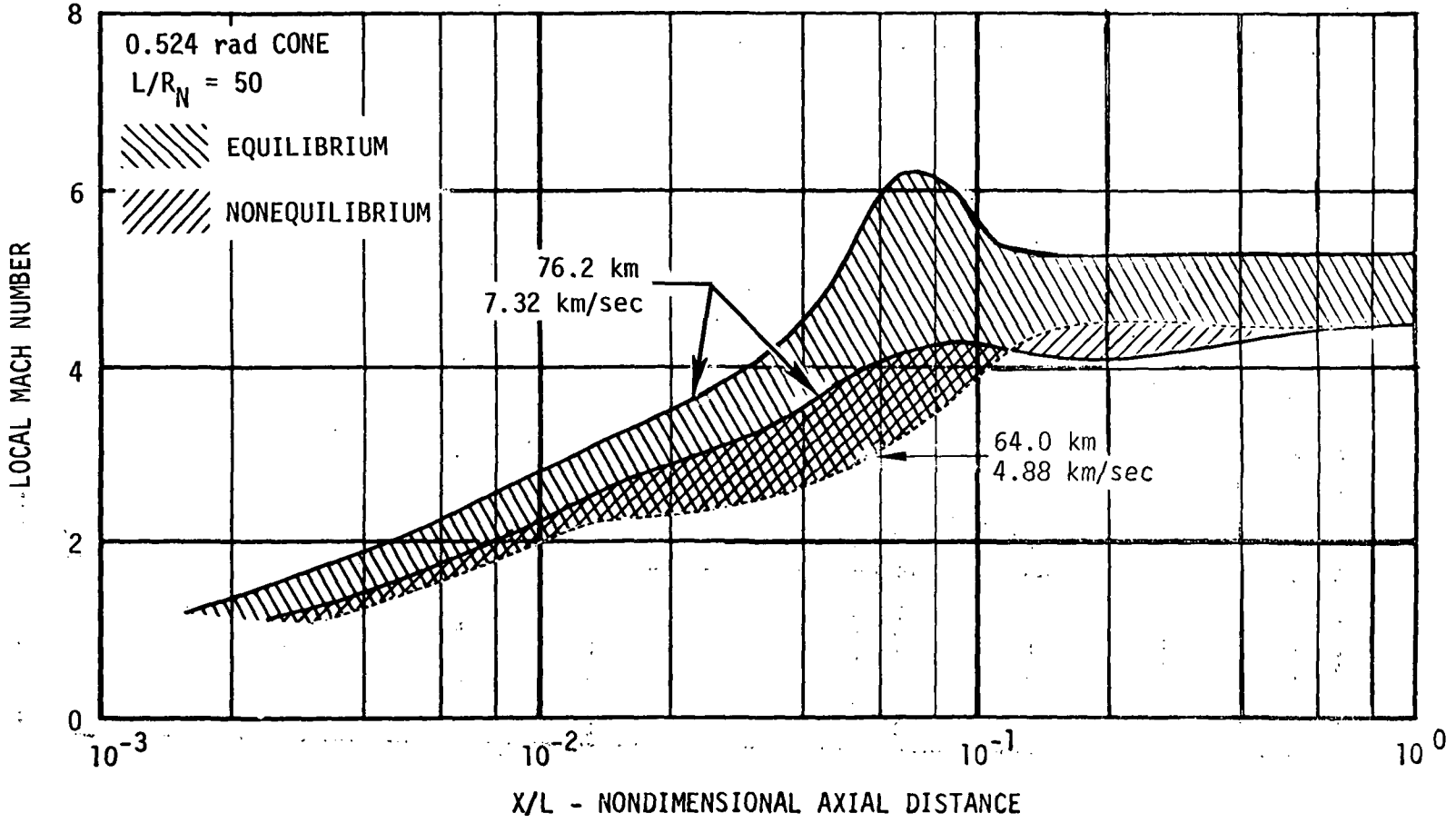

Figure 13. - Flight Boundary Layer Edge Mach Number Range for 0.524 rad Cones.

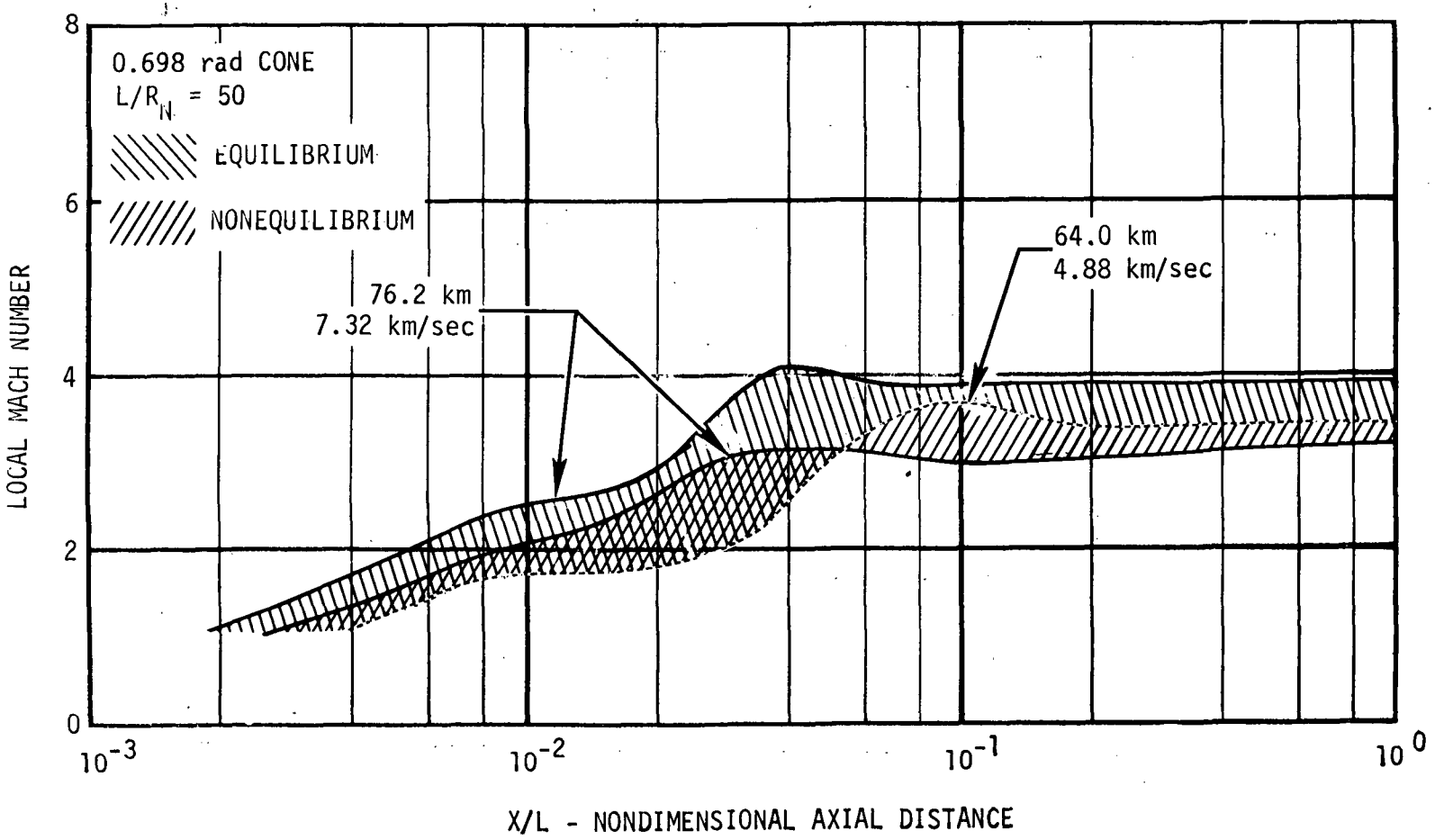

Figure 14. - Flight Boundary Layer Edge Mach Number Range for 0.698 rad Cones.

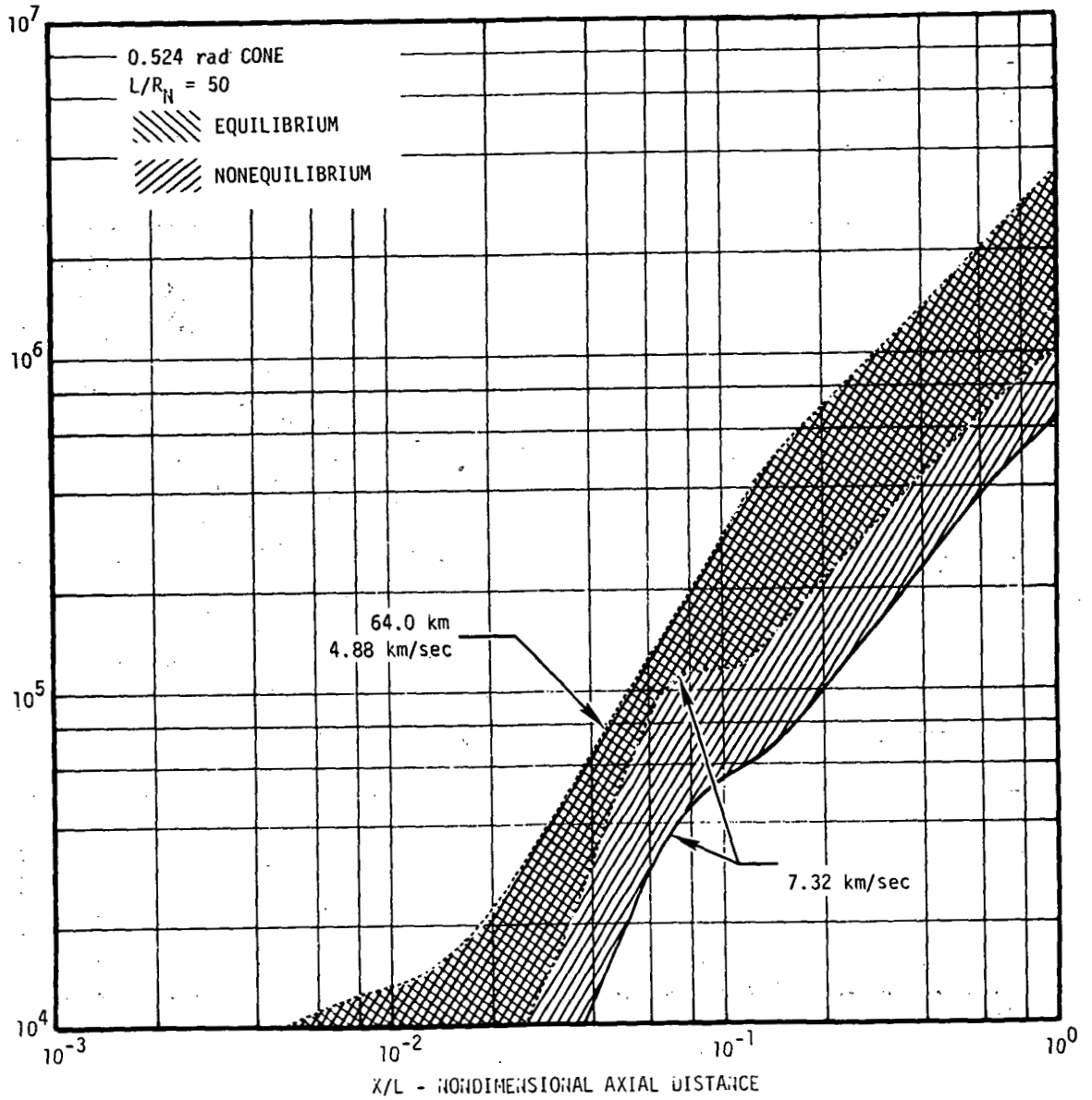

Figure 15. - Flight Local Reynolds Number Range for 0.524 rad Cones.

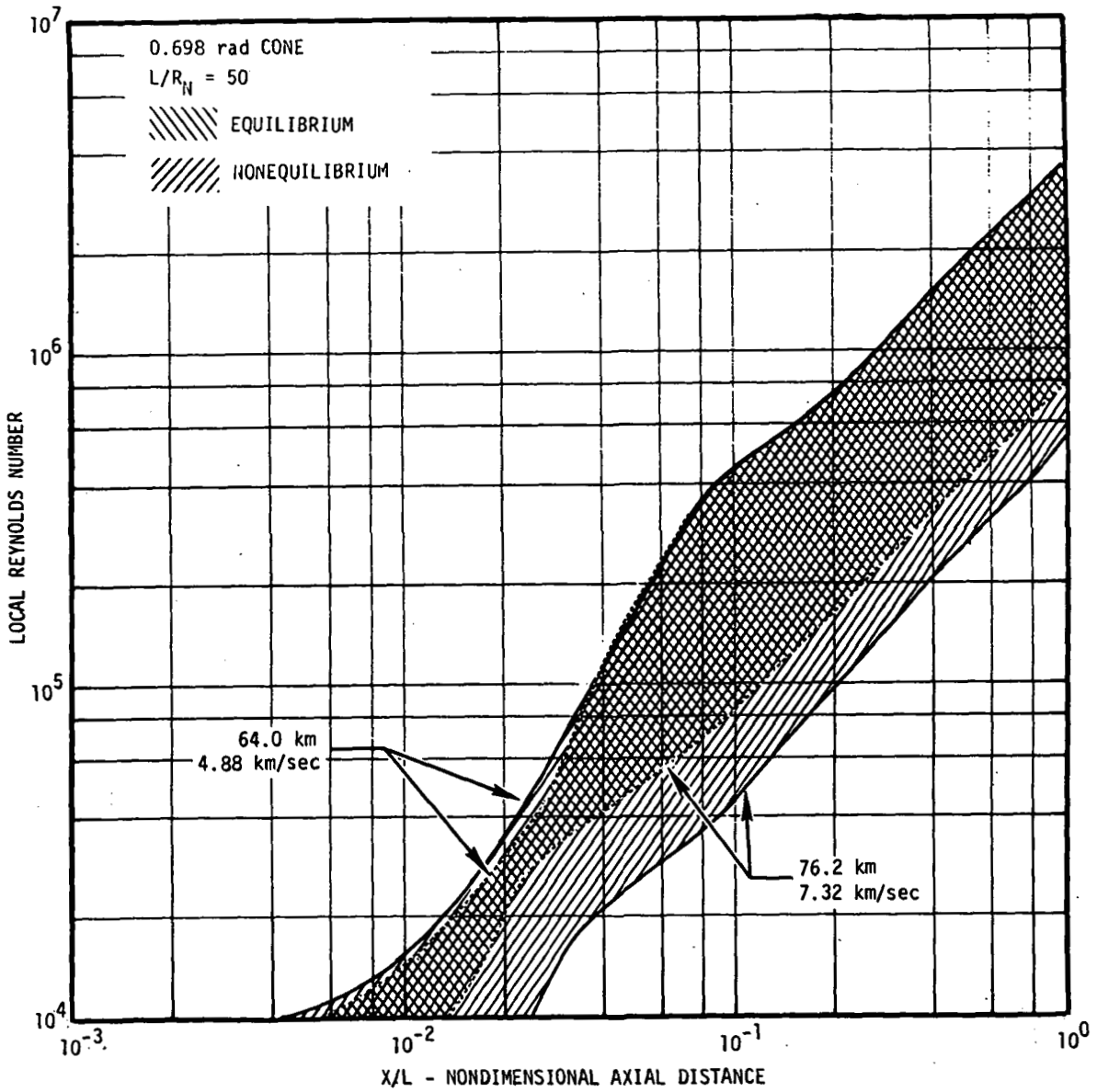

Figure 16. - Flight Local Reynolds Number Range for 0.698 rad Cones.

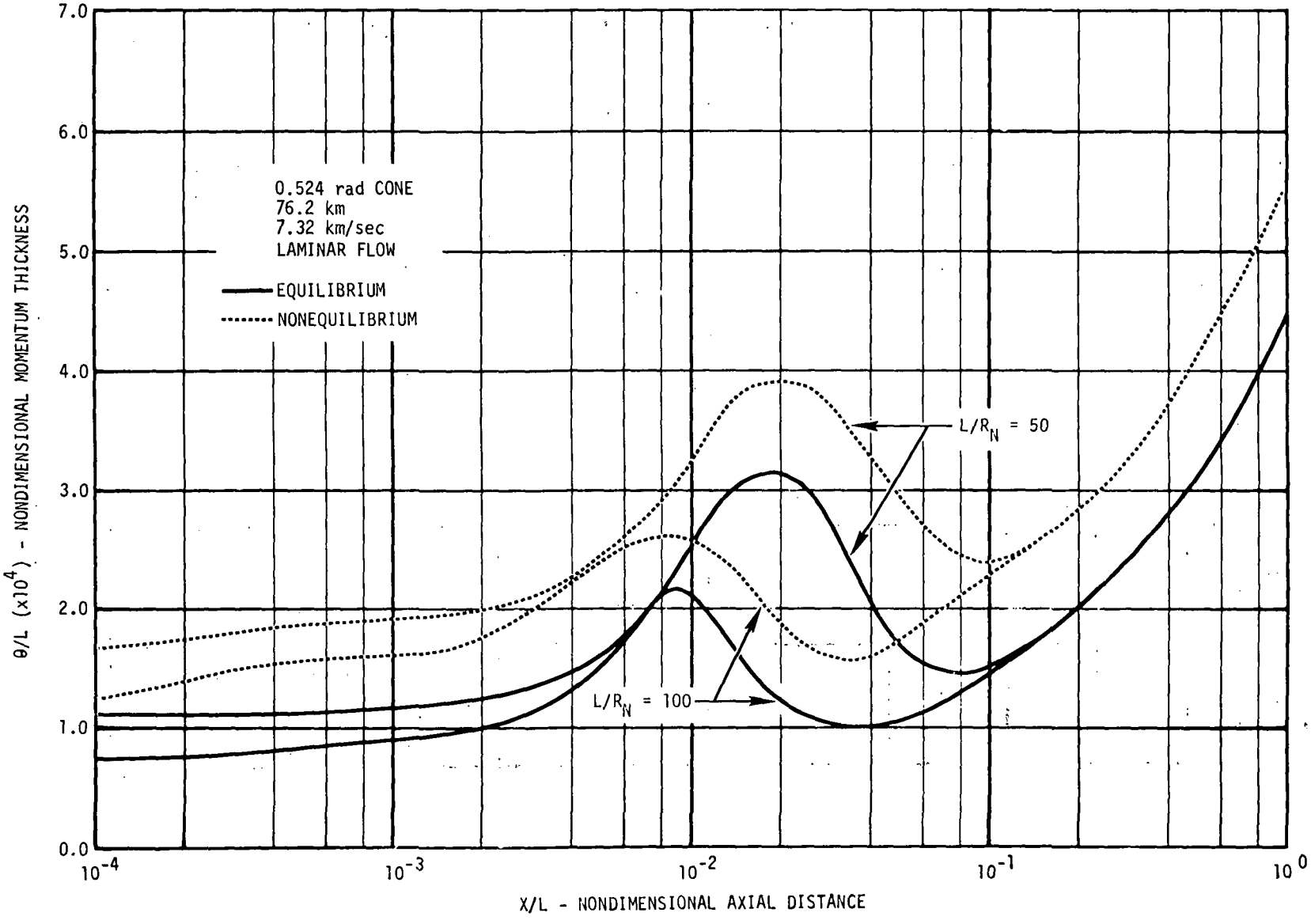

Figure 17. - Laminar Boundary Layer Momentum Thickness at 76.2 km.

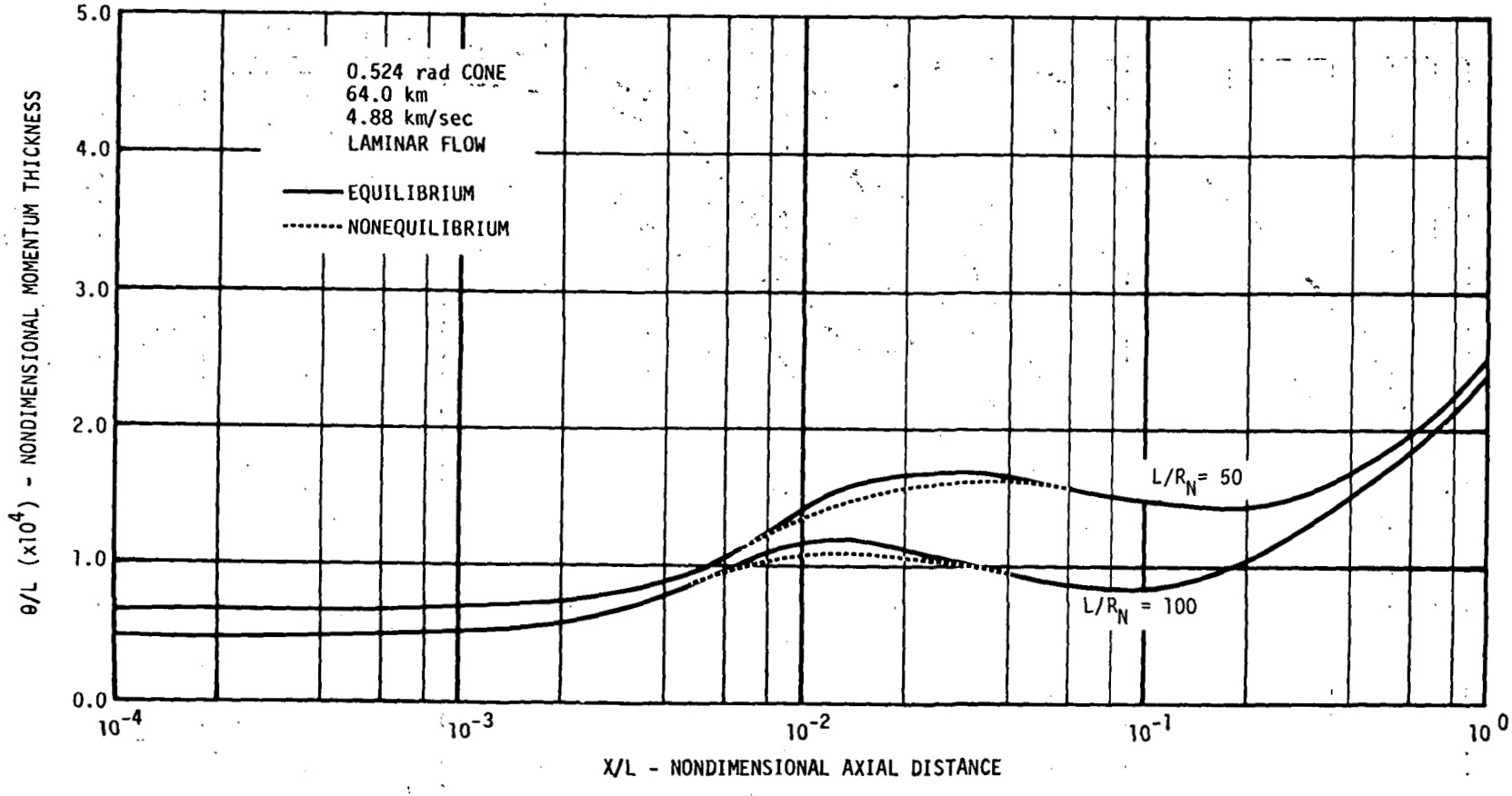

Figure 18. - Laminar Boundary Layer Momentum Thickness at 64.0 km.

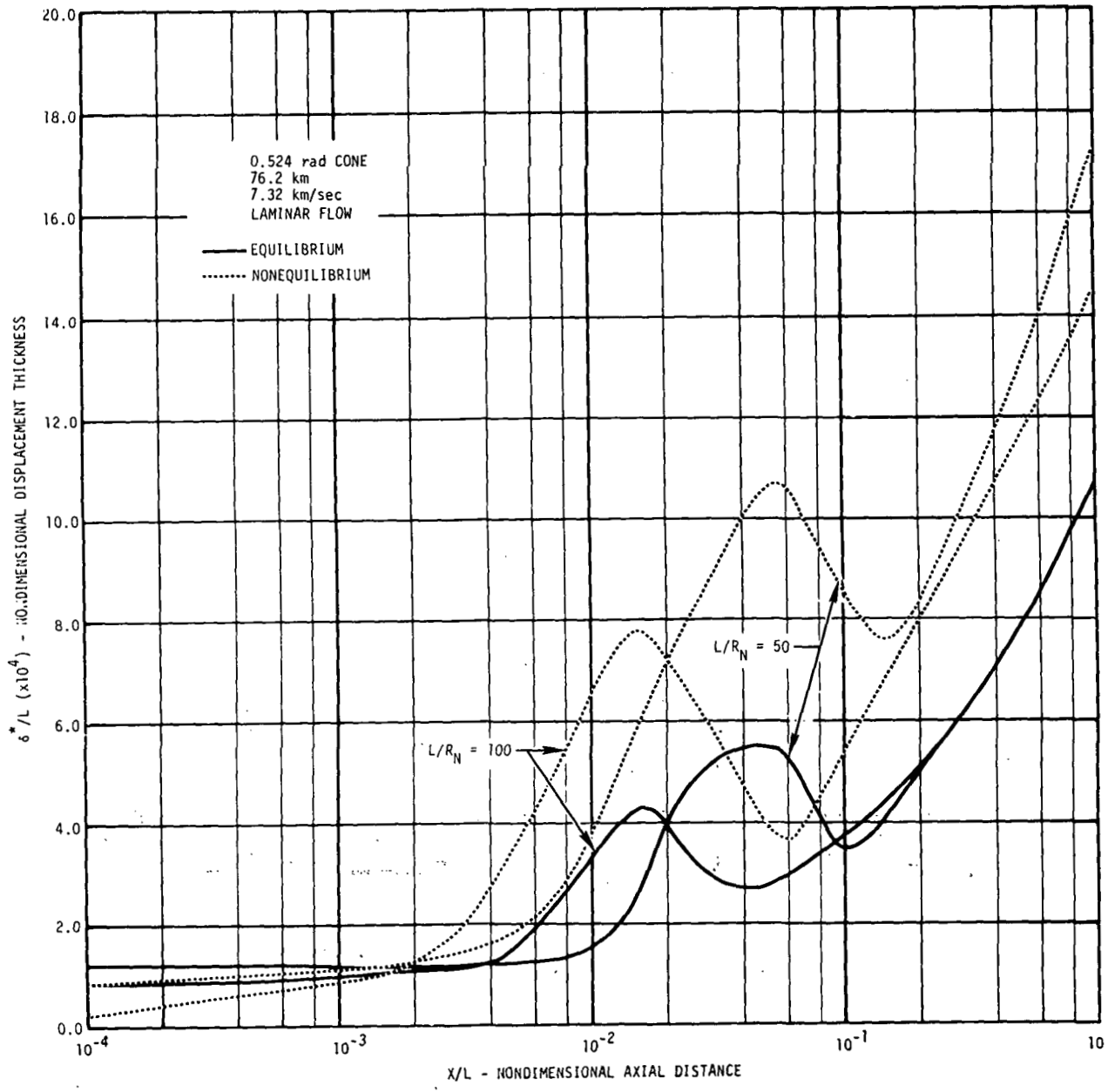

Figure 19. - Laminar Boundary Layer Displacement Thickness at 76.2 km.

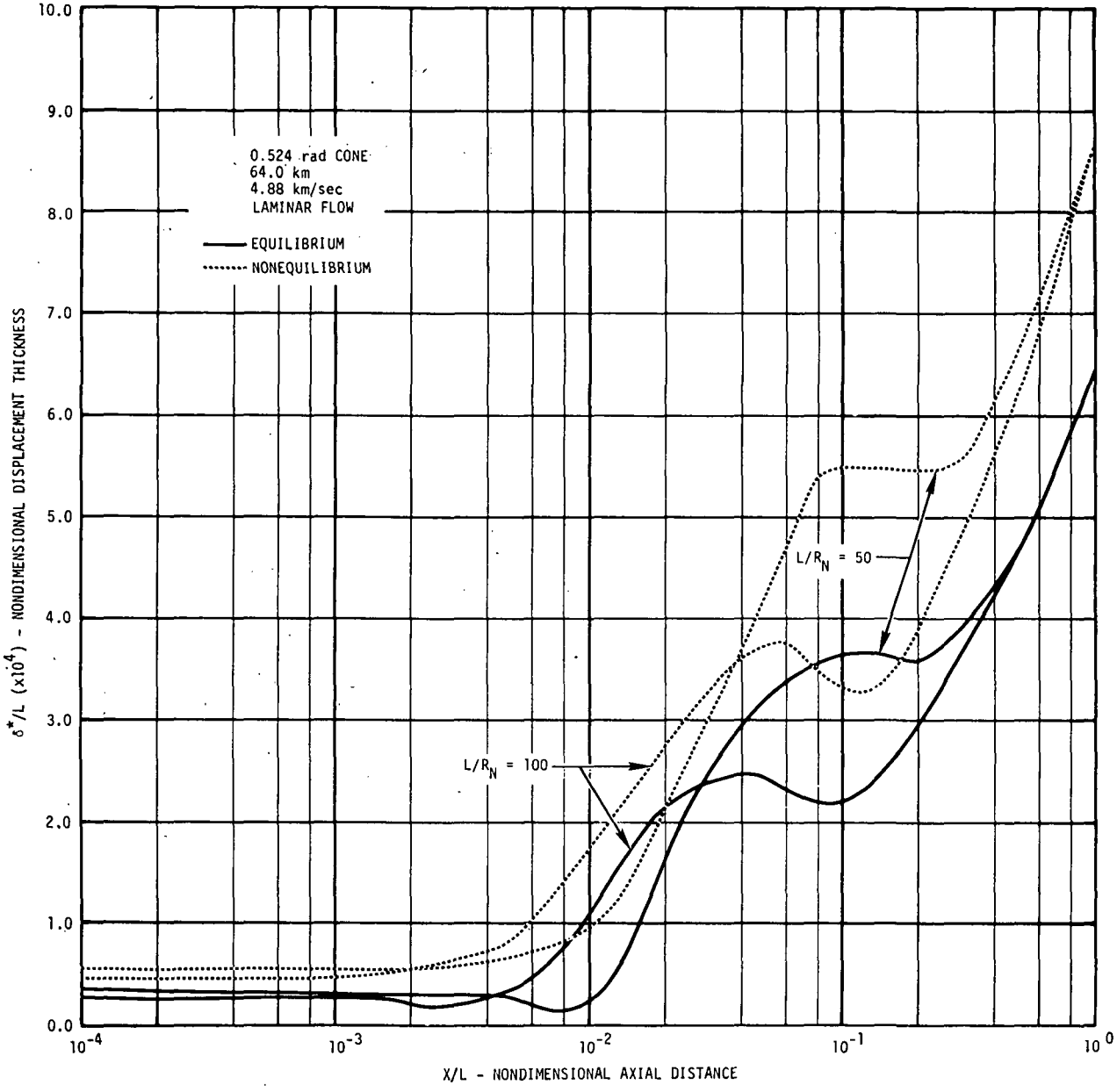

Figure 20. - Laminar Boundary Layer Displacement Thickness at 64.0 km.

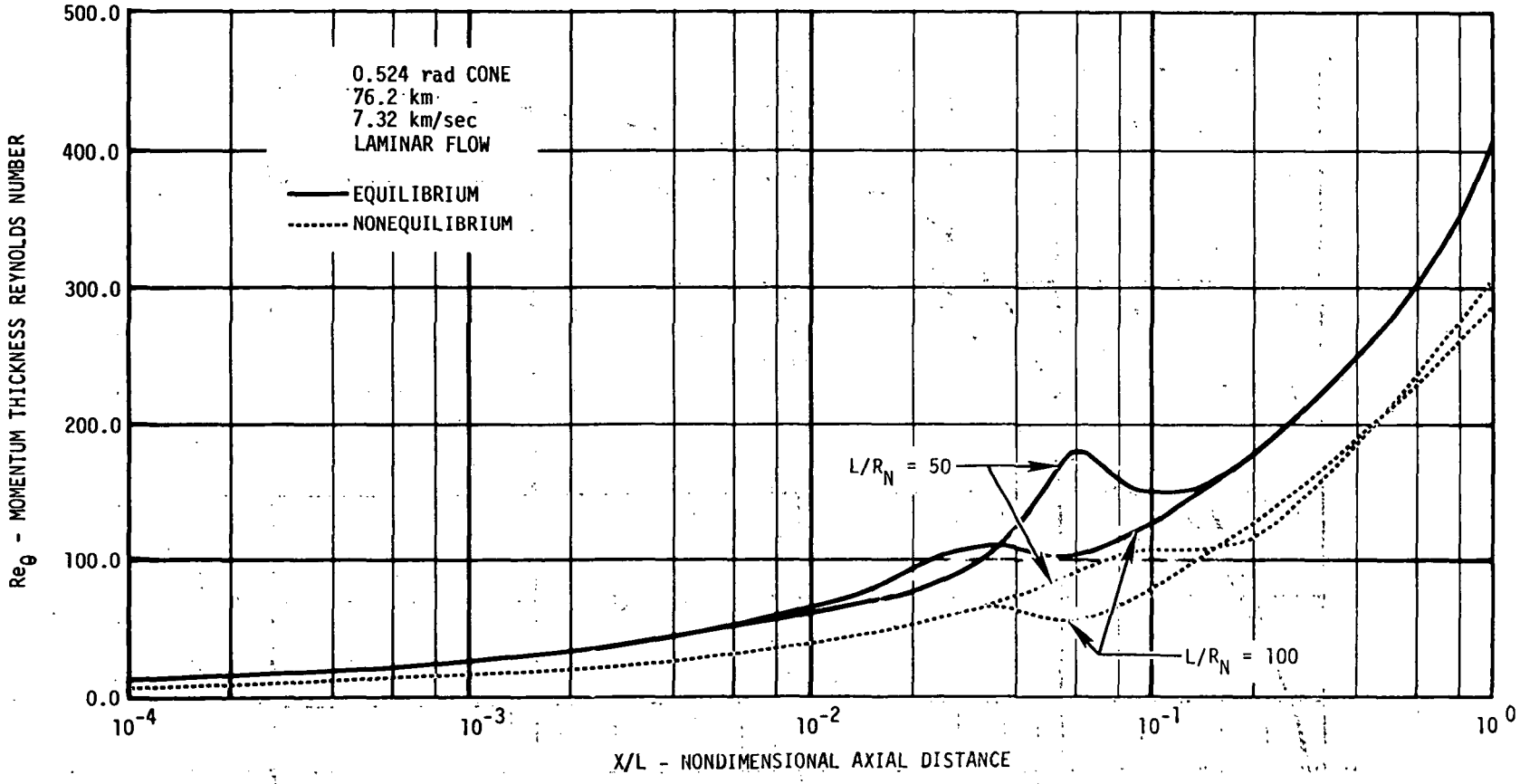

Figure 21. - Laminar Momentum Thickness Reynolds Number at 76.2 km.

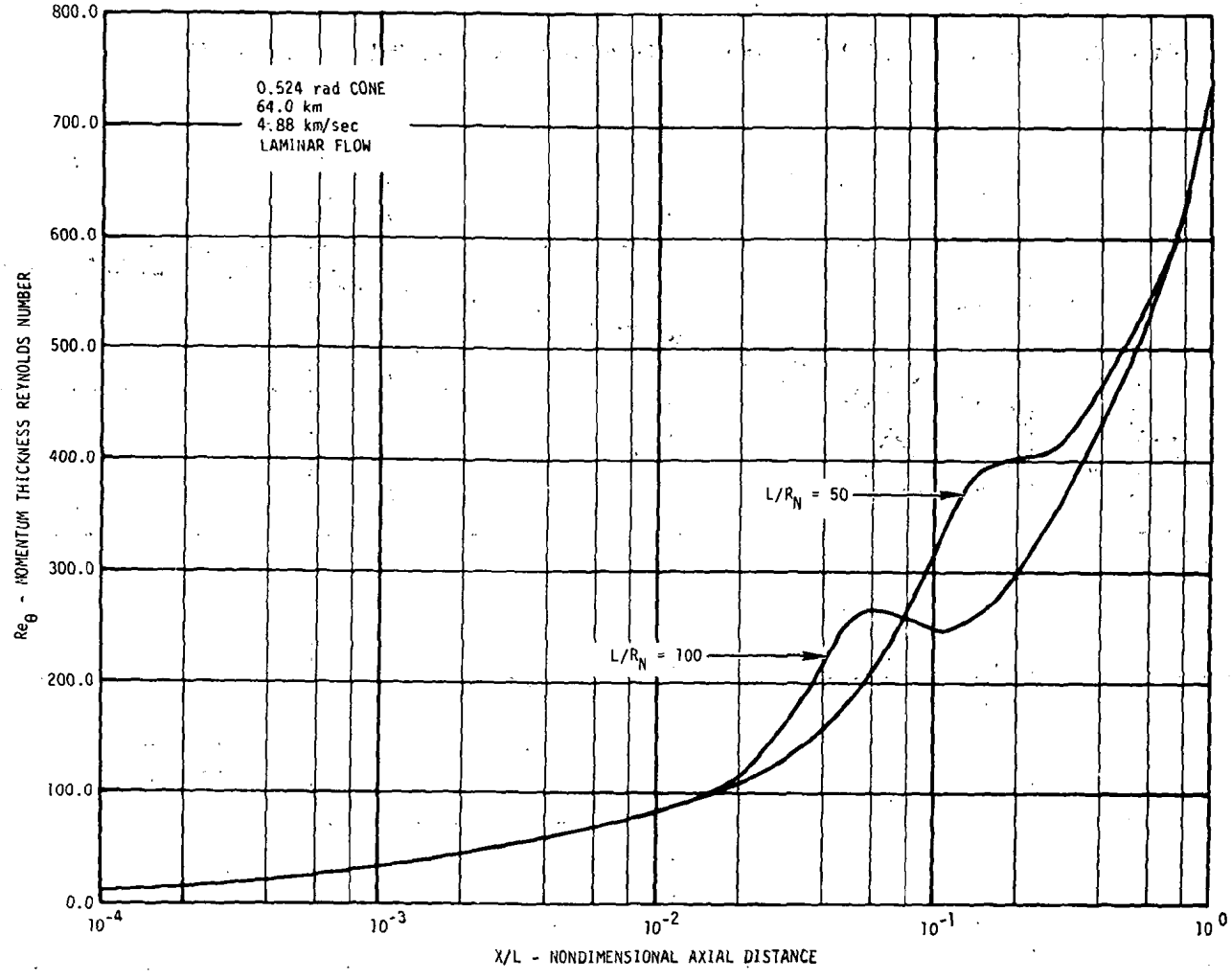

Figure 22. - Laminar Momentum Thickness Reynolds Number at 64.0 km.

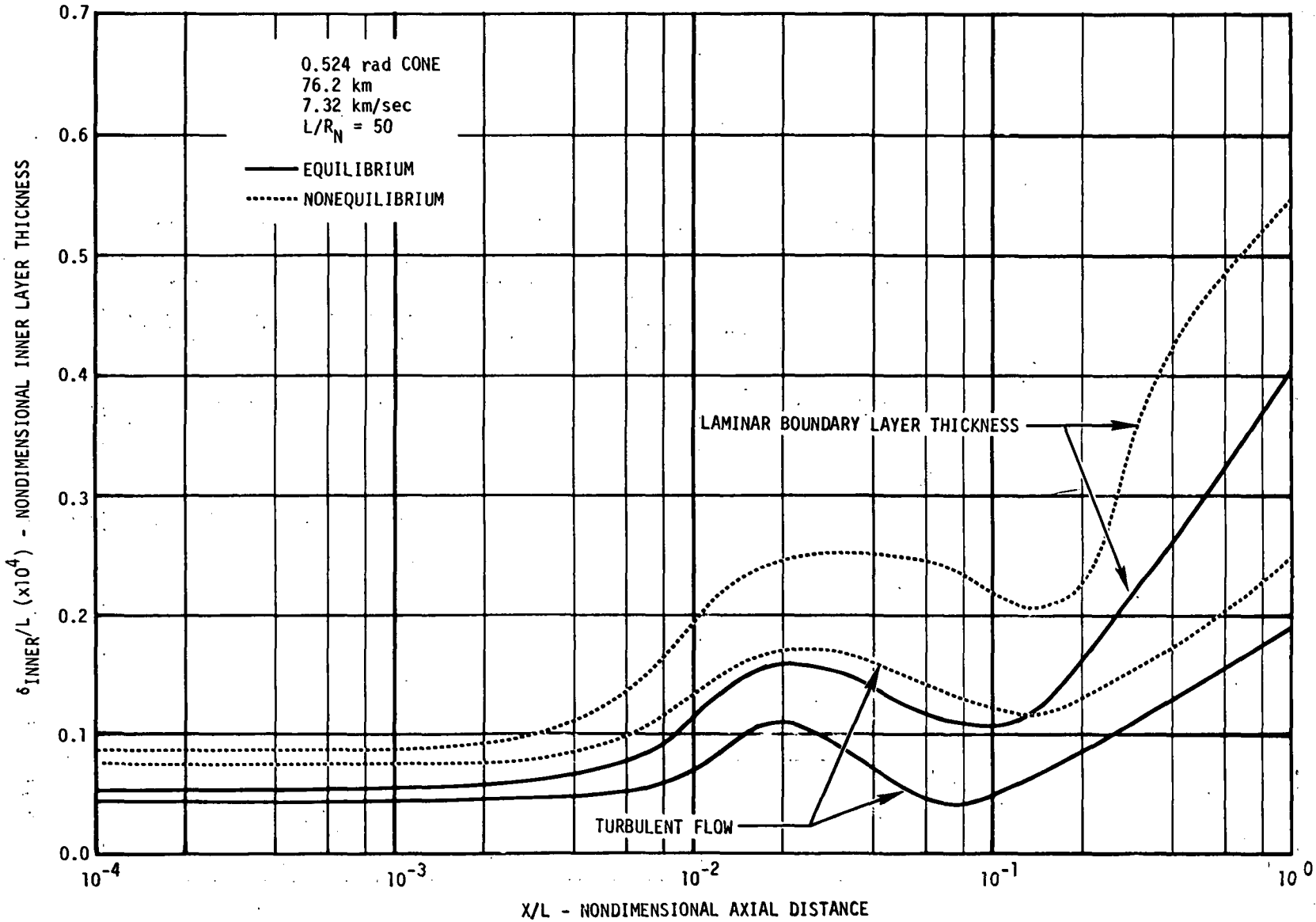

Figure 23. - Boundary Layer Inner Layer Thickness at 76.2 km.

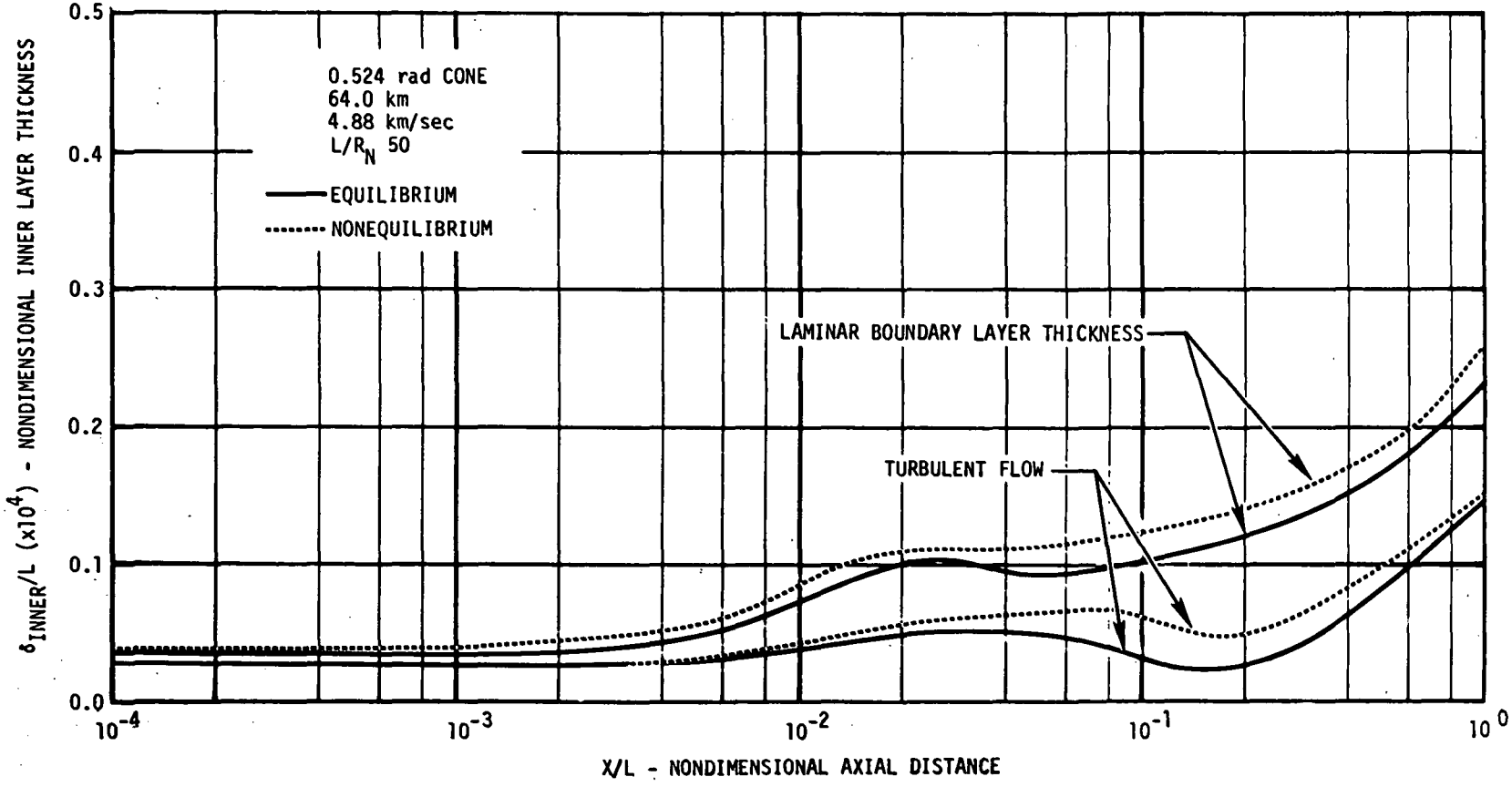

Figure 24. - Boundary Layer Inner Layer Thickness at 64.0 km.

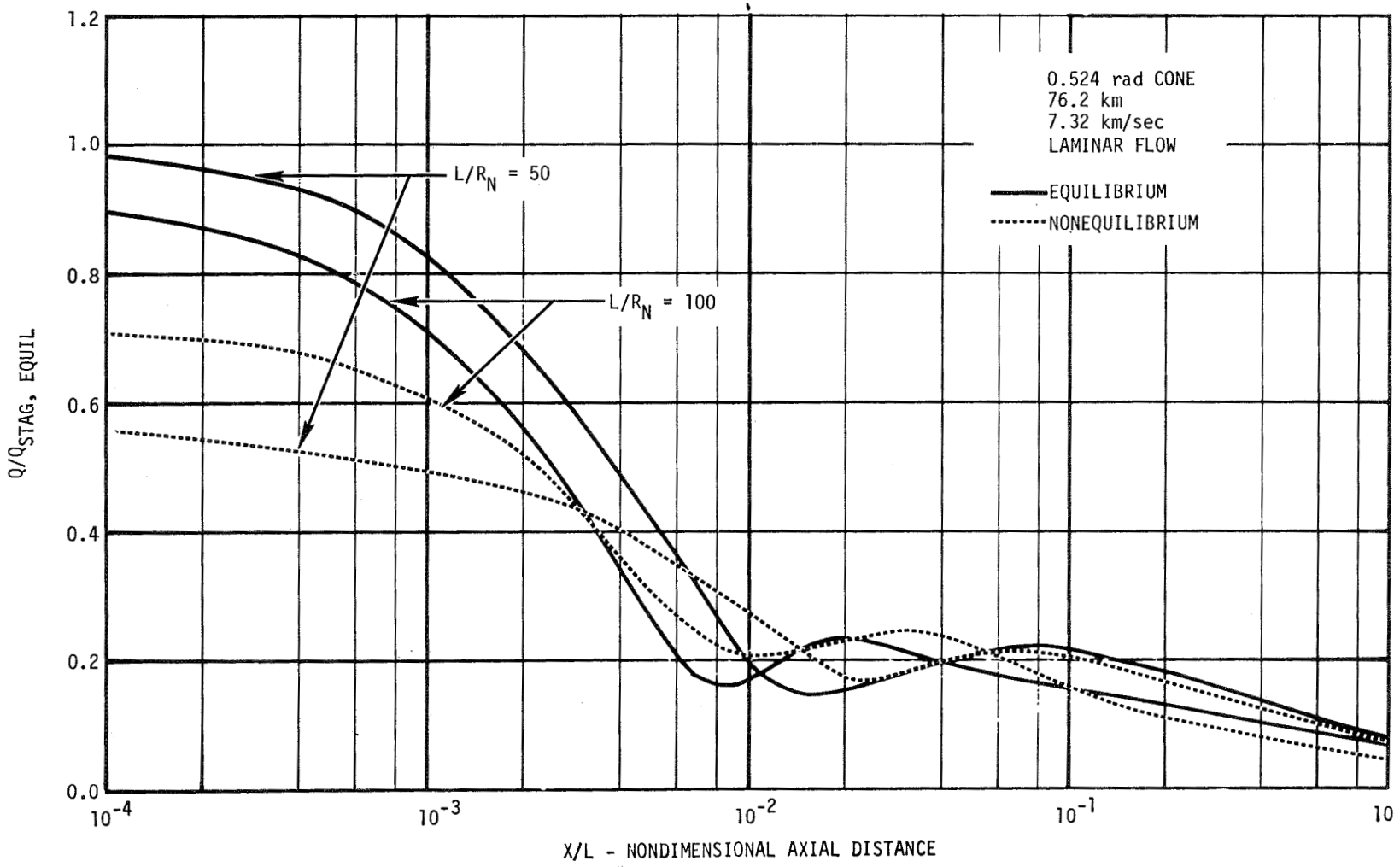

Figure 25. - Laminar Heating Distribution at 76.2 km.

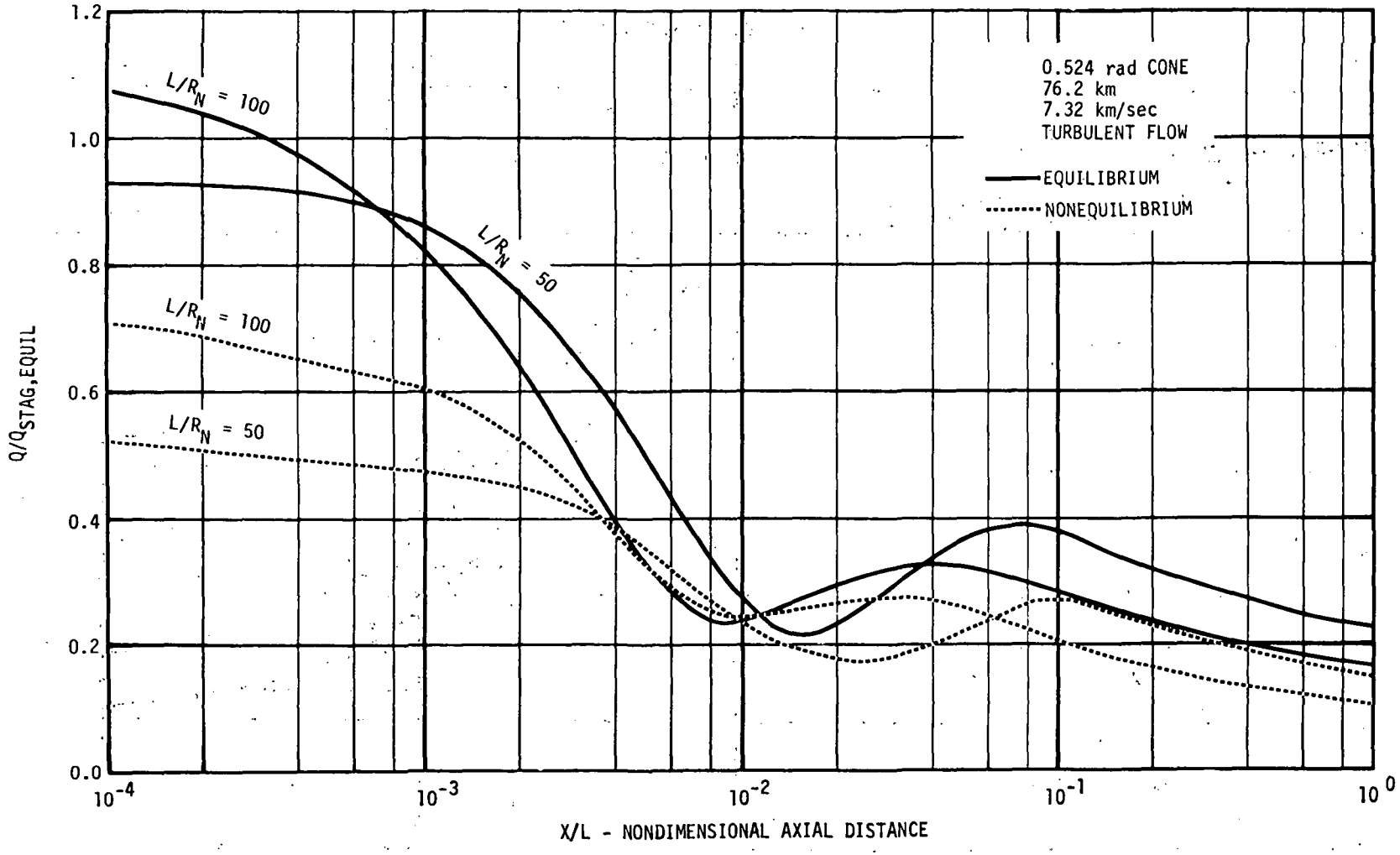

Figure 26. - Turbulent Heating Distribution at 76.2 km.

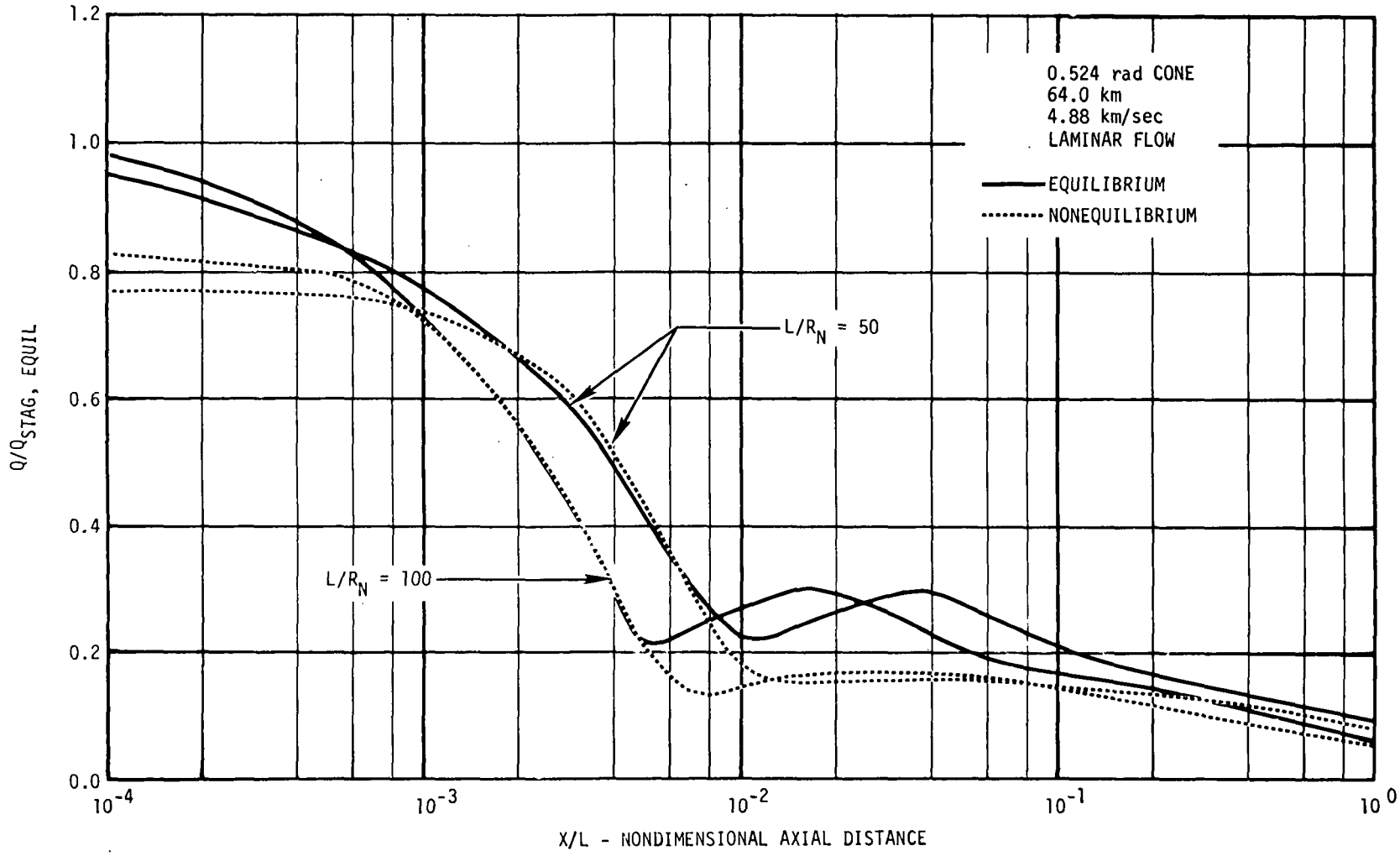

Figure 27. - Laminar Heating Distribution at 64.0 km.

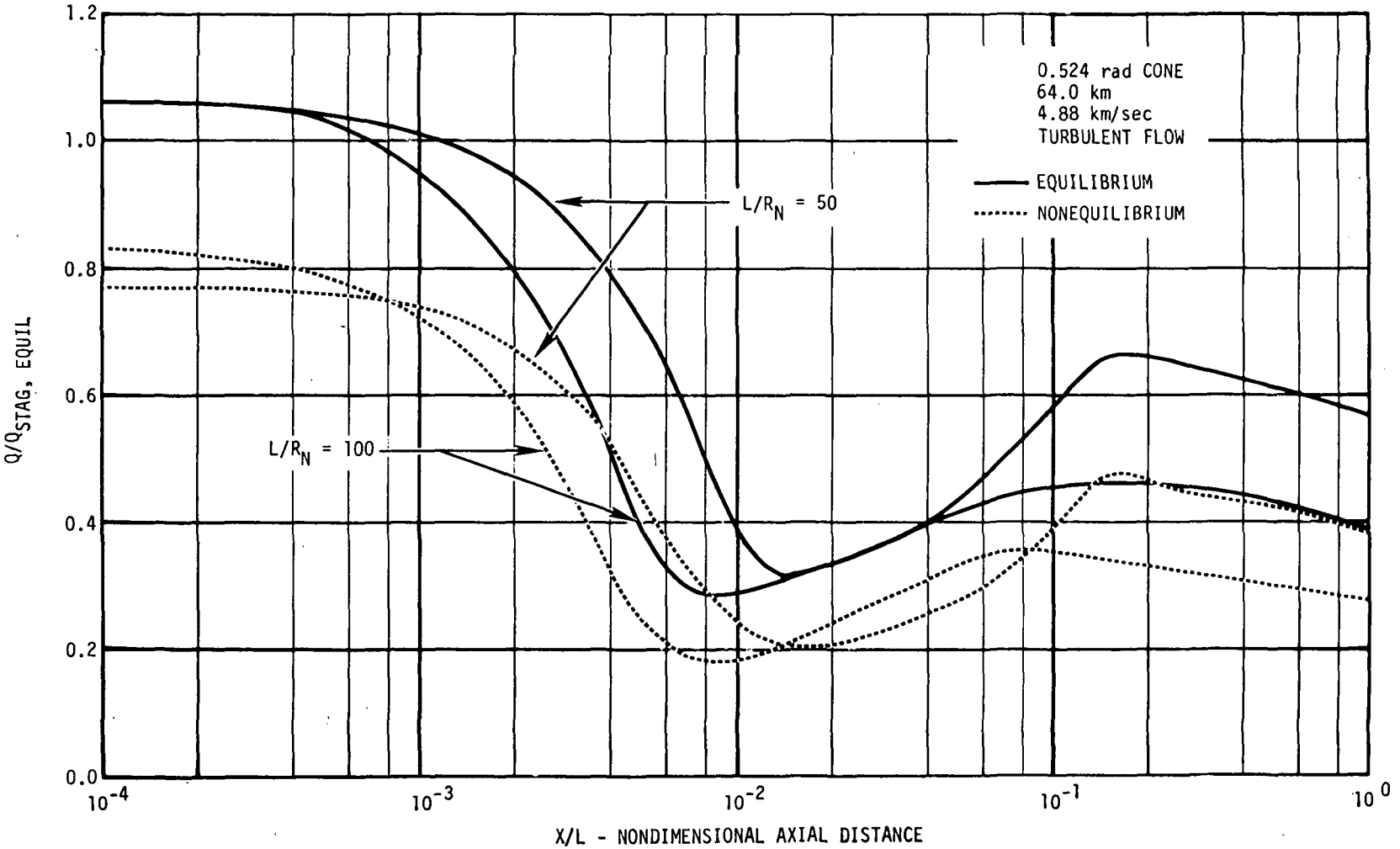

Figure 28. - Turbulent Heating Distribution at 64.0 km.

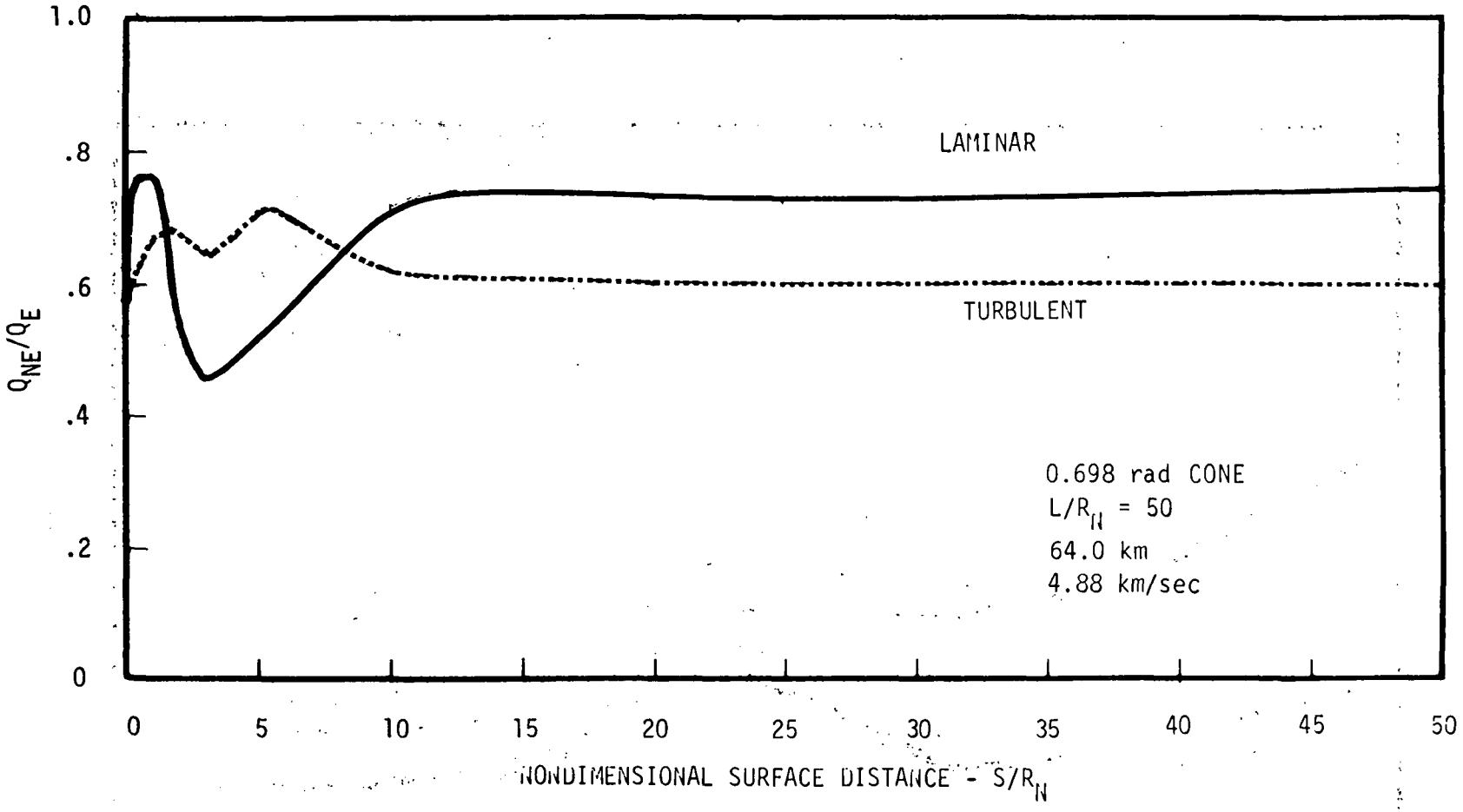

Figure 29. - Heating Reduction Due to Nonequilibrium Chemistry.

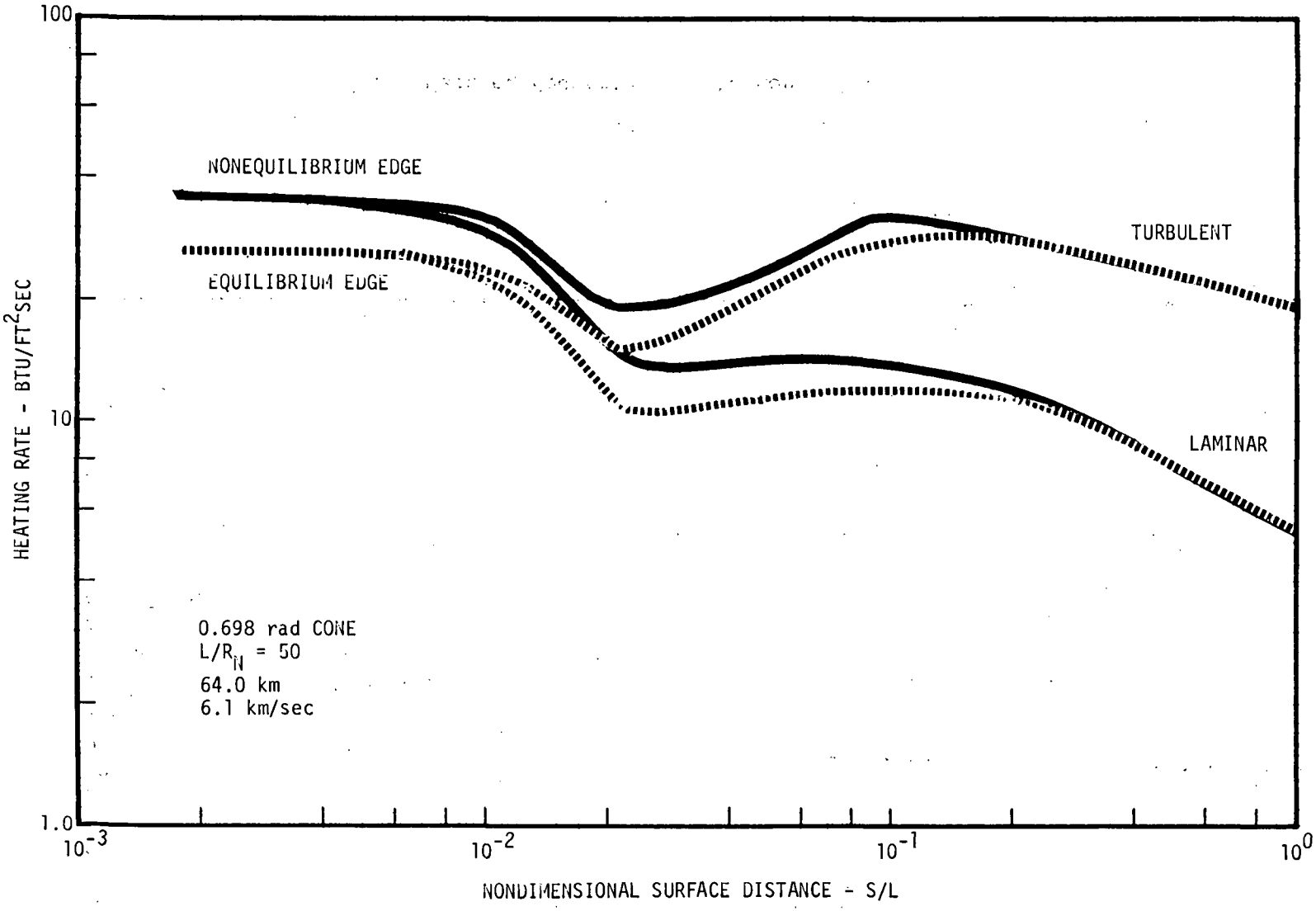

Figure 30. - Effect of Edge Chemistry on Heating Rate.

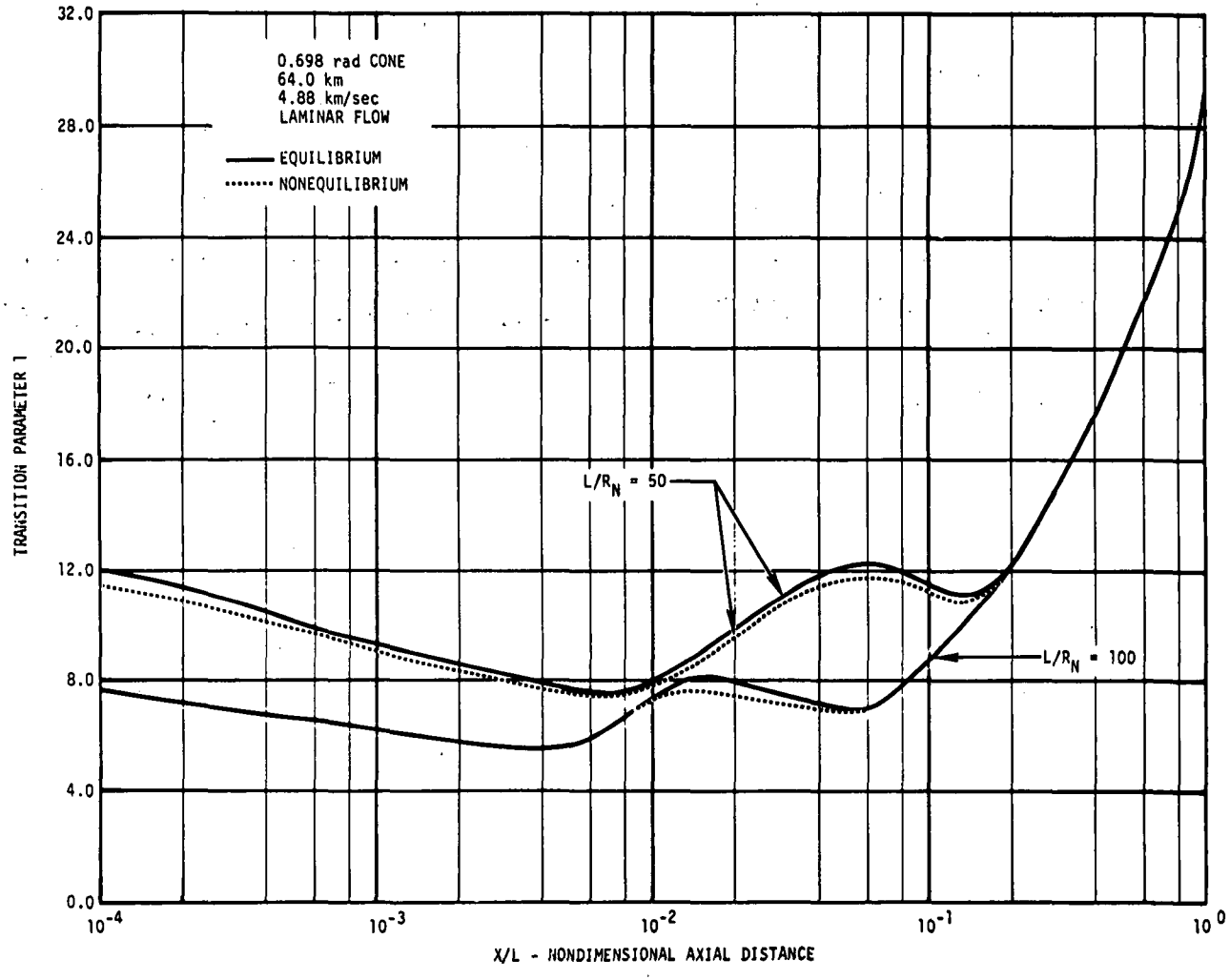

Figure 31. - Effect of Chemical Nonequilibrium on Transition Parameter 1.

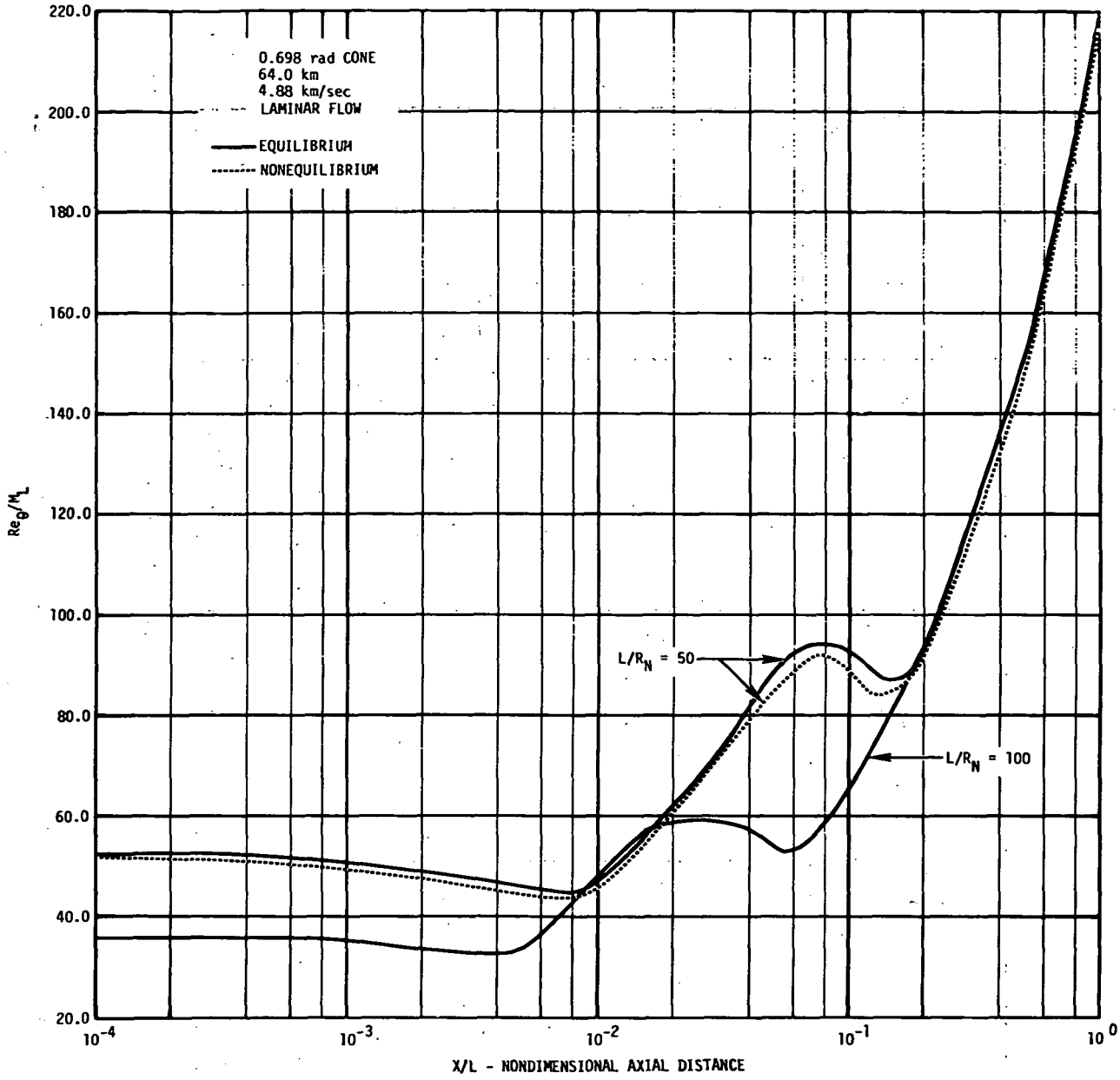

Figure 32. – Effect of Chemical Nonequilibrium on $R_{e\theta}/M_L$.

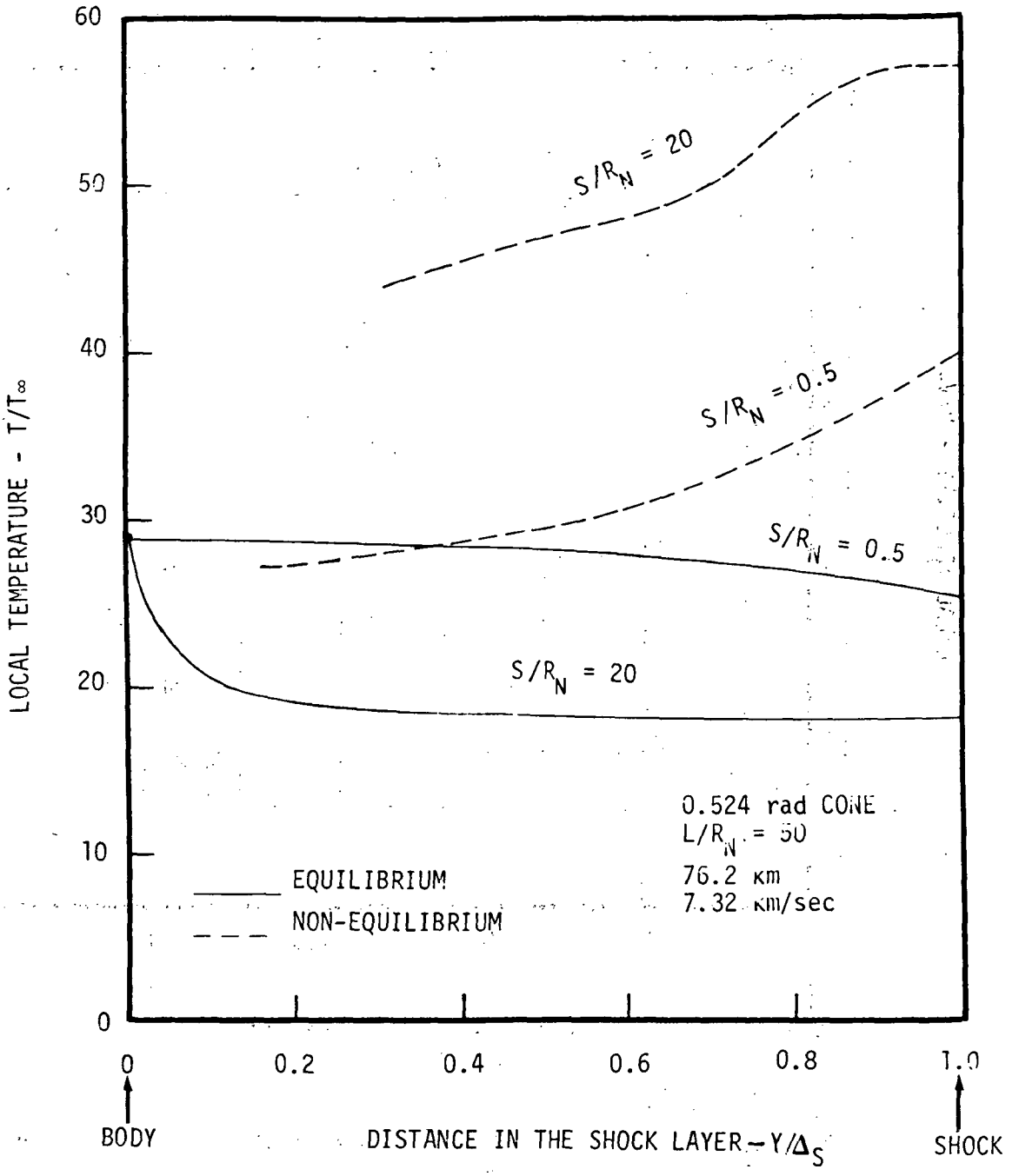

Figure 33. - Effect of Chemical Nonequilibrium on Shock Layer Temperature Distribution.

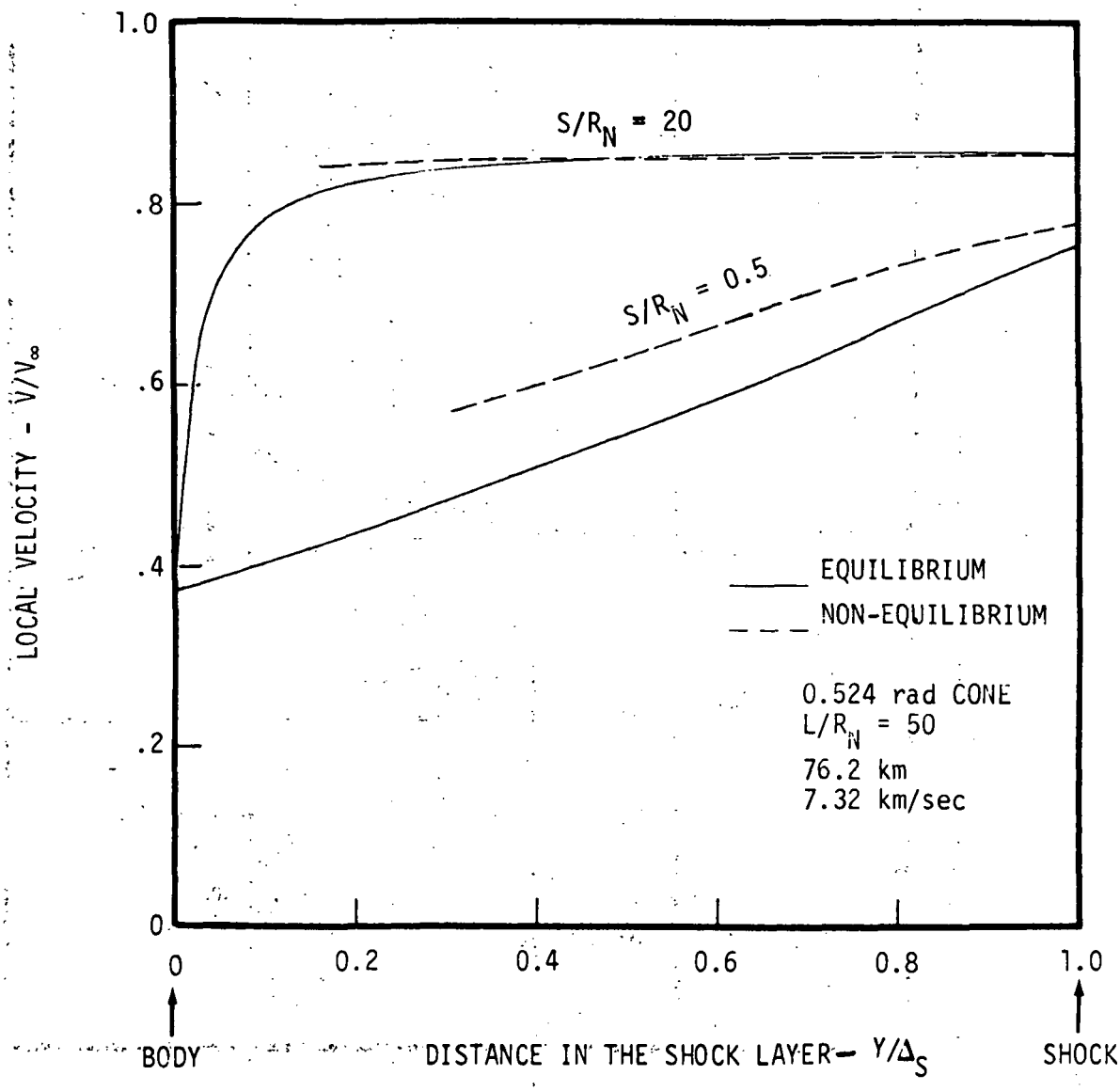

Figure 34. - Effect on Chemical Nonequilibrium on Shock Layer Velocity Distribution.

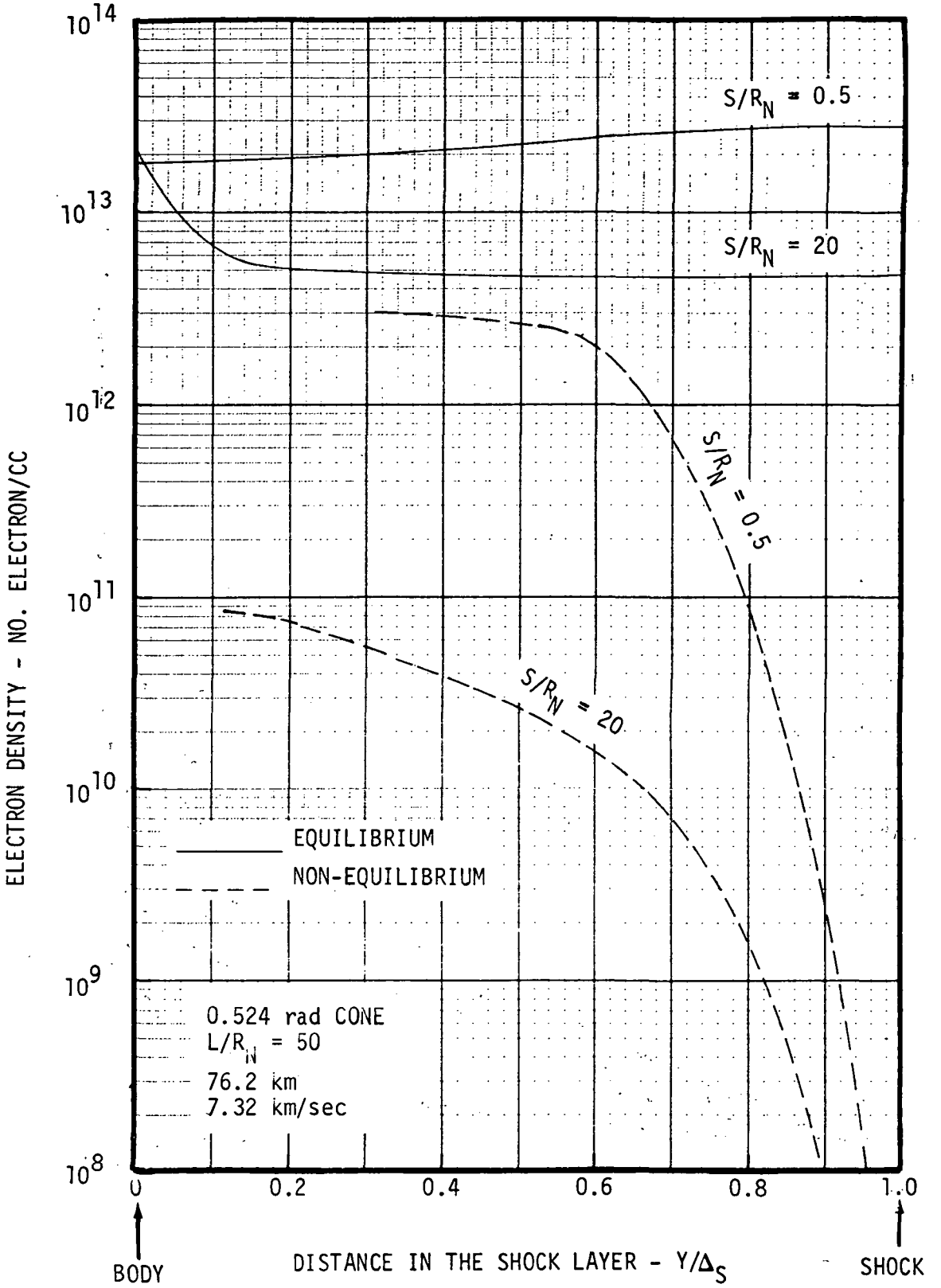

Figure 35. - Effect of Chemical Nonequilibrium on Shock Layer Electron Density Distribution.

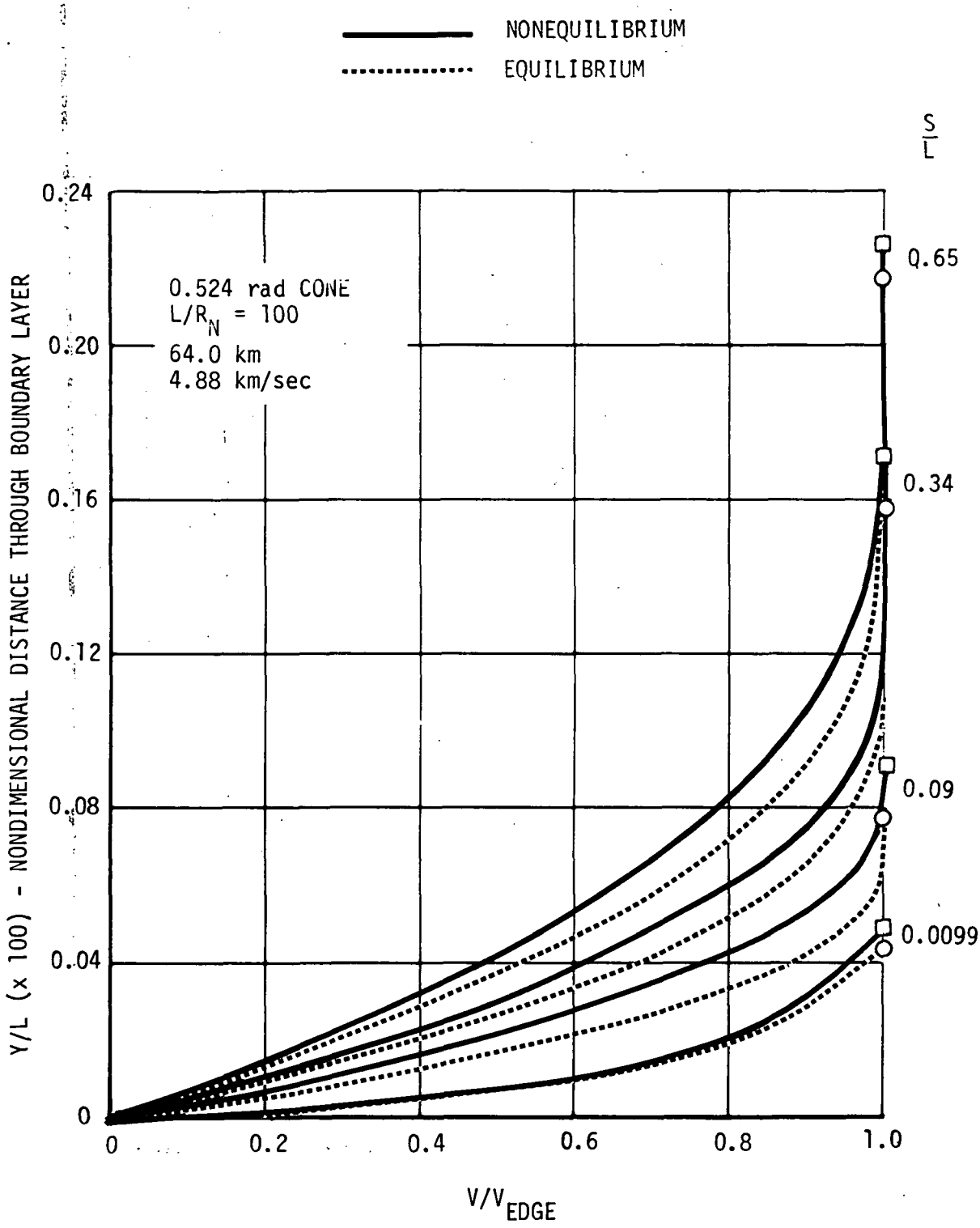

Figure 36. - Laminar Boundary Layer Velocity Profiles at 64.0 km.

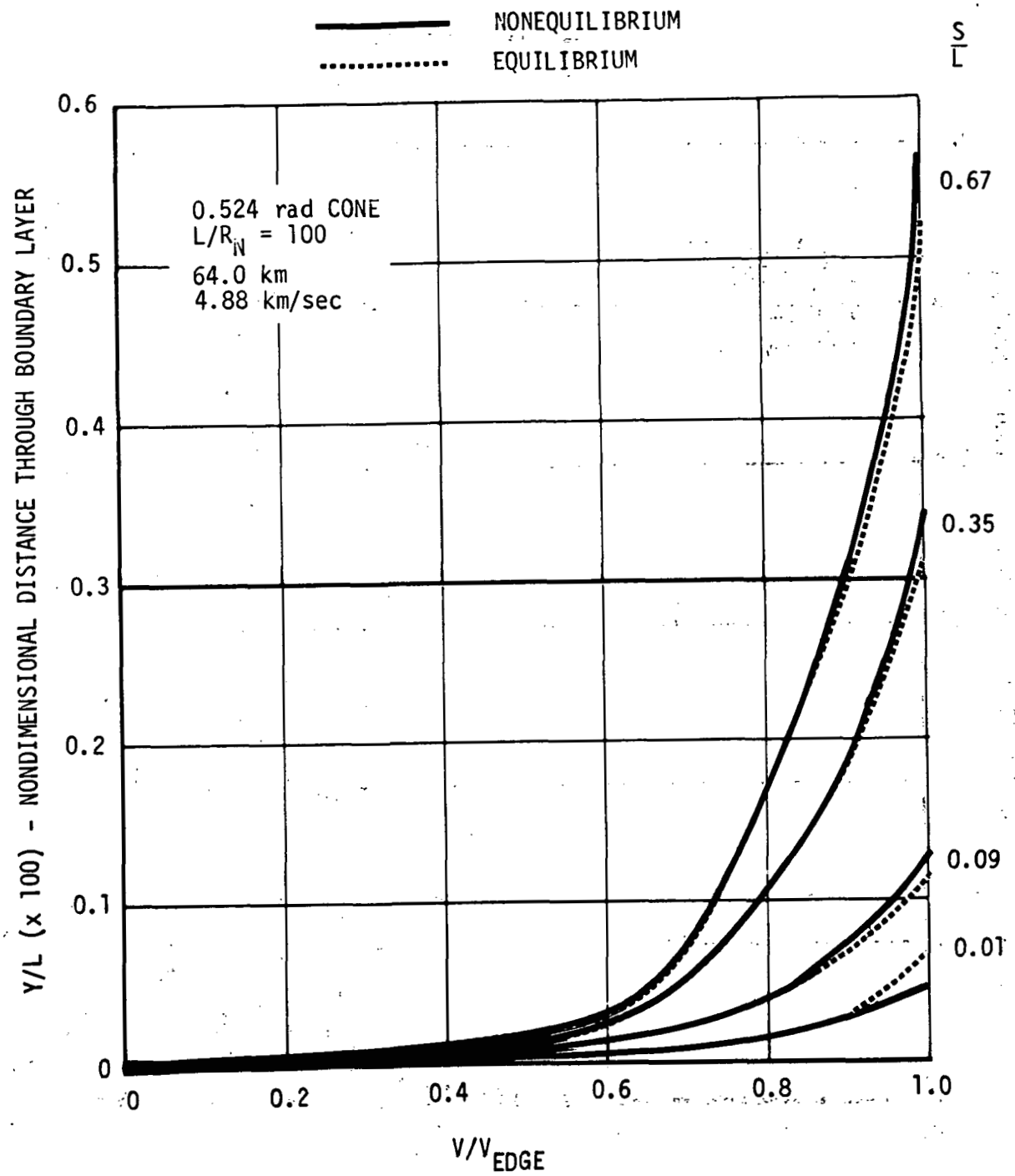

Figure 37. - Turbulent Boundary Layer Velocity Profiles at 64.0 km.

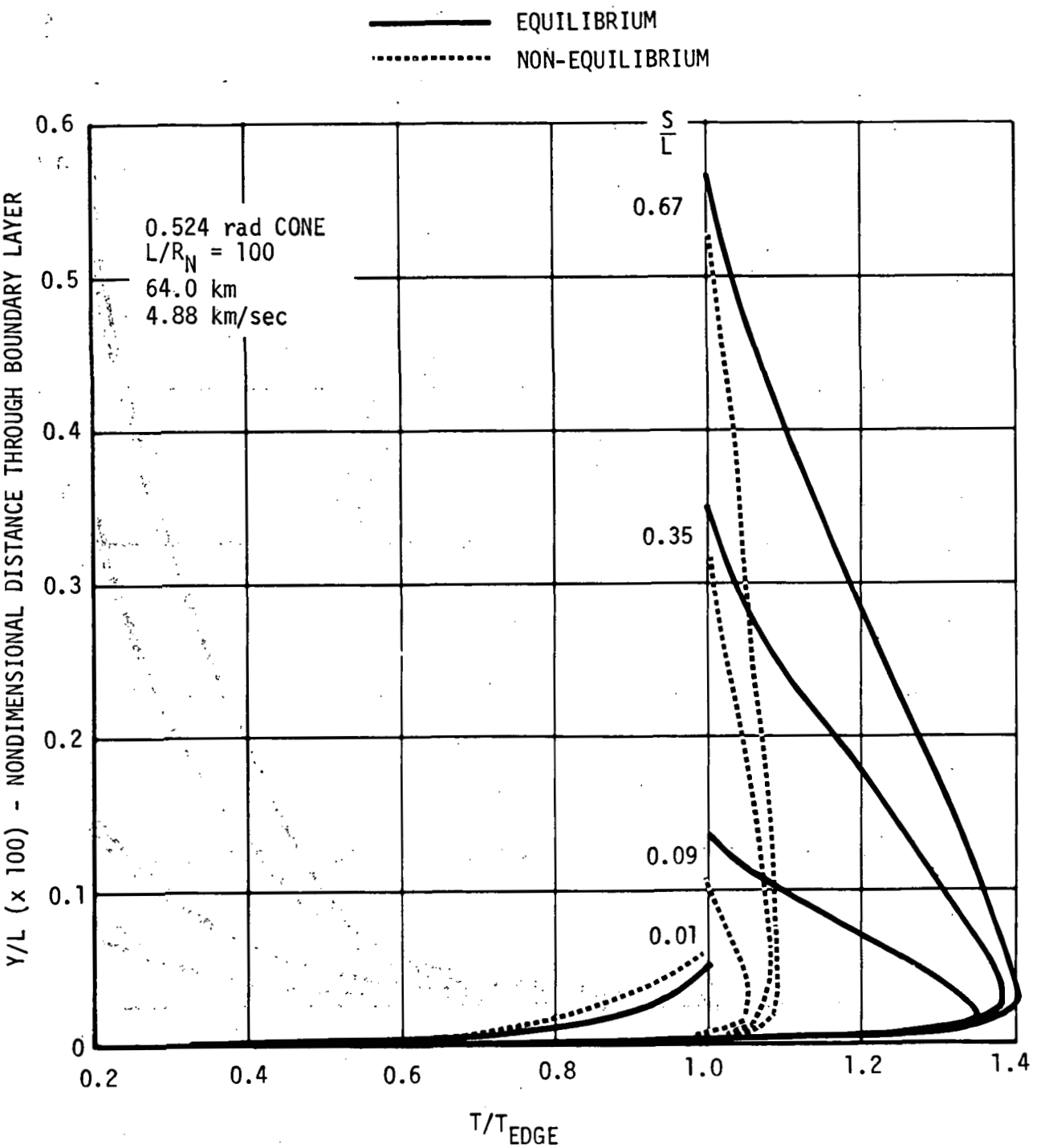

Figure 38. - Turbulent Boundary Layer Temperature Profiles at 64.0 km.

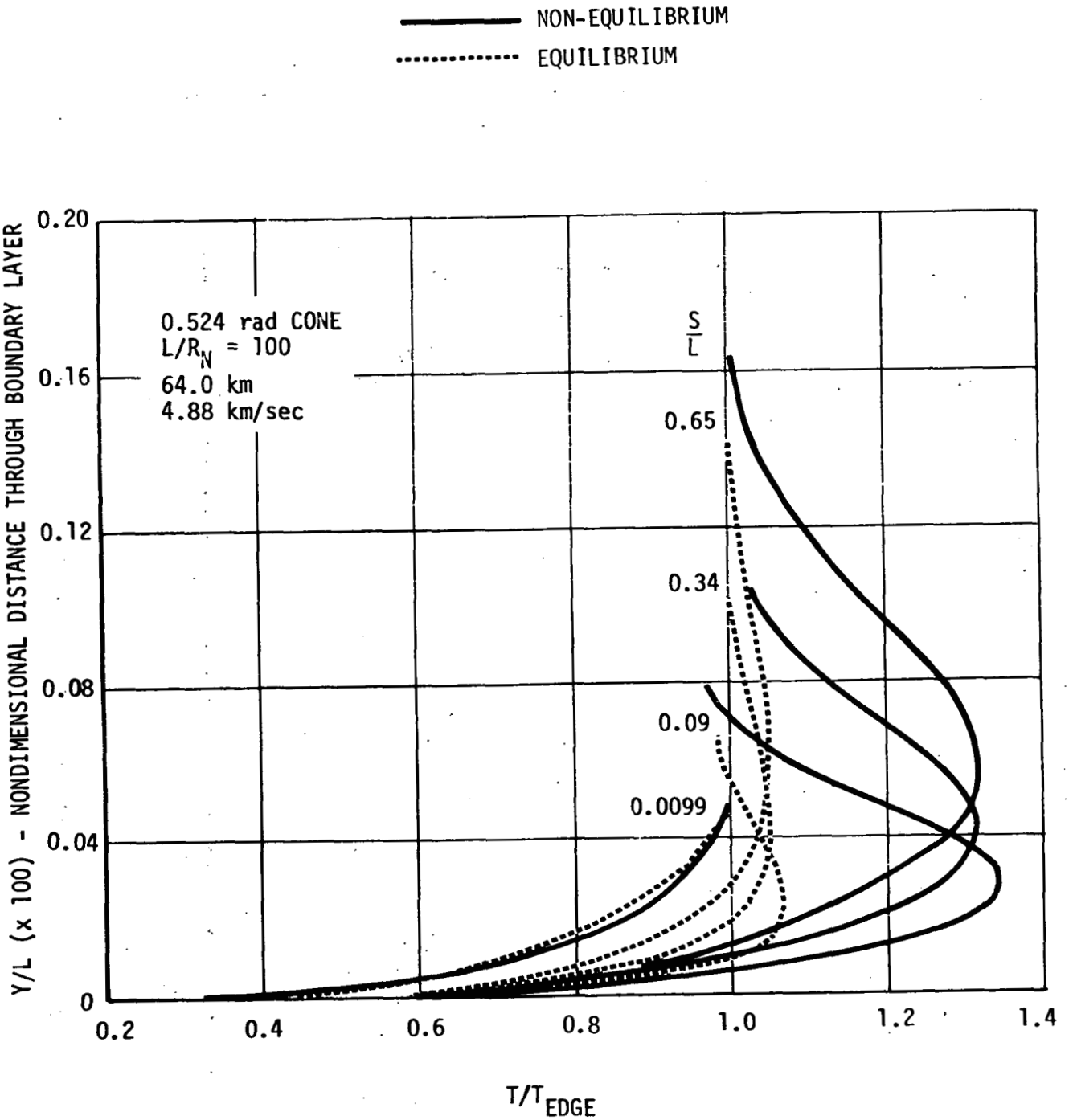

Figure 39. - Laminar Boundary Layer Temperature Profiles at 64.0 km.

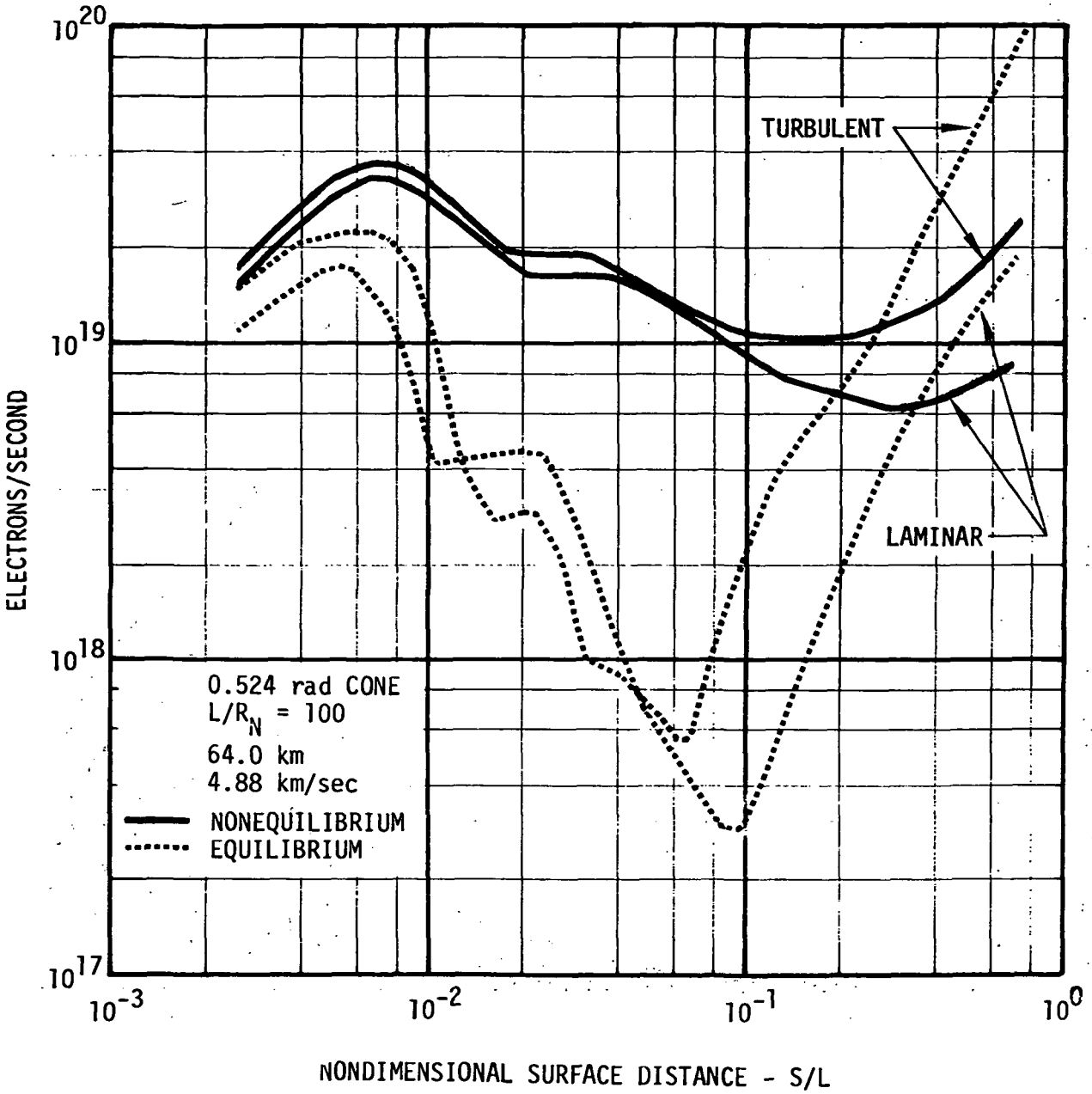

Figure 40. - Effect of Chemical Nonequilibrium on Free Electrons in the Boundary Layer.

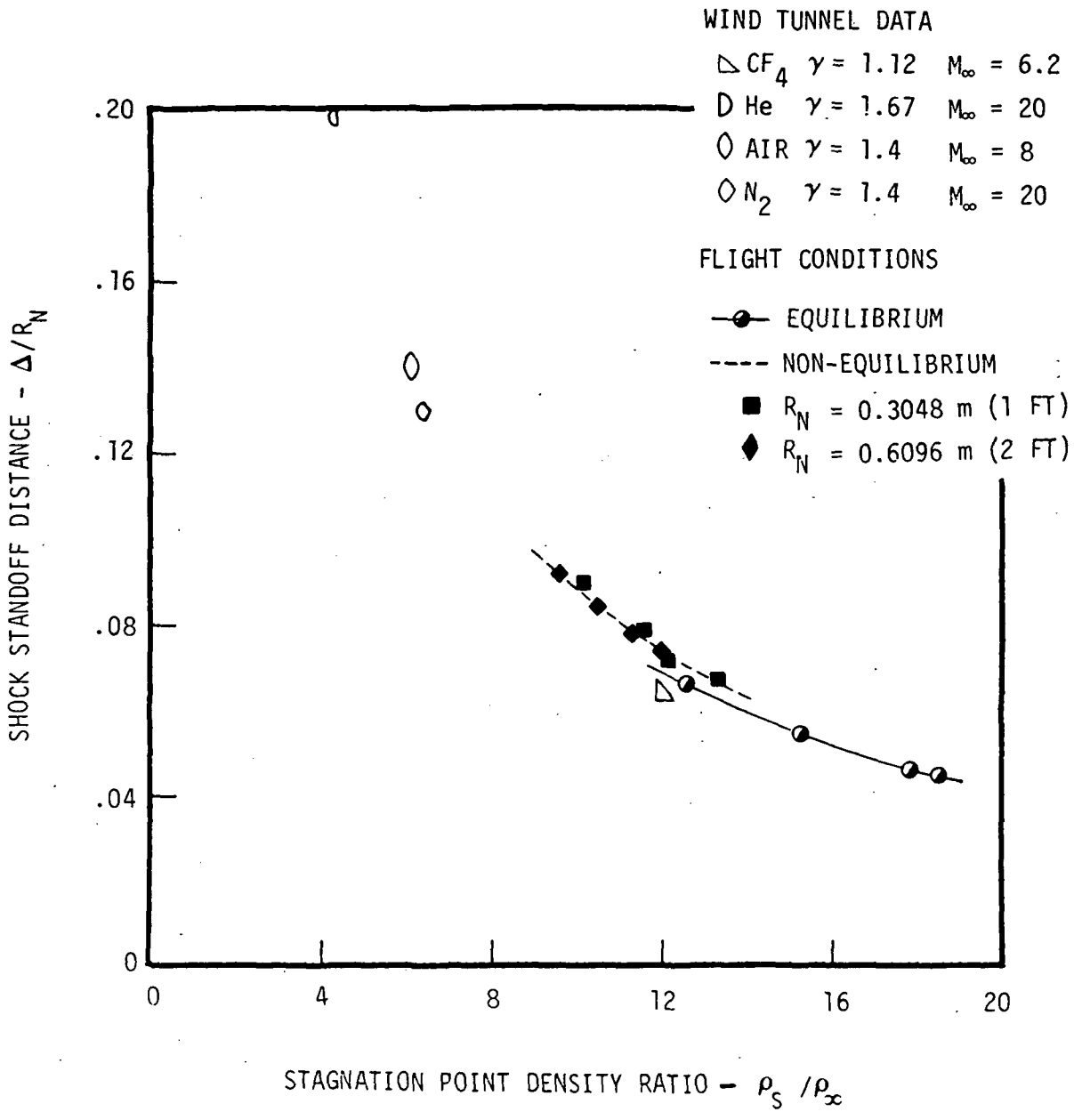

Figure 41. - Comparison of Tunnel and Flight Shock Standoff Distance.

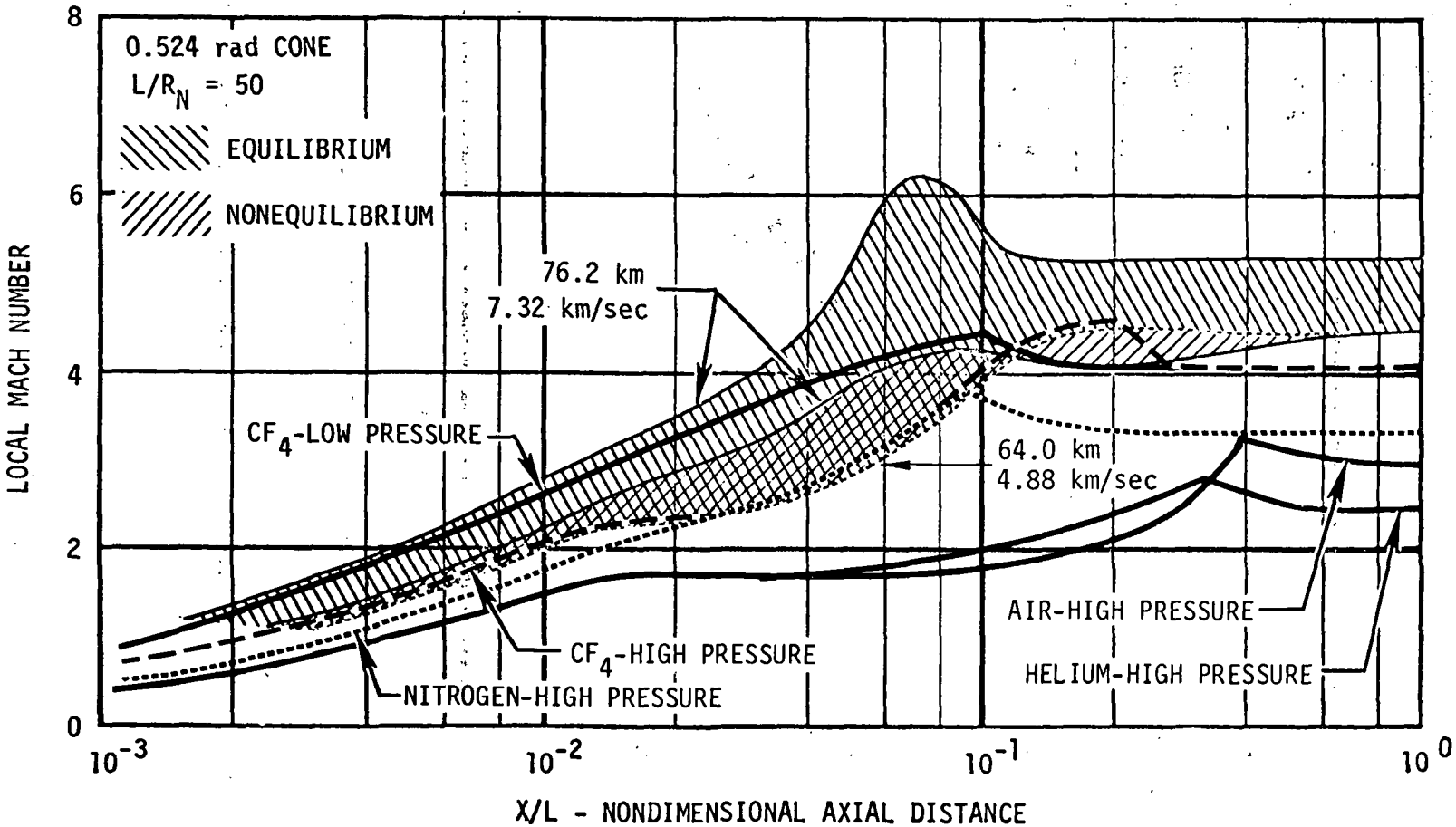

Figure 42. - Tunnel Simulation of Flight Boundary Layer Edge Mach Number for 0.524 rad Cones.

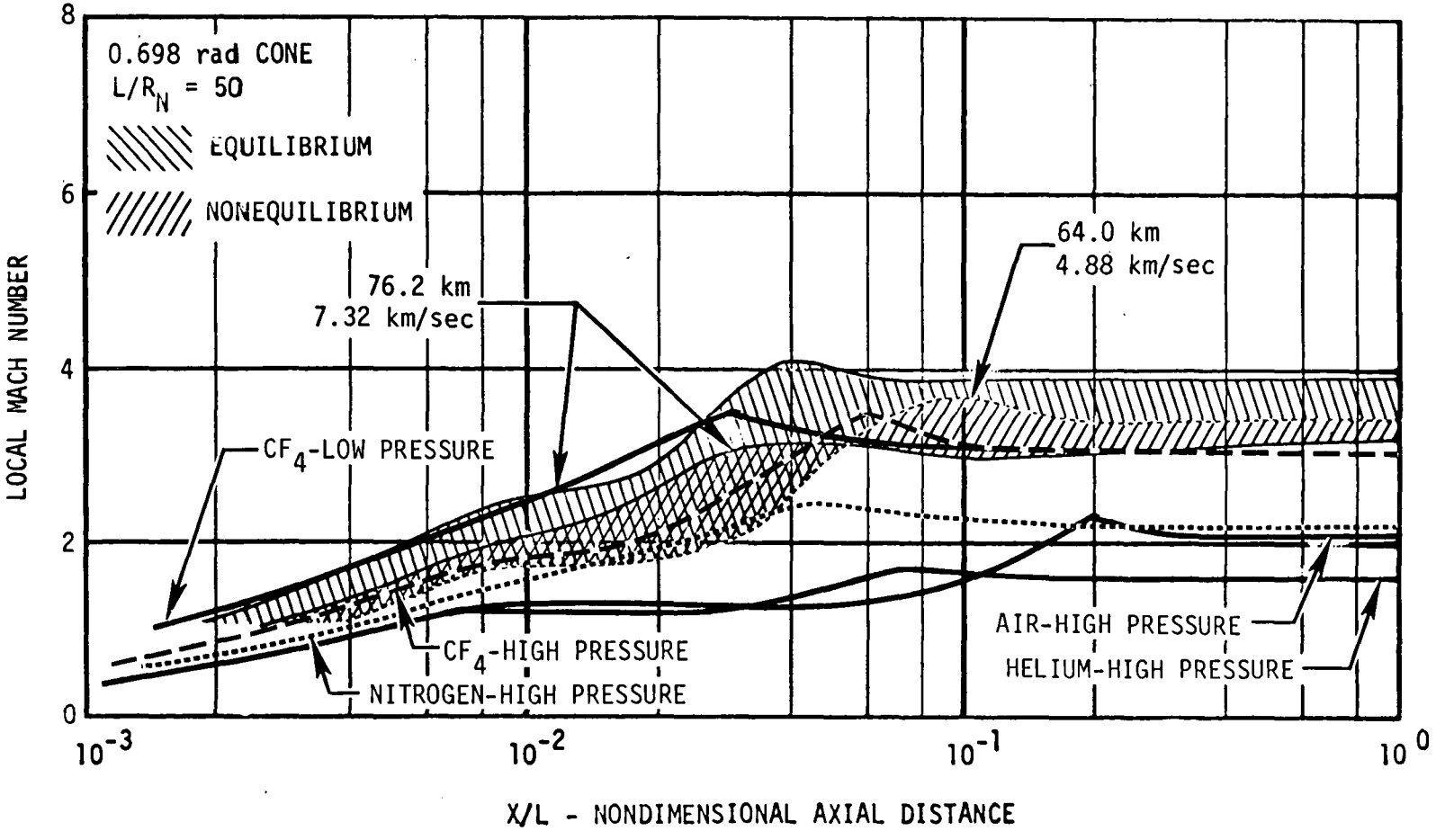

Figure 43. - Tunnel Simulation of Flight Boundary Layer Edge Mach Number for 0.698 rad Cones.

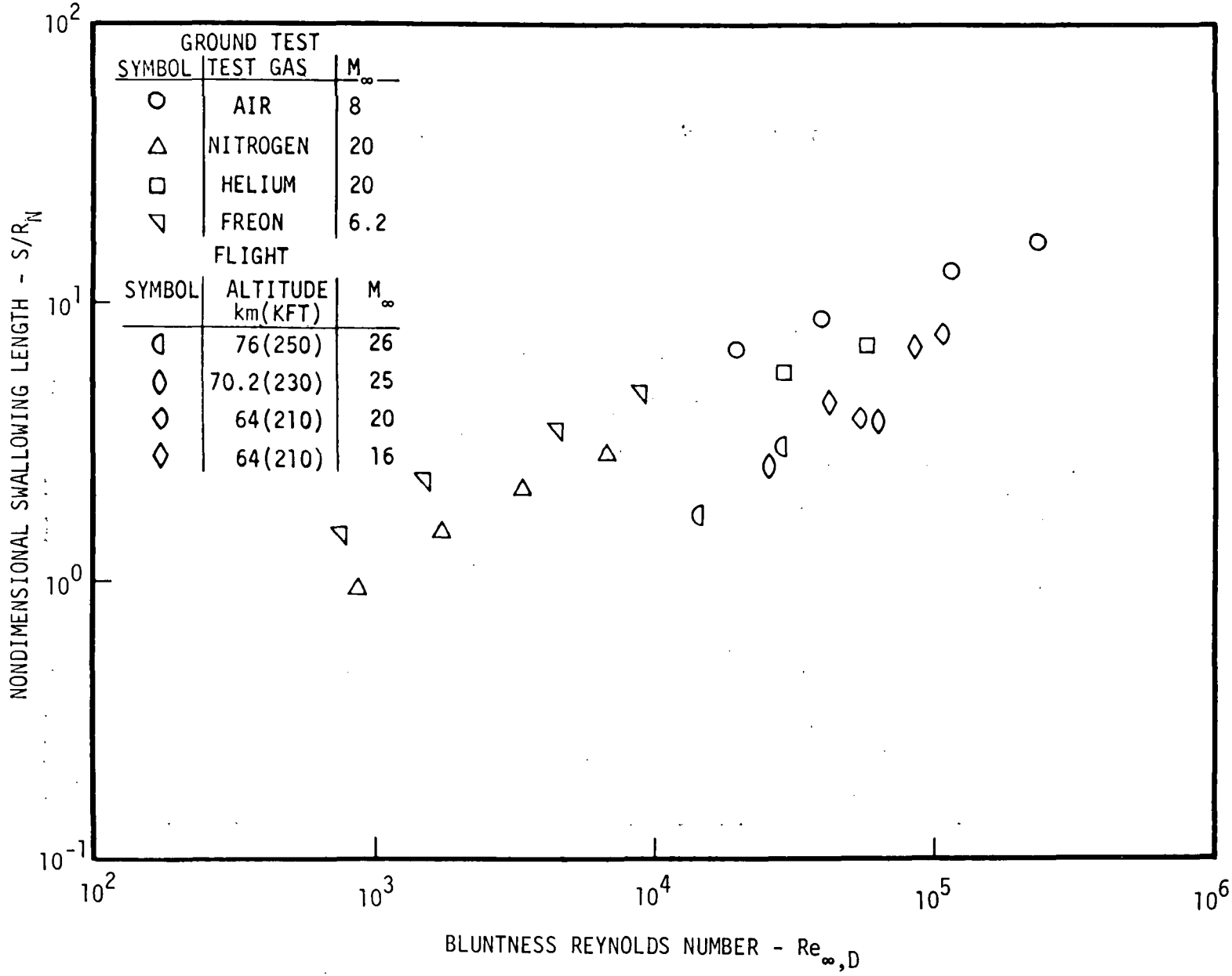

Figure 44. - End of High Entropy Inviscid Flow Region for Laminar 0.524 rad Cones.

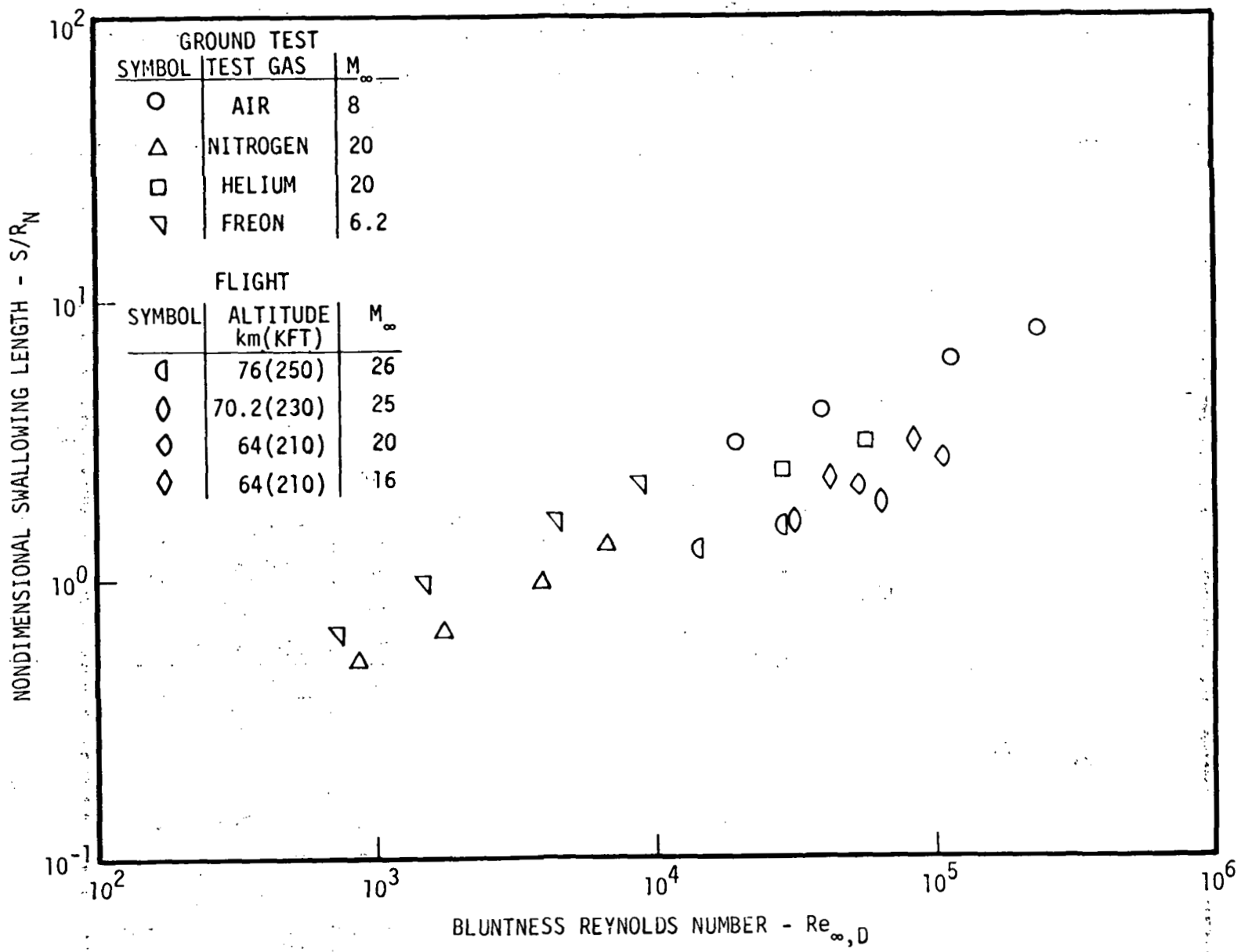

Figure 45. - End of High Entropy Inviscid Flow Region for Laminar 0.698 rad Cones.

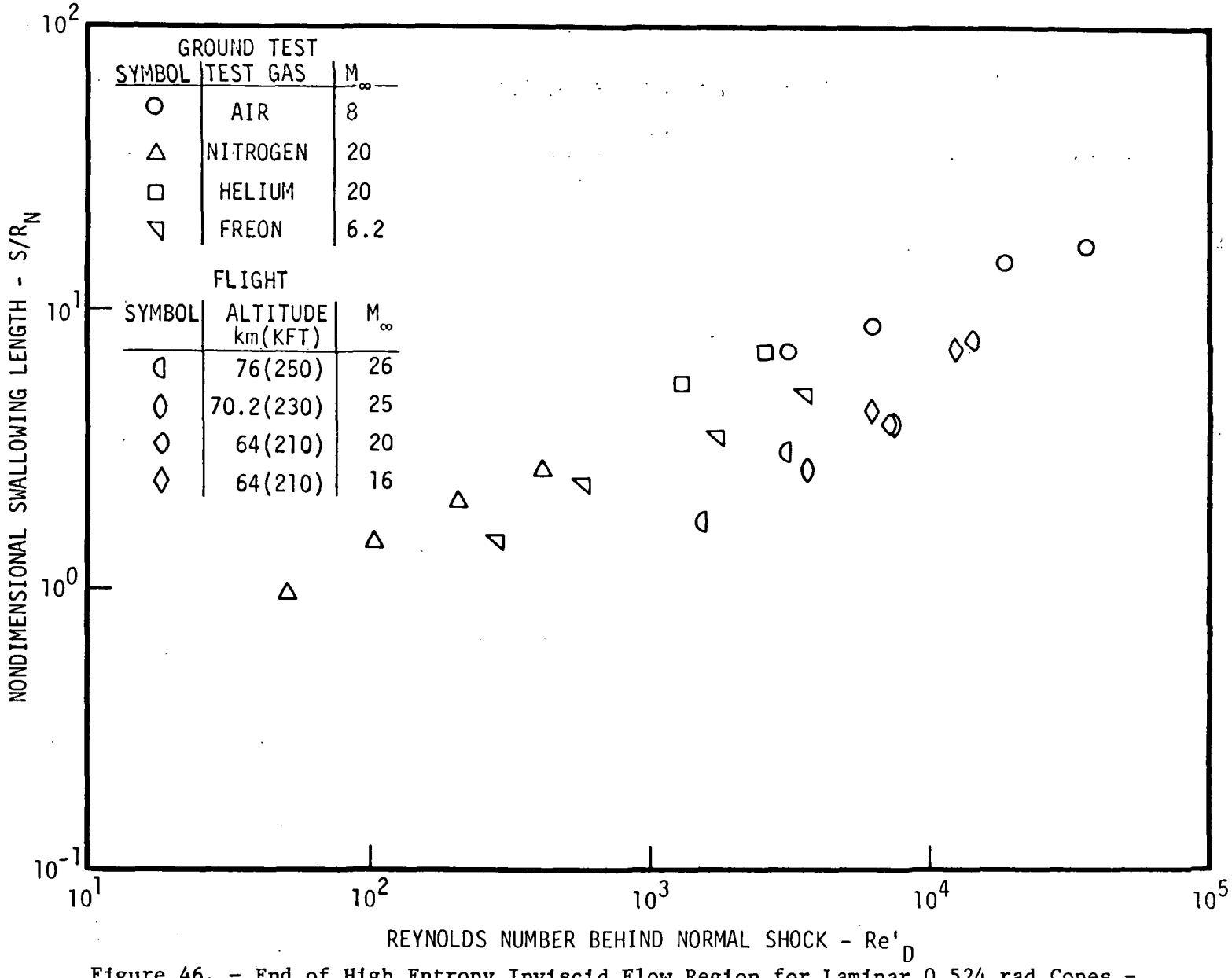

Figure 46. - End of High Entropy Inviscid Flow Region for Laminar 0.524 rad Cones - Correlated by Reynolds Number Behind Normal Shock.

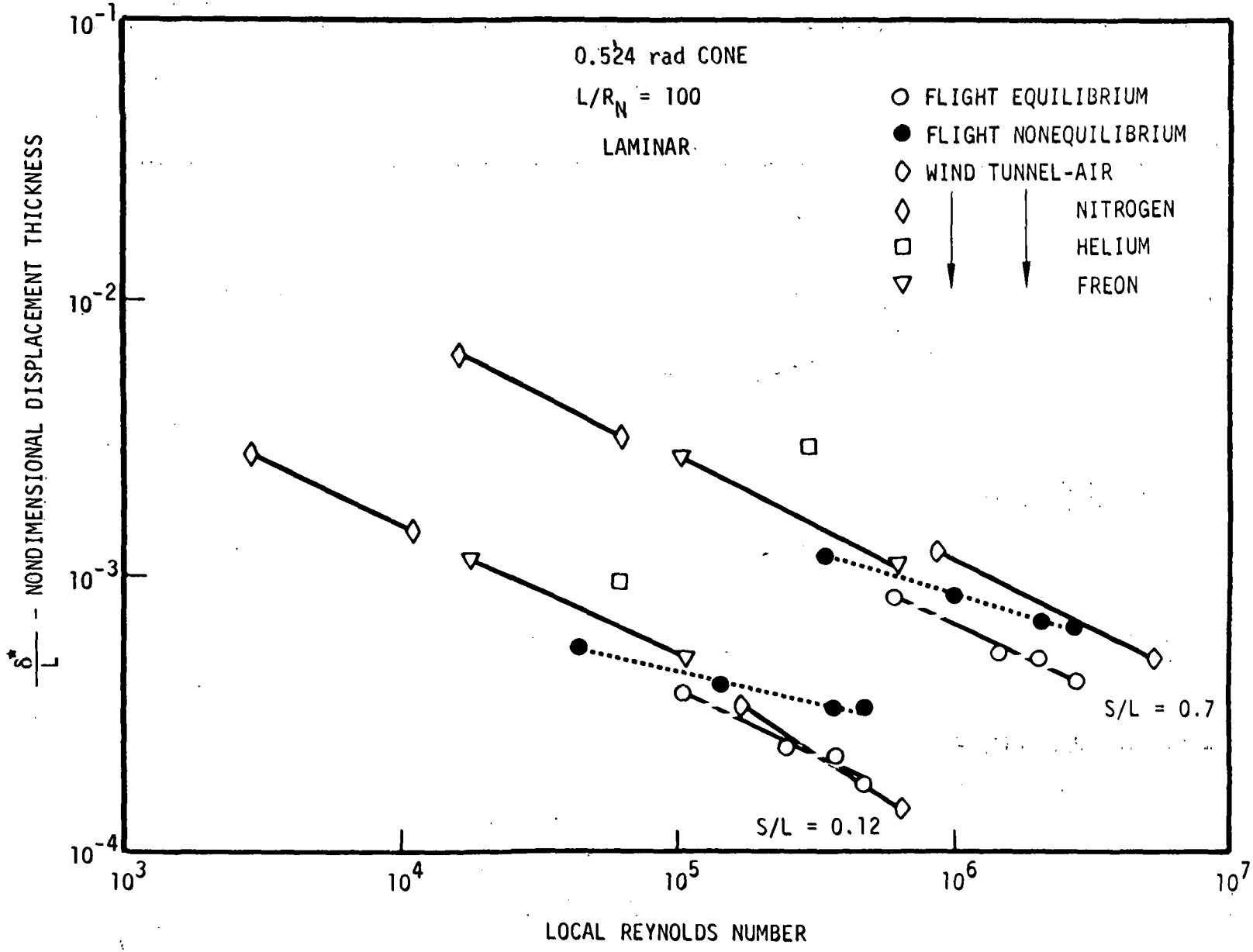

Figure 47. - Correlation of Laminar Boundary Layer Displacement Thickness for 0.524 rad Cones.

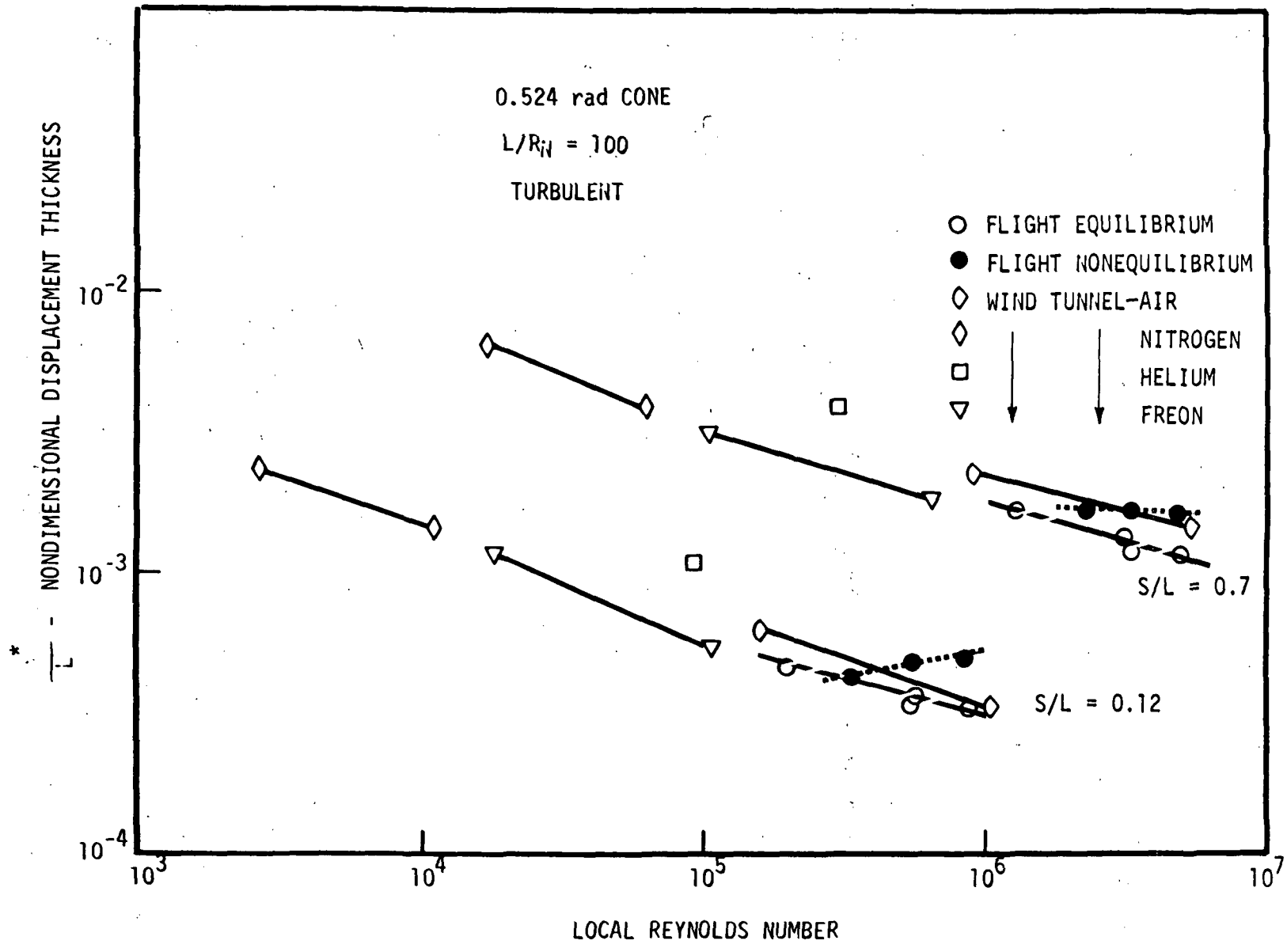

Figure 48. - Correlation of Turbulent Boundary Displacement Thickness for 0.524 rad Cones.

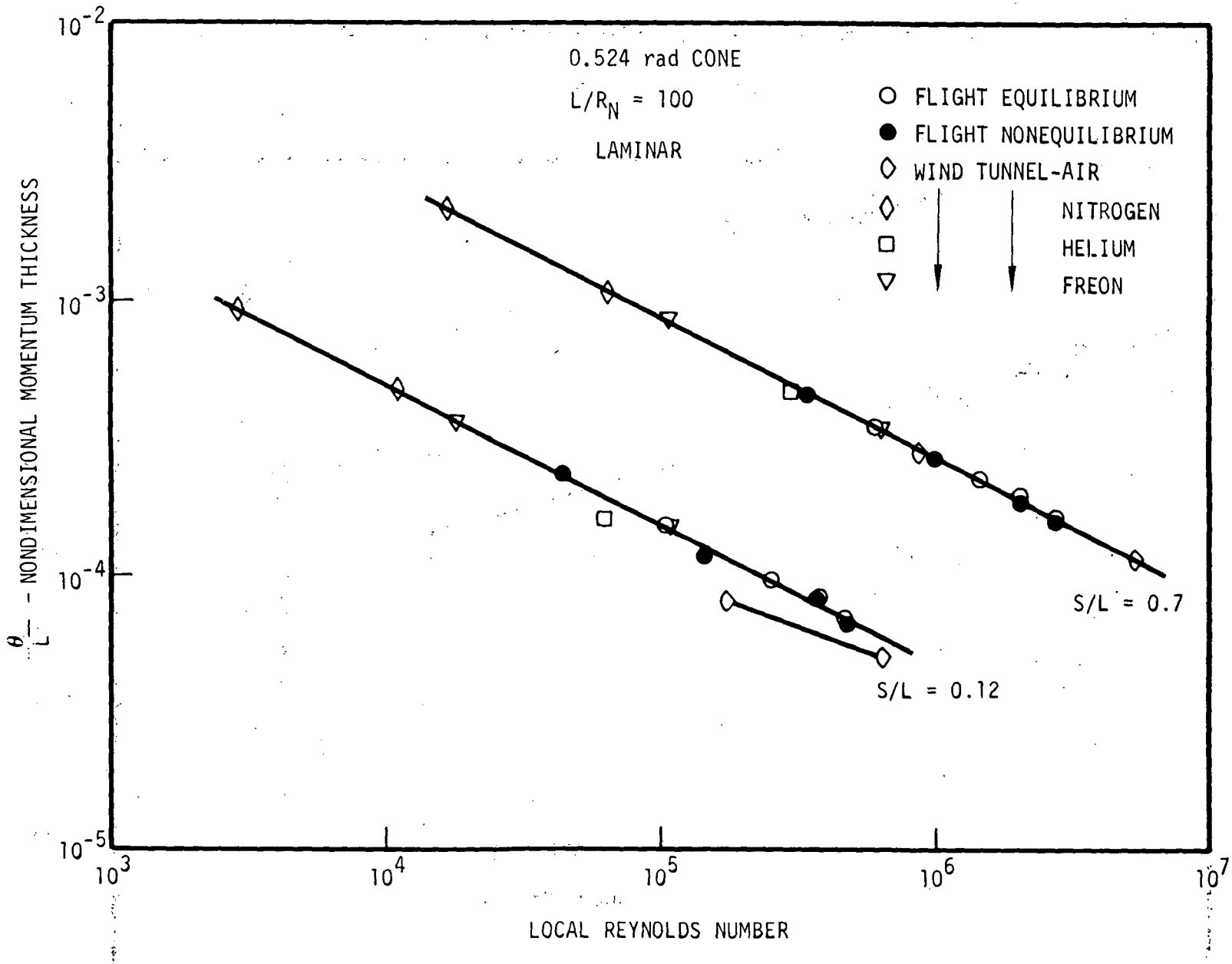

Figure 49. — Correlation of Laminar Boundary Layer Momentum Thickness for 0.524 rad Cones.

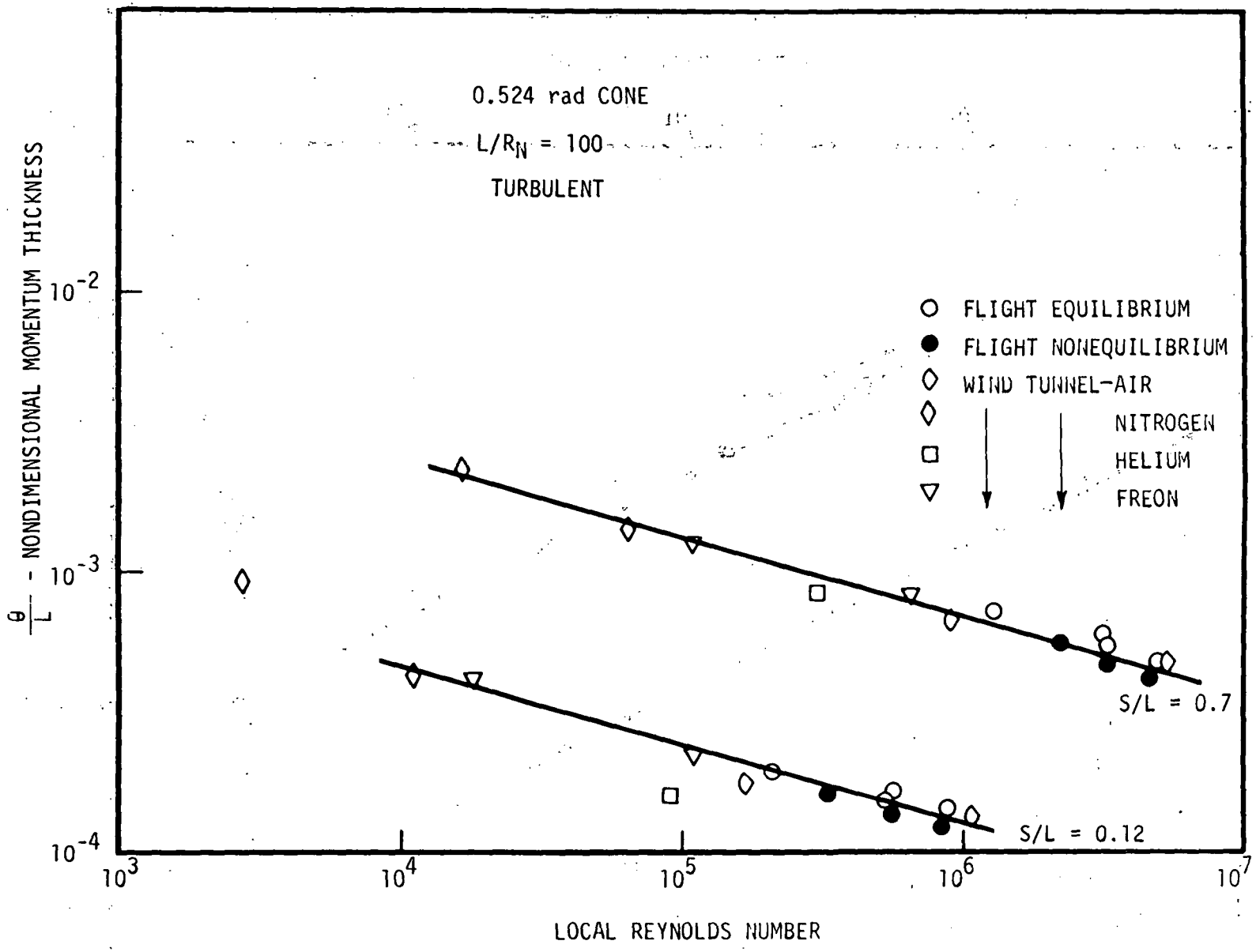

Figure 50. - Correlation of Turbulent Boundary Layer Momentum Thickness for 0.524 rad Cones.

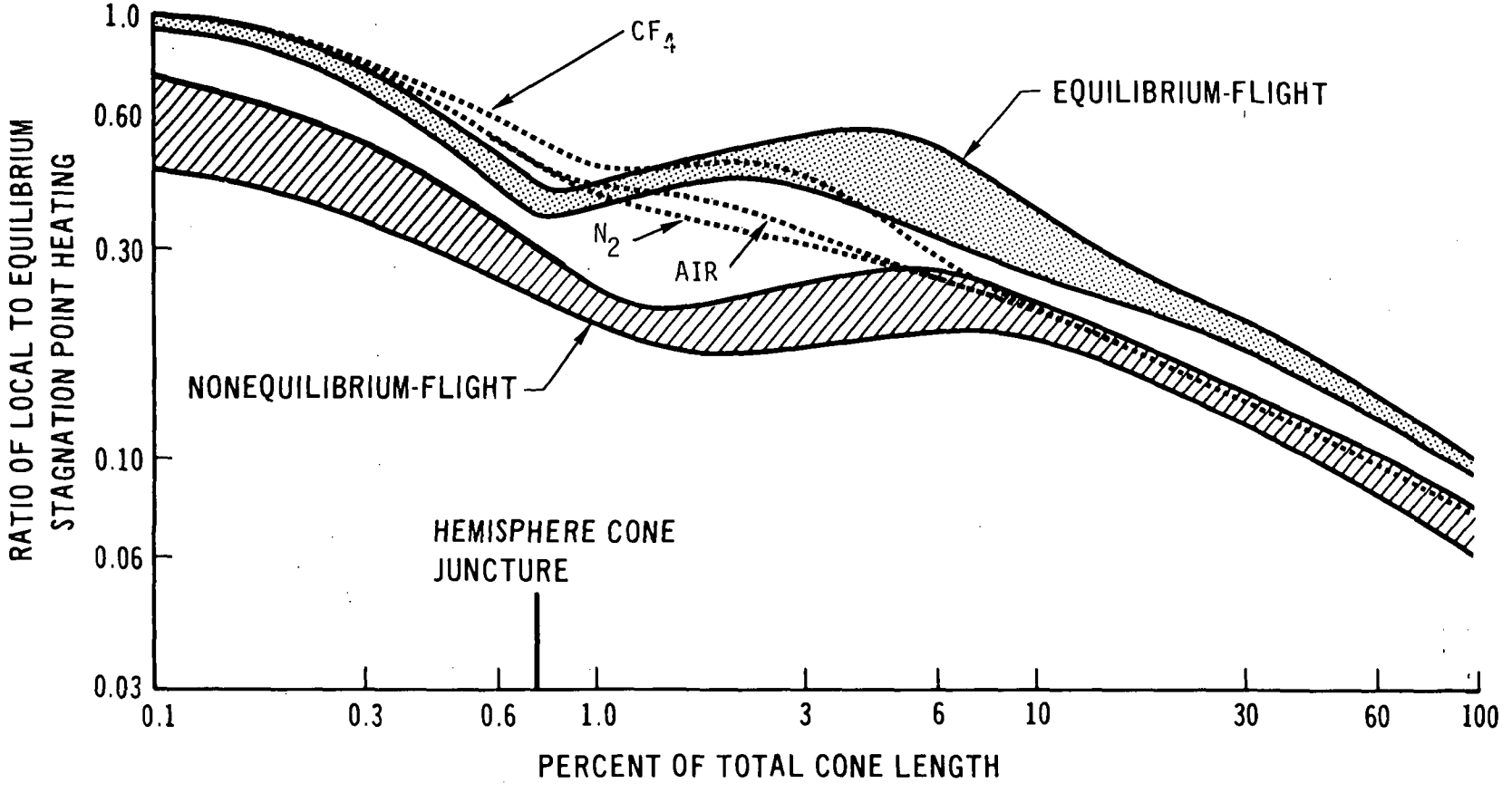

Figure 51. - Laminar Heating Rate Simulation.

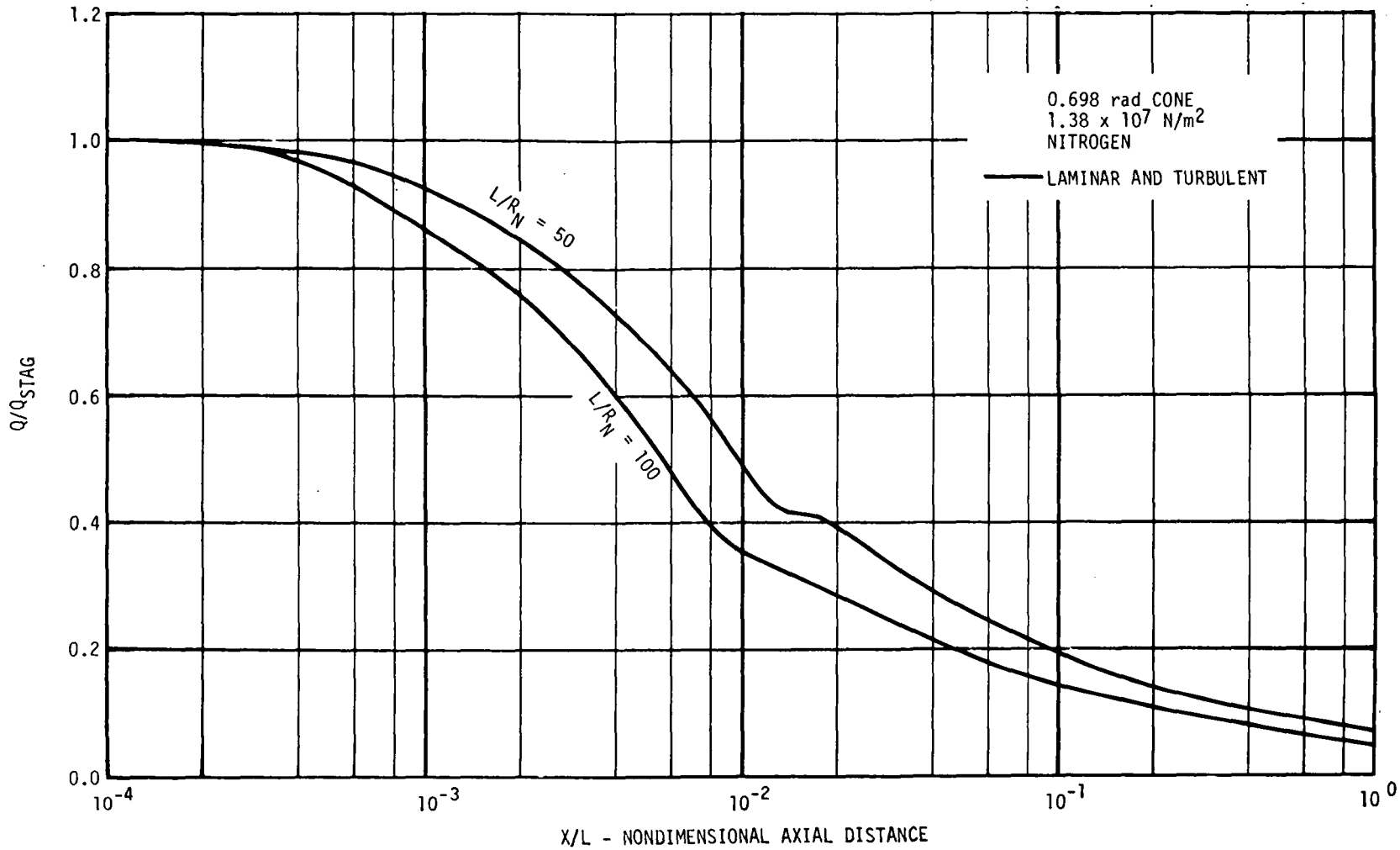

Figure 52. - Heating Rate Distribution in Low Pressure Nitrogen Wind Tunnel.

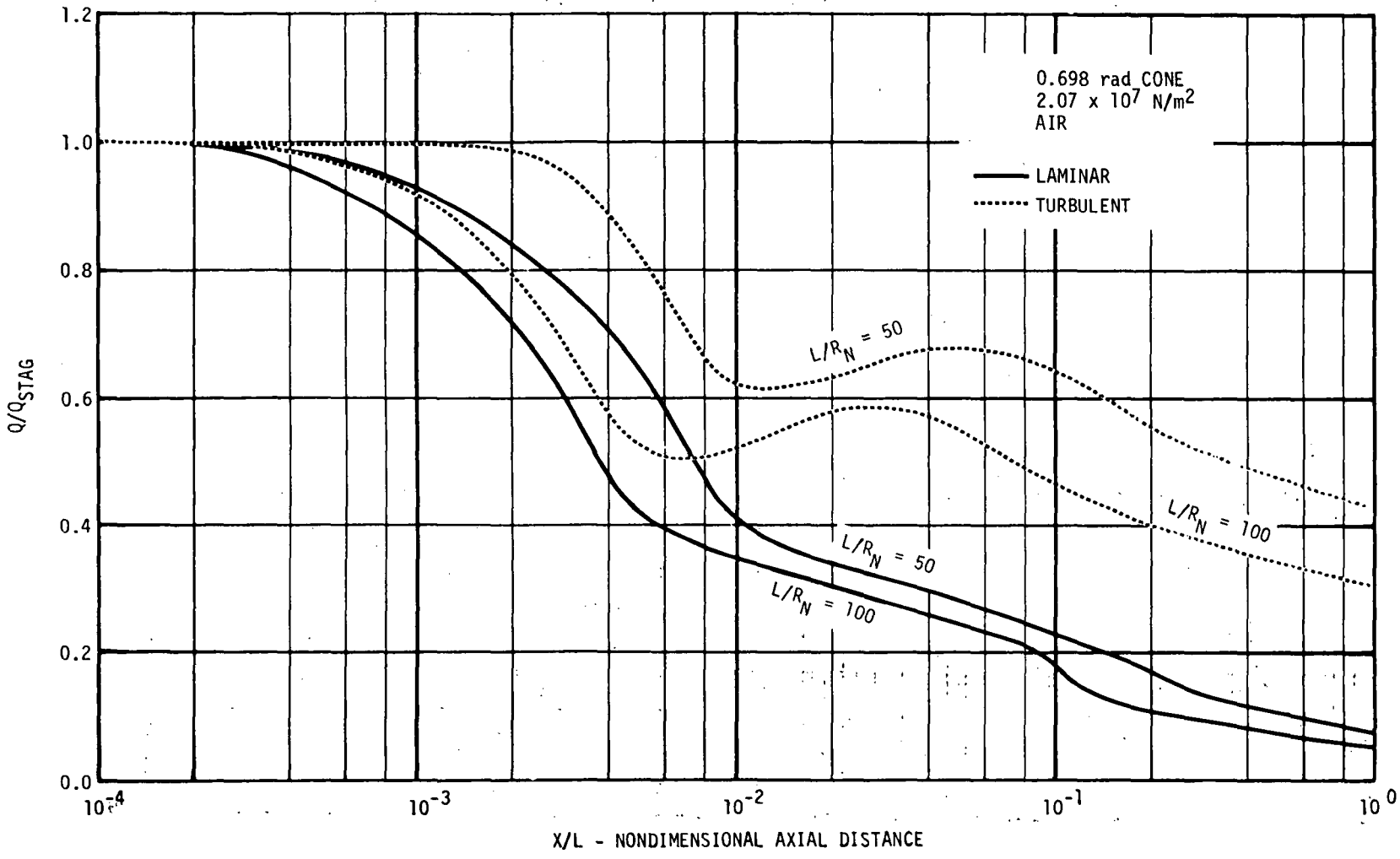

Figure 53. - Heating Rate Distribution in High Pressure Air Wind Tunnel.

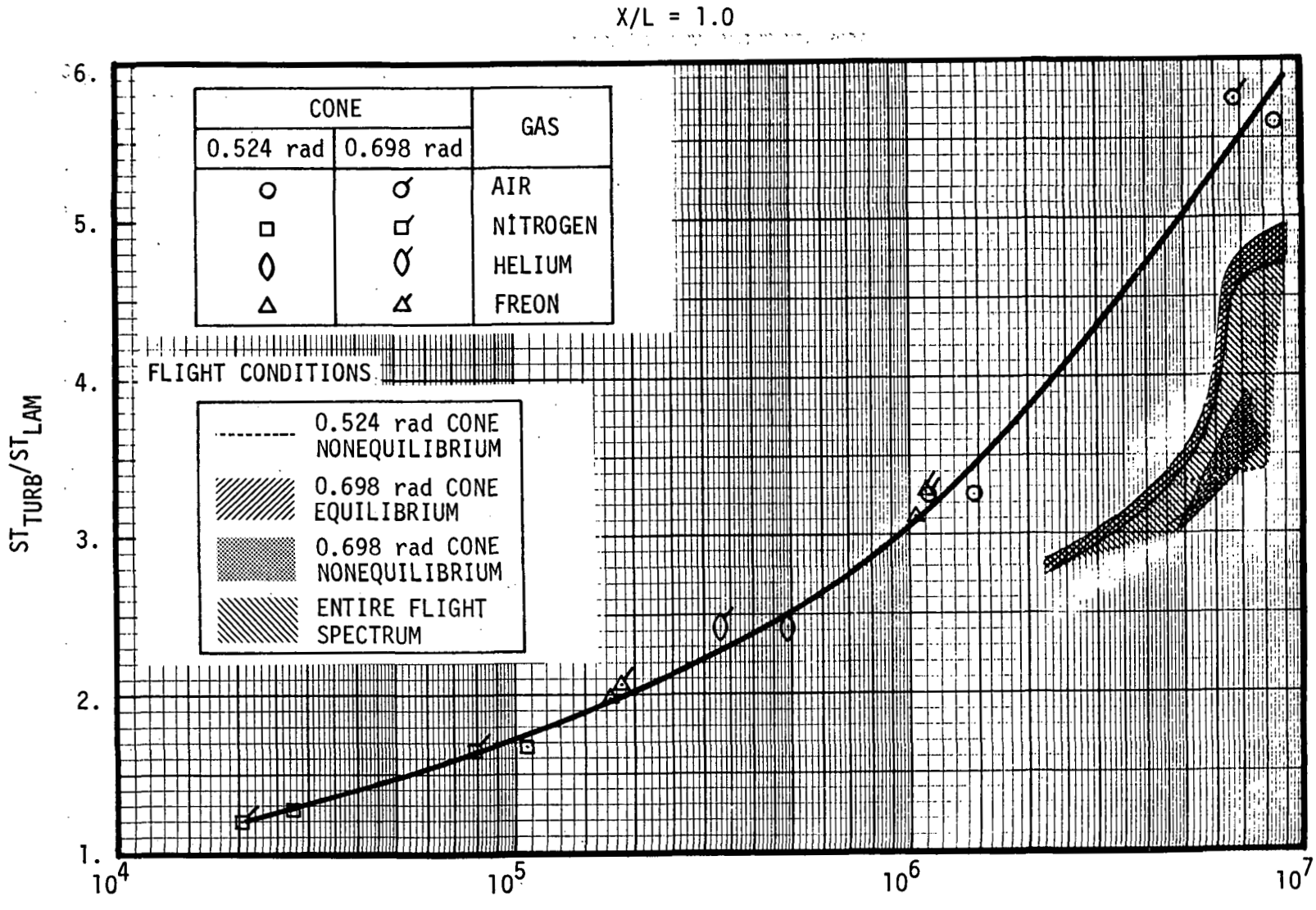

Figure 54. - Correlation of Turbulent to Laminar Stanton Number Ratio.

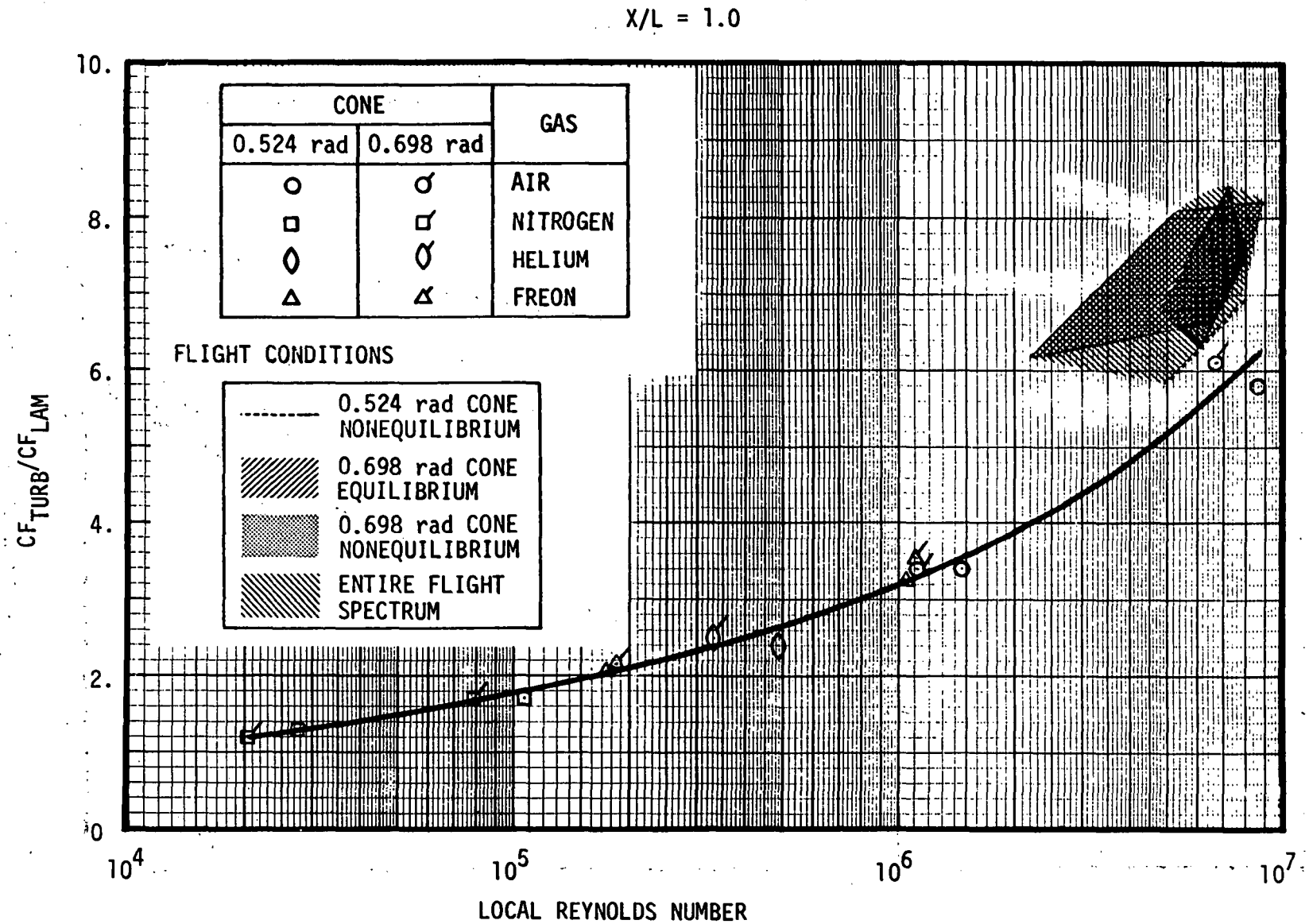

Figure 55. - Correlation of Turbulent to Laminar Skin Friction Coefficient Ratio.

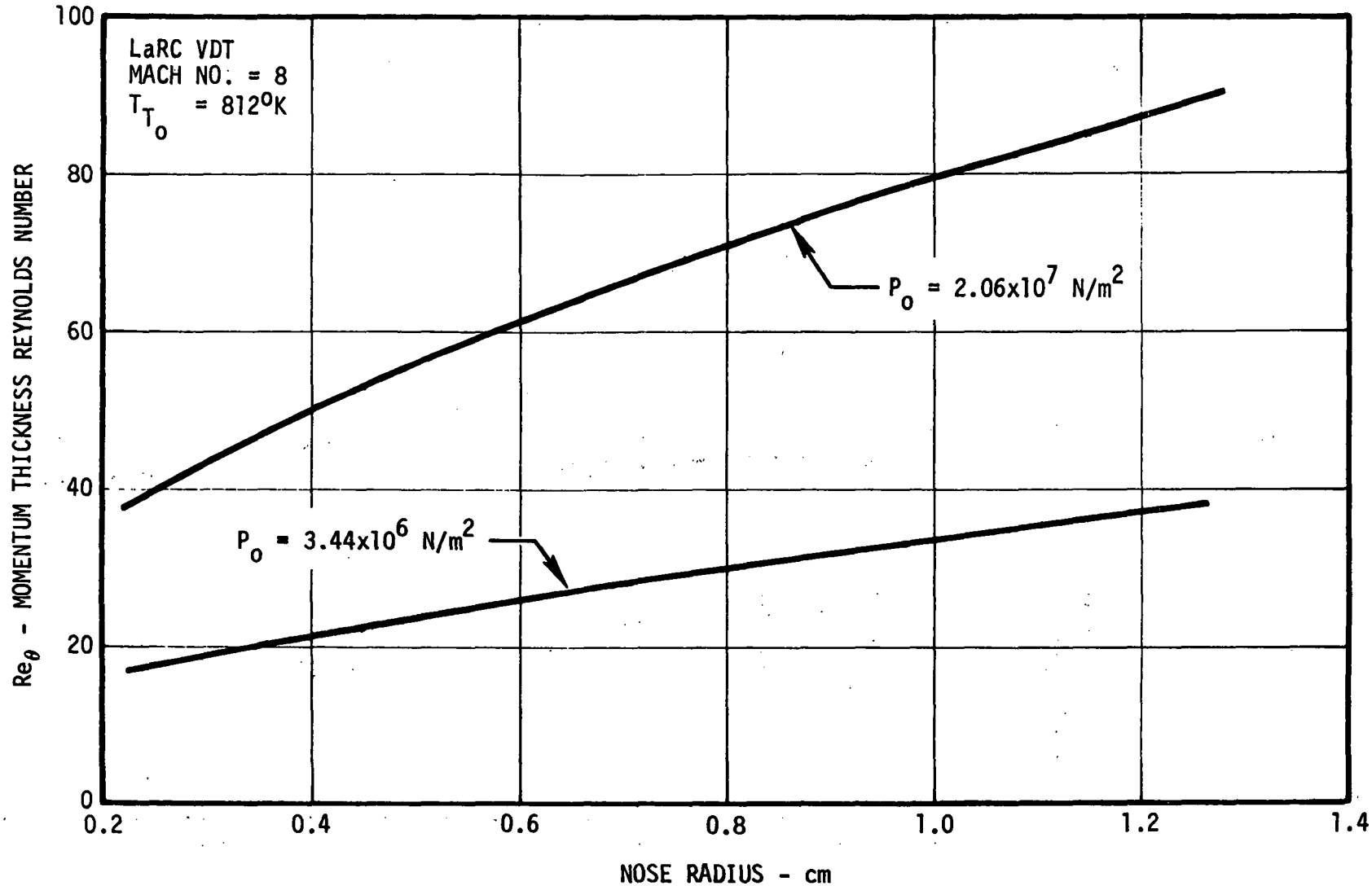

Figure 56. - Variation of Momentum Thickness Reynolds Number at Nose Tip Sonic Point.

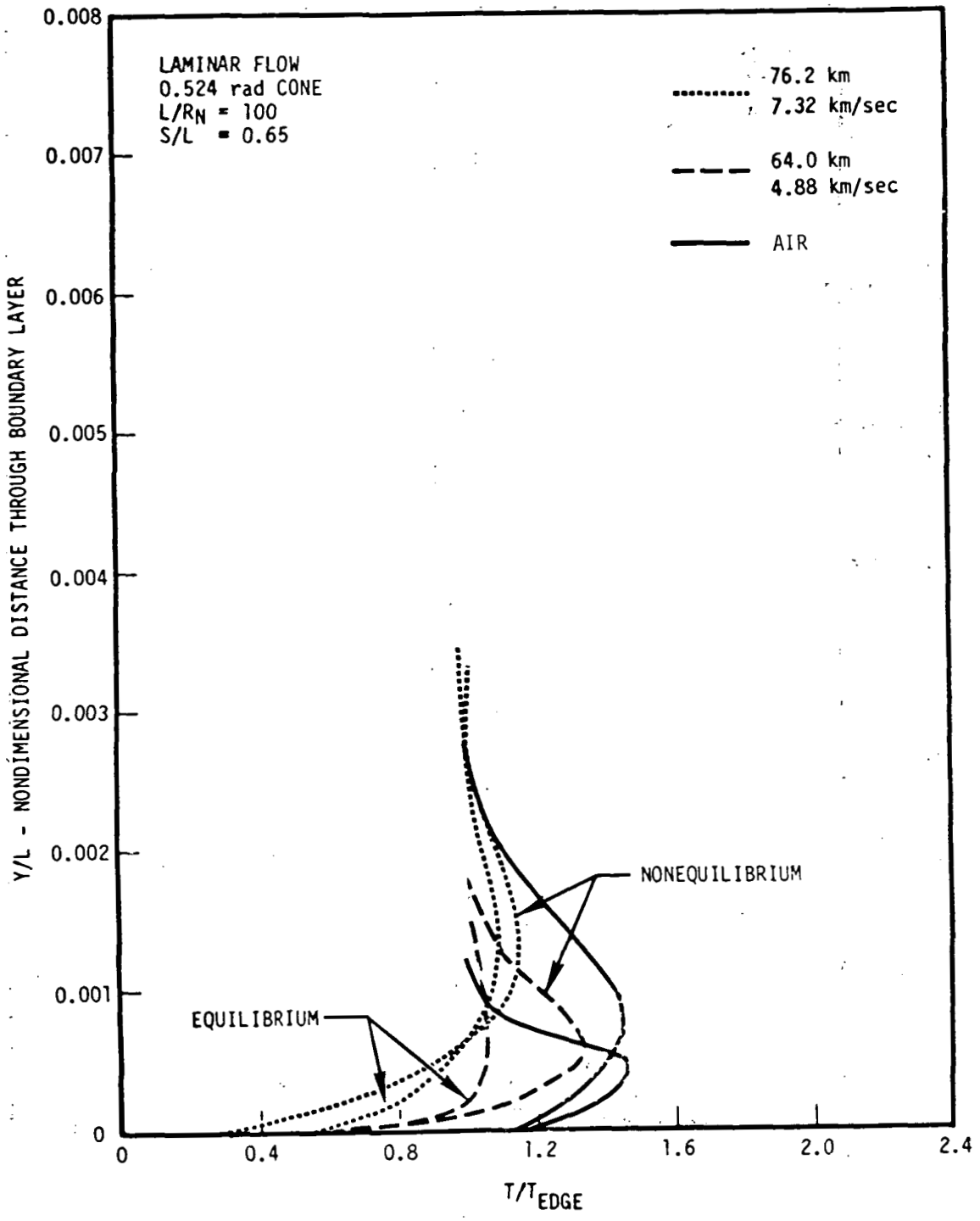

Figure 57. - Air Wind Tunnel Simulation of Flight Laminar Boundary Layer Temperature Profiles.

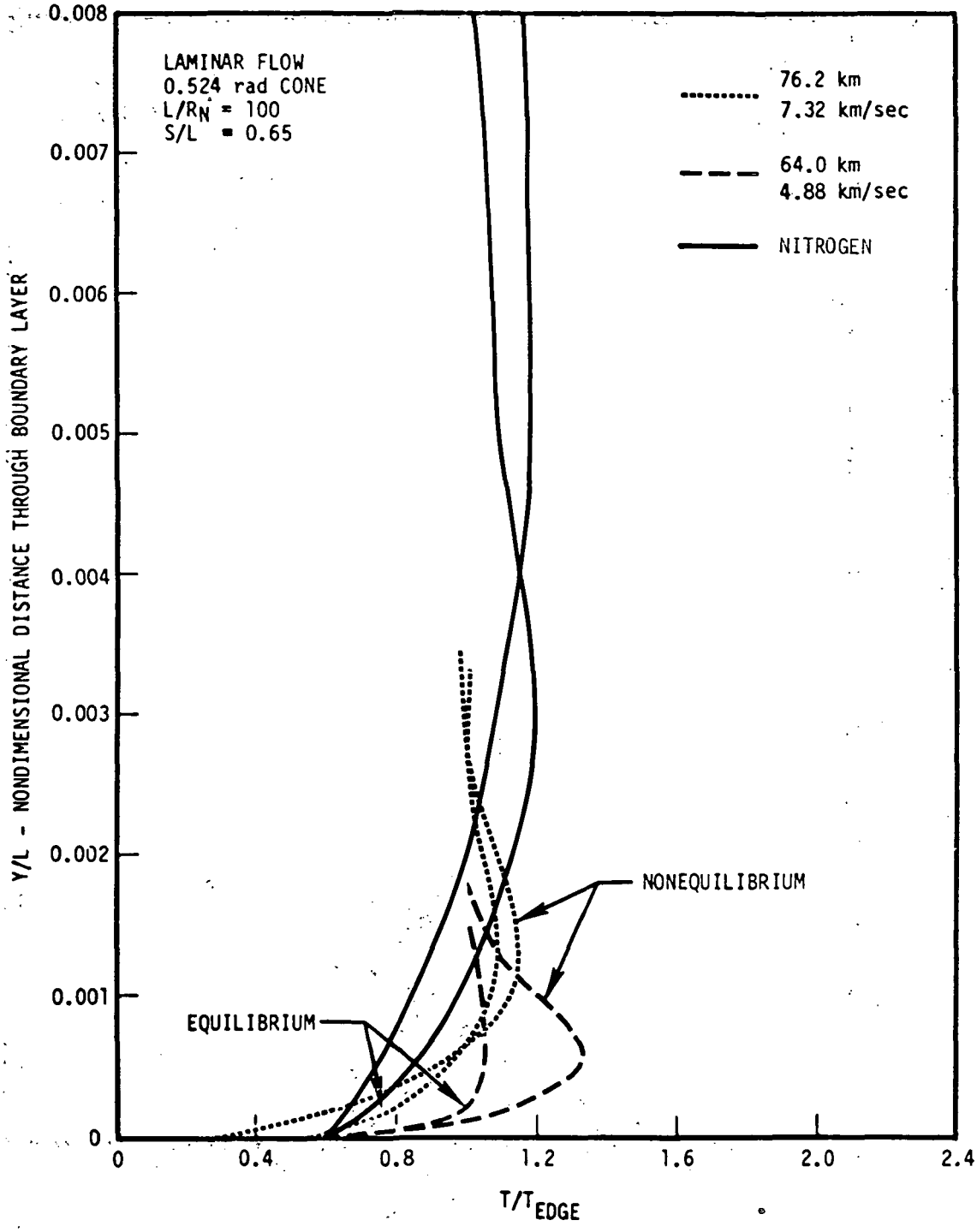

Figure 58. - Nitrogen Wind Tunnel Simulation of Flight Laminar Boundary Layer Temperature Profiles.

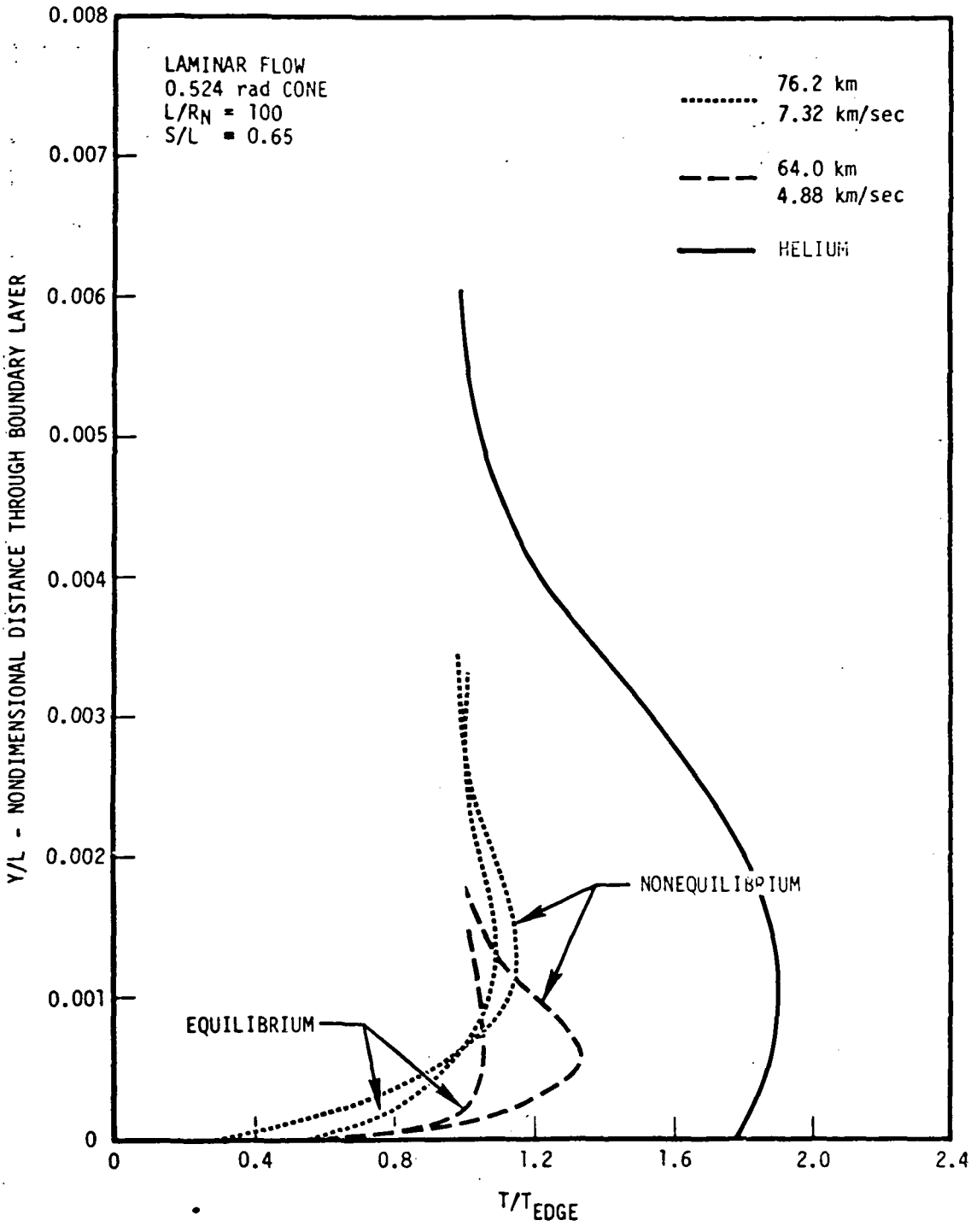

Figure 59. - Helium Wind Tunnel Simulation of Flight Laminar Boundary Layer Temperature Profiles.

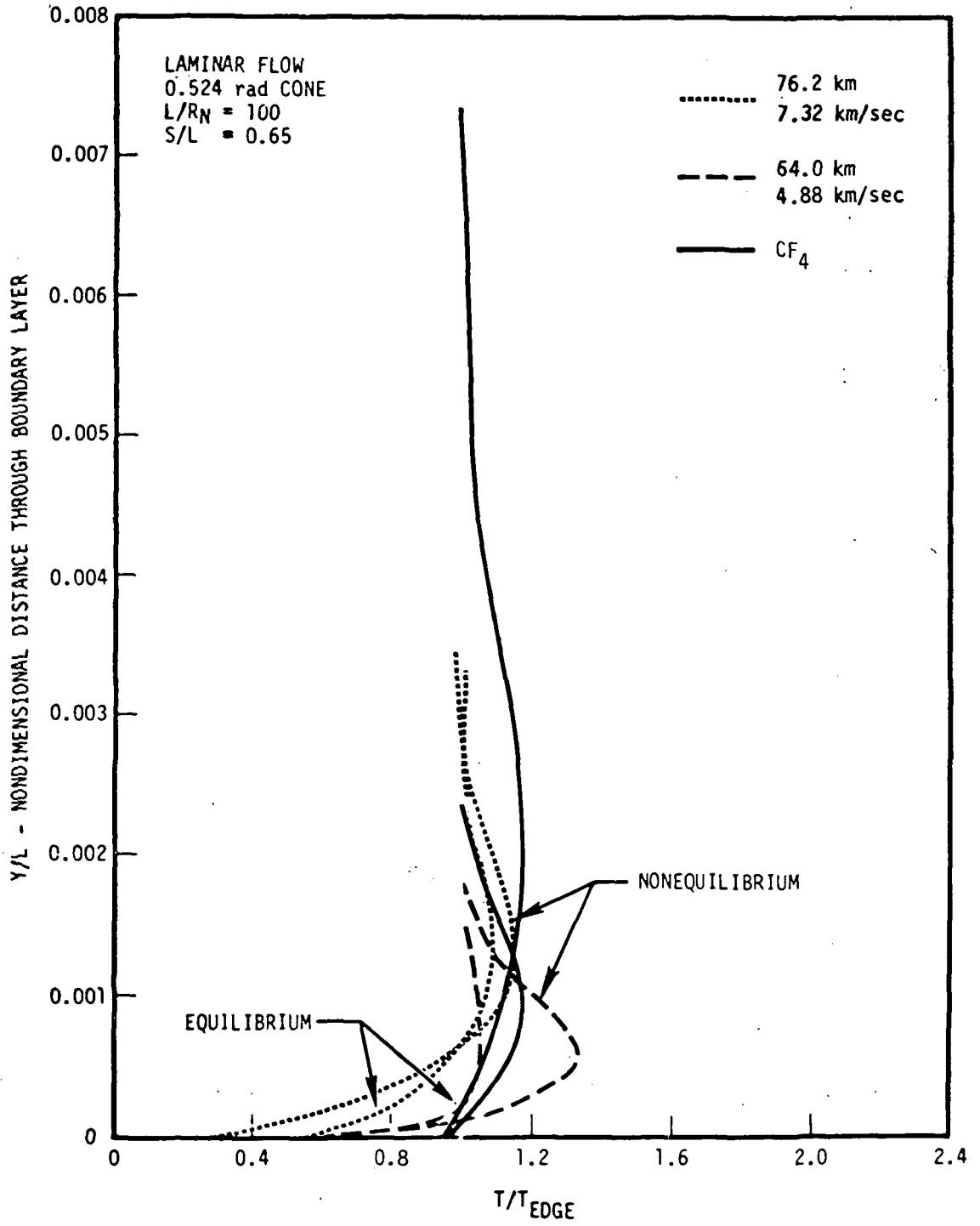

Figure 60. - Freon (CF_4) Wind Tunnel Simulation of Flight Laminar Boundary Layer Temperature Profiles.

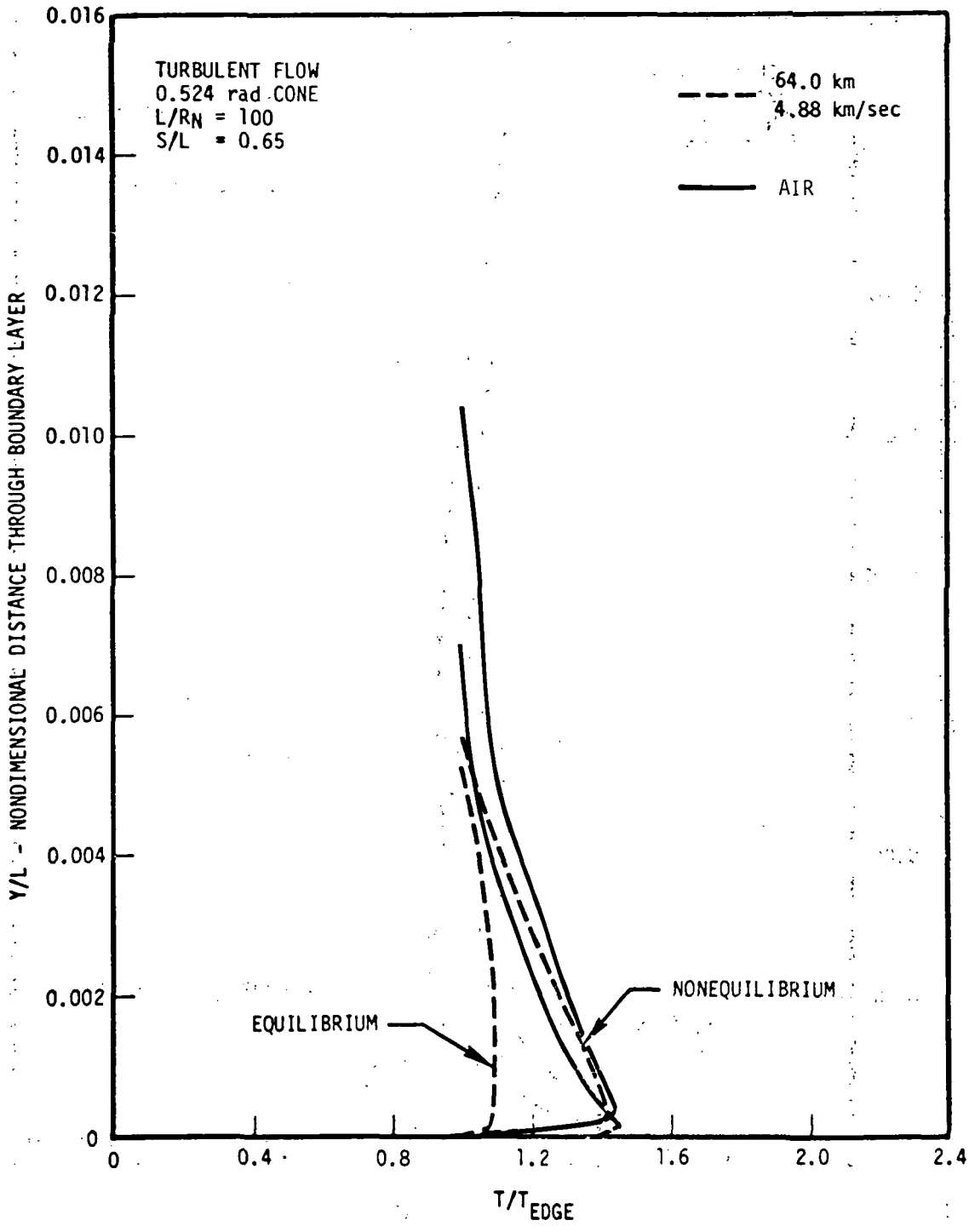

Figure 61. - Air Wind Tunnel Simulation of Flight Turbulent Boundary Layer Temperature Profiles.

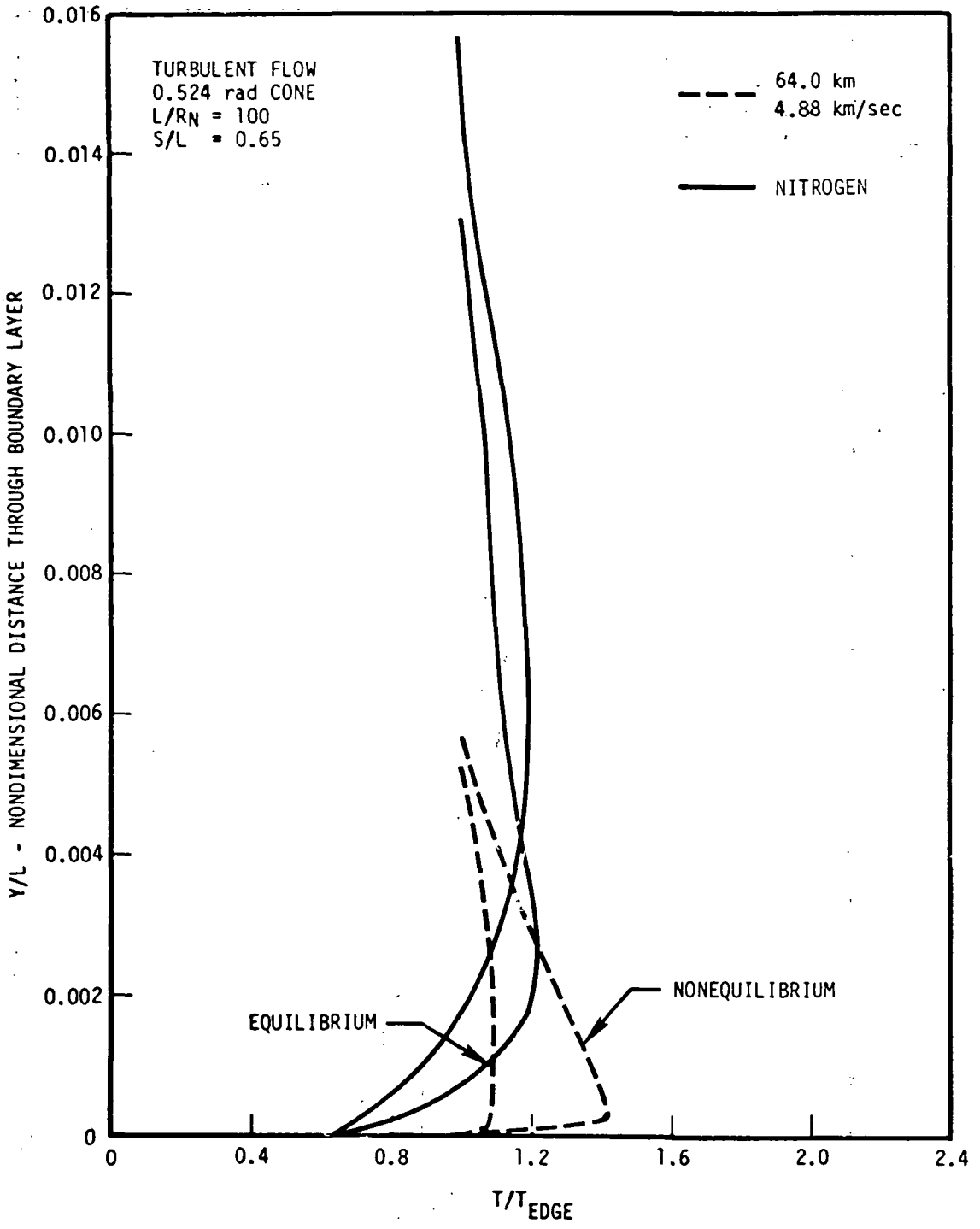

Figure 62. - Nitrogen Wind Tunnel Simulation of Flight Turbulent Boundary Layer Temperature Profiles.

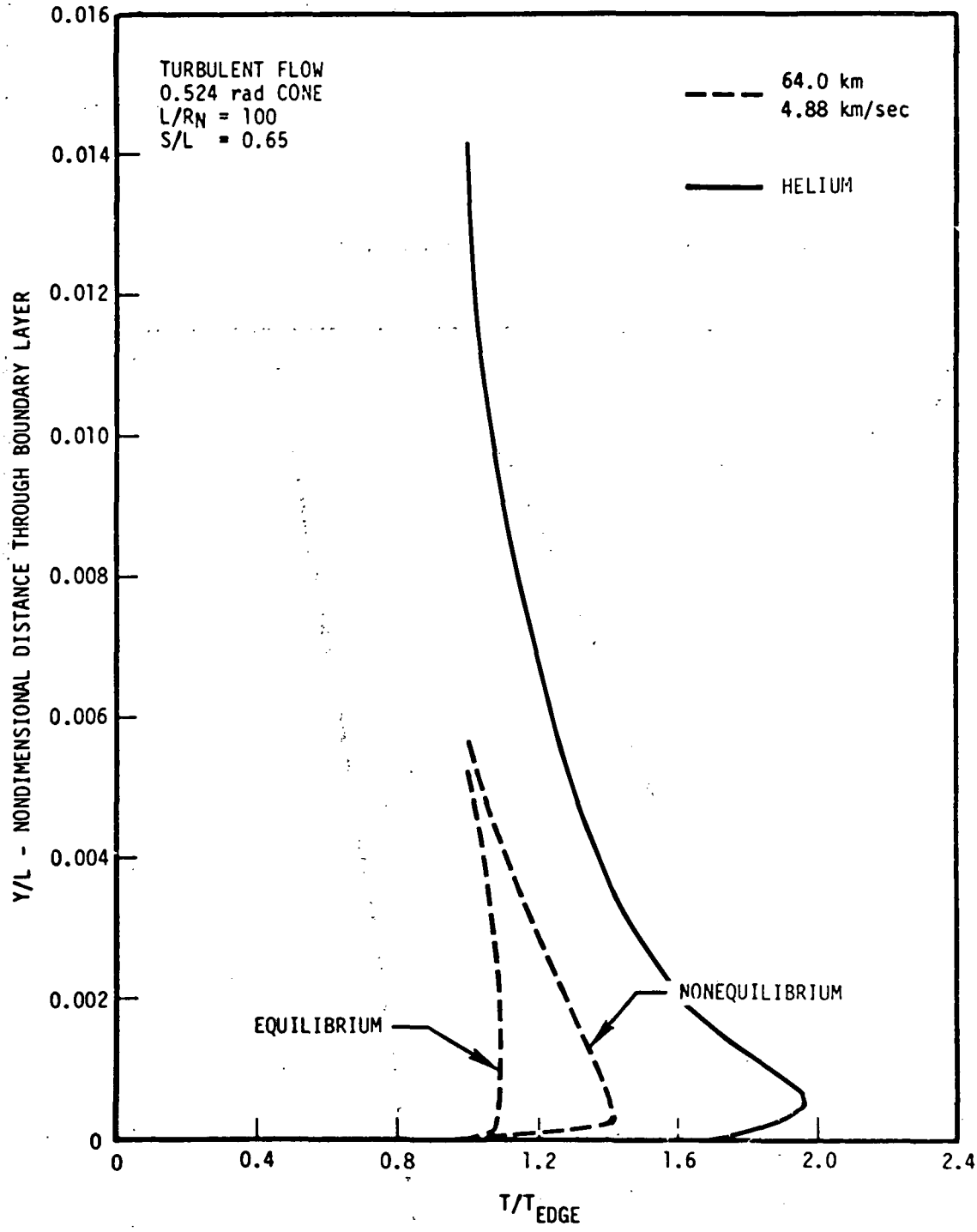

Figure 63. - Helium Wind Tunnel Simulation of Flight Turbulent Boundary Layer Temperature Profiles.

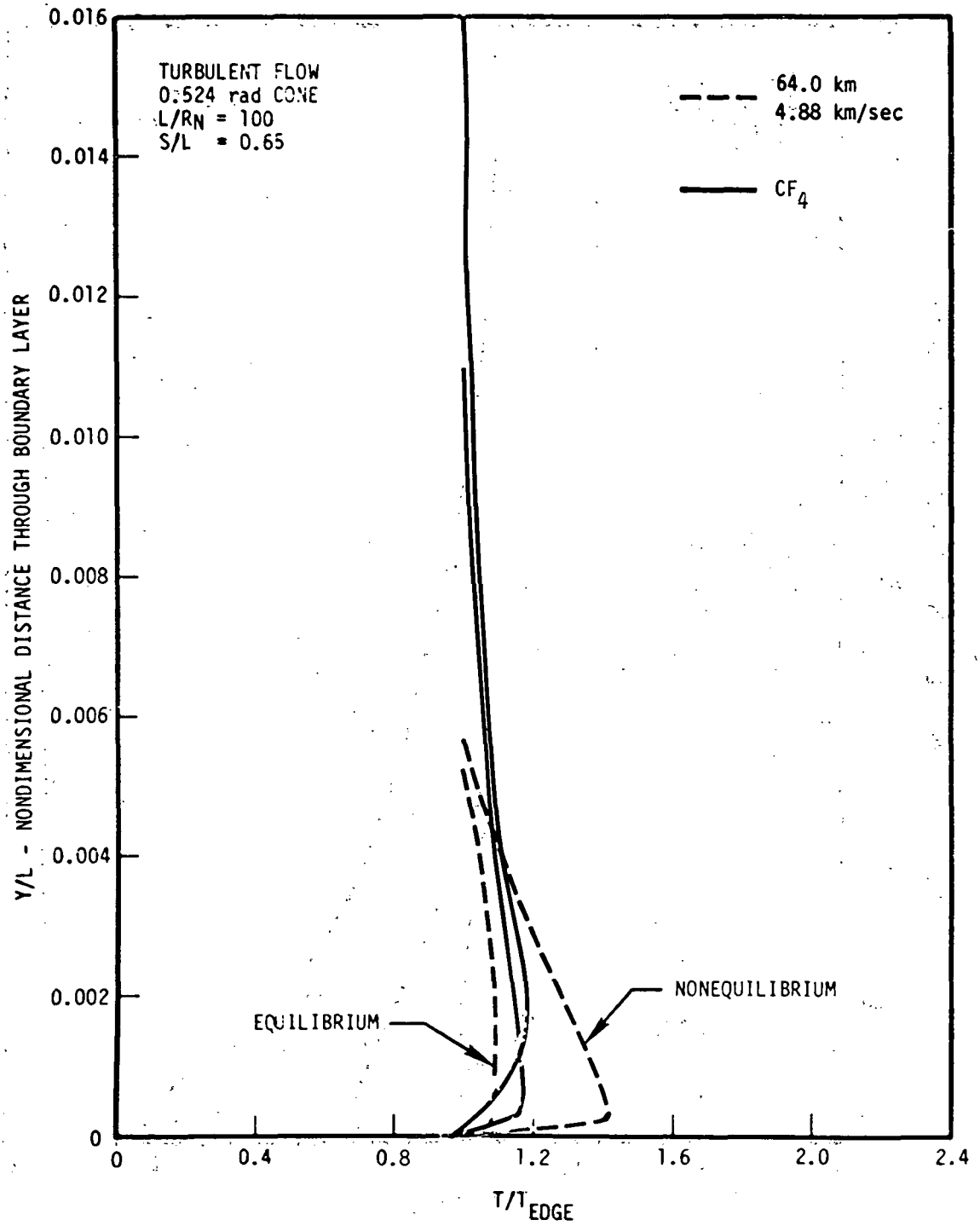

Figure 64. - Freon (CF_4) Wind Tunnel Simulation of Flight Turbulent Boundary Layer Temperature Profiles.

Appendix A

EDDY VISCOSITY MODEL FOR TURBULENT BOUNDARY LAYERS

The eddy viscosity formulation used in the nonsimilar, compressible viscous flow field code for turbulent flight conditions is modeled after the formulation of Cebeci and found in Reference 9. The turbulent boundary layer is characterized by two distinct regions: (1) an inner layer based on Prandtl's mixing length theory, and (2) an outer layer, based on a constant eddy viscosity modified by an intermittency factor. The expression for the eddy viscosity in the inner layer is given by

$$\epsilon_i = (0.4y)^2 \left[1 - \exp\left(-\frac{y}{A} \right) \right]^2 \left| \frac{\partial u}{\partial y} \right| \qquad \text{(A-1)}$$

where:

$$A = 26\,\nu \left(\frac{\tau_w}{\rho} + \frac{dp}{dx}\,\frac{y}{\rho} \right)^{-1/2} \qquad \text{(A-2)}$$

and

u = streamwise component of velocity

y = distance through boundary layer normal to wall

$\frac{dp}{dx}$ = pressure gradient

ϵ_i = kinematic eddy viscosity, inner region

ν = kinematic viscosity

ρ = density

τ_w = shear stress at the wall

The expression for the eddy viscosity in the outer region is given by

$$\epsilon_o = 0.0168\, u_e\, \delta^*_{inc}\, \gamma \qquad \text{(A-3)}$$

where:

$$\delta^*_{inc} = \int_o^\infty \left(1 - \frac{u}{u_e} \right) dy \qquad \text{(A-4)}$$

$$\gamma = \left[1 + 5.5\left(\frac{y}{\delta}\right)^6\right]^{-1} \qquad \text{(A-5)}$$

and

u_e = streamwise velocity at boundary layer edge

γ = intermittency factor

δ^*_{inc} = incompressible form of displacement thickness

δ = boundary layer thickness

ϵ_o = kinematic eddy viscosity, outer region

A typical eddy viscosity variation across the boundary layer is presented in Figure A-1. The plotted values are $\rho\varepsilon$, i.e. the dynamic eddy viscosity. The switch-over from the inner layer formulation to the outer layer formulation occurs at the point where the two curves cross, at approximately $\eta = 1$ for this case. The laminar viscosity is included in the figure for comparison.

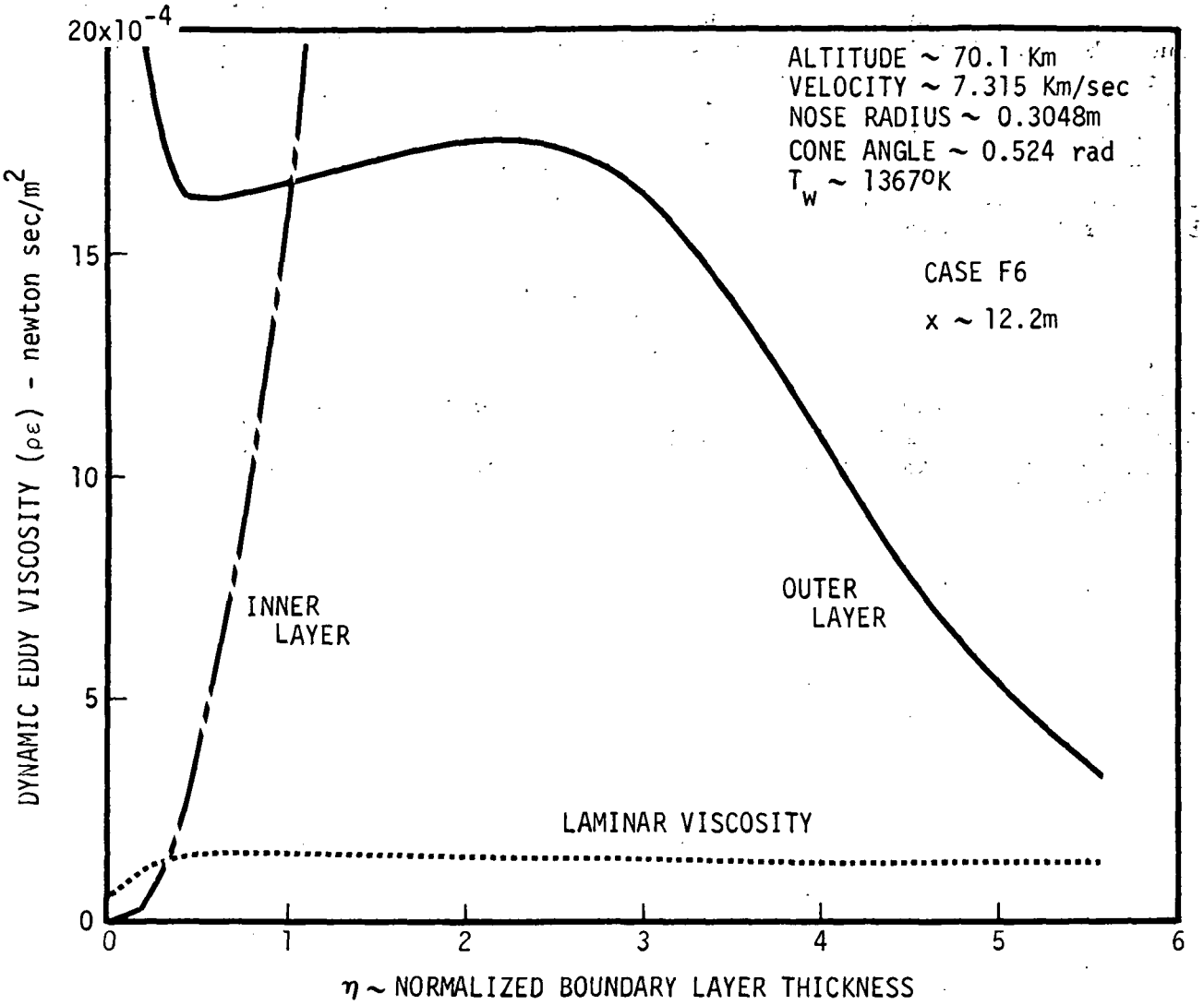

Figure A-1. - Turbulent Boundary Layer Eddy Viscosity Profile.

Appendix B

CHEMICAL REACTIONS FOR SHUTTLE NONEQUILIBRIUM EFFECTS

The chemical reactions used in the nonequilibrium portion of the present study, both inviscid and viscous flow fields, are listed in Table B-1. It is felt that these particular reactions are the most important reactions in determining the nonequilibrium effects in the Shuttle flow field at typical entry conditions. The forward rate constants, also listed in Table B-1, best describe the reaction rates over the temperature range encountered in the altitude-velocity regime selected for the study. The reaction rates are given by the following expression:

$$k = a\, T^{b}\, e^{(-E/T)} \qquad \text{(B-1)}$$

where units are gram moles, cm^3, sec, and ^{o}K. Reverse reaction rate constants were determined from the forward values and the equilibrium constant for each reaction, fitting the constants at three temperatures: $1000^{o}K$, $6000^{o}K$, and $12000^{o}K$.

TABLE B-I

CHEMICAL REACTIONS FOR SHUTTLE NONEQUILIBRIUM EFFECTS

	REACTION	FORWARD REACTION RATE CONSTANTS			REVERSE REACTION RATE CONSTANTS		
		a	b	E	a	b	E
1.	$O_2 + M \rightarrow 2O + M$	6.30 E18	-1.0	59357	8.5982 E16	-0.7954	0.00
2.	$N_2 + M \rightarrow 2N + M$	2.46 E19	-1.0	113200	3.2489 E19	-1.3509	609.68
3.	$NO + M \rightarrow O + N + M$	5.50 E20	-1.5	75483	1.2083 E20	-1.4801	0.00
4.	$O + NO \rightarrow N + O_2$	3.20 E9	1.0	19676	6.5504 E12	0.3115	4915.60
5.	$O + N_2 \rightarrow N + NO$	7.34 E11	0.5	37950	4.4495 E12	0.1283	845.02
6.	$O_2 + O \rightarrow 2O + O$	6.00 E19	-1.0	59357	8.1887 E17	-0.7954	0.00
7.	$N2 + N \rightarrow 2N + N$	1.75 E20	-1.0	113200	2.3112 E20	-1.3509	609.68
8.	$O + N \rightarrow NO^+ + e^-$	2.43 E10	0.5	32400	1.0347 E20	-1.0476	672.72

$$k = a\, T^b\, e^{(-E/T)}$$

(UNITS ARE GRAM MOLES, cm^3, SEC, AND ^oK)

Appendix C

INVISCID FLOW FIELD SHOCK SHAPES

The shock shapes for the equilibrium inviscid flow fields generated for this study are presented in this appendix. Both flight condition cases and ideal gas wind tunnel cases are included. Data are in tabular form, listing the coordinates of the shock in a body-coordinate system. Each entry is normalized by nose radius, thus enabling the user to determine the shock shape for other nose radii than those used for this study.

SHOCK SHAPES FOR EQUILIBRIUM FLIGHT CONDITIONS

CASE 1
H = 76.2 km (250 KFT)
V_∞ = 7.315 km/sec (24000 FPS)
θ_C = 30°
R_N = 0.6096 m (2 FT)

X/R_N	Y/R_N
- .0447	0.0
- .0361	.1385
- .0111	.2728
.0288	.4008
.0816	.5209
.1468	.6346
.2197	.7379
.3015	.8348
.4081	.9411
.5463	1.0572
.7224	1.1814
.9446	1.3123
1.2143	1.4574
1.5132	1.6162
1.8292	1.7873
2.1706	1.9832
2.5763	2.2267
2.9236	2.4401
3.3610	2.7080
3.8951	3.0319
4.5578	3.4313
5.4588	3.9773
6.3959	4.5495
7.5755	5.2709
8.8146	6.0279
10.3531	6.9686
11.9885	7.9695
13.8083	9.0845
15.7187	10.2537
18.0134	11.6595
20.3385	13.0836
25.0000	15.9129
50.0000	31.0872

CASE 2
H = 70.1 km (230 KFT)
V_∞ = 7.315 km/sec (24000 FPS)
θ_C = 30°
R_N = 0.6096 m (2 FT)

X/R_N	Y/R_N
- .0463	0.0
- .0376	.1391
- .0125	.2740
.0276	.4027
.0806	.5230
.1476	.6397
.2125	.7324
.2946	.8312
.4021	.9399
.5338	1.0525
.9045	1.2968
1.1529	1.4317
1.4671	1.5988
1.7391	1.7446
2.0475	1.9171
2.3267	2.0804
2.6925	2.3017
2.9984	2.4899
3.2100	2.6197
3.5938	2.8542
4.0105	3.1067
4.5140	3.4103
5.0821	3.7538
5.7277	4.1463
6.3283	4.5134
7.1169	4.9961
7.8349	5.4355
8.7634	6.0034
9.9834	6.7497
11.4669	7.6581
13.0426	8.6238
14.7770	9.6869
16.5321	10.7630
18.9640	12.2540
25.0000	15.9572
50.0000	31.2952

CASE 3
H = 64.0 km (210 KFT)
V_∞ = 6.096 km/sec (20000 FPS)
θ_C = 30°
R_N = 0.6096 m (2 FT)

X/R_N	Y/R_N
- .0545	0.0
- .0458	.1407
- .0206	.2777
.0194	.4079
.0745	.5344
.1406	.6510
.2083	.7489
.2840	.8419
.3862	.9484
.4880	1.0393
.6719	1.1777
.8311	1.2804
1.0642	1.4080
1.3046	1.5450
1.5627	1.6837
1.8859	1.8583
2.0700	1.9618
2.3787	2.1416
2.6886	2.3280
3.0567	2.5550
3.3656	2.7464
3.7178	2.9639
4.1599	3.2356
4.6841	3.5556
5.1032	3.8113
5.6589	4.1513
6.4679	4.6485
7.3166	5.1725
8.4471	5.8713
9.3050	6.4014
10.5718	7.1841
12.0089	8.0725
13.4334	8.9537
14.9924	9.9187
16.8527	11.0705
18.8034	12.2783
20.7800	13.5021
23.1513	14.9706
25.0000	24.2967
50.0000	39.7872

SHOCK SHAPES FOR EQUILIBRIUM FLIGHT CONDITIONS

CASE 4
H = 64.0 km (210 KFT)
V_∞ = 4.876 km/sec (16000 FPS)
θ_C = 30°
R_N^C = 0.6096 m (2 FT)

X/R_N	Y/R_N
- .0660	0.0
- .0582	.1354
- .0356	.2665
- .0016	.3853
.0682	.5497
.1371	.6687
.2089	.7695
.2875	.8631
.3928	.9705
.5062	1.0704
.6550	1.1845
.8222	1.2970
1.0354	1.4236
1.2502	1.5423
1.5067	1.6830
1.8183	1.8555
2.1900	2.0692
2.4752	2.2411
2.9573	2.5400
3.3230	2.7707
3.7167	3.0194
4.1208	3.2736
4.6327	3.5942
5.1722	3.9314
5.7603	4.2992
6.3447	4.6657
7.1589	5.1778
8.2918	5.8920
9.0241	6.3542
10.4709	7.2673
12.1225	8.3099
13.2740	9.0370
15.0744	10.1742
25.0000	16.4493
50.0000	32.2548

CASE 5
H = 76.2 km (250 KFT)
V_∞ = 7.315 km/sec (24000 FPS)
θ_C = 30°
R_N = 0.3048 m (1 FT)

X/R_N	Y/R_N
- .0447	0.0
- .0361	.1385
- .0111	.2728
.0288	.4008
.0816	.5209
.1468	.6346
.2197	.7379
.3015	.8348
.4081	.9411
.5463	1.0572
.7224	1.1814
.9464	1.3123
1.2143	1.4574
1.5132	1.6162
1.8292	1.7873
2.1706	1.9832
2.5763	2.2267
2.9236	2.4401
3.3610	2.7080
3.8951	3.0319
4.5578	3.4313
5.4588	3.9773
6.3959	4.5495
7.5755	5.2709
8.814	6.0279
10.353	6.9686
11.9885	7.9695
13.8083	9.0845
15.7187	10.2537
18.0134	11.6595
20.3385	13.0836
25.0000	15.9129
50.0000	31.0872

CASE 6
H = 70.1 km (230 FT)
V_∞ = 7.315 km/sec (24000 FPS)
θ_C = 30°
R_N^C = 0.3048 m (1 FT)

X/R_N	Y/R_N
- .0463	0.0
- .0376	.1391
- .0125	.2740
.0276	.4027
.0806	.5230
.1476	.6397
.2125	.7324
.2946	.8312
.4021	.9399
.5338	1.0525
.9045	1.2968
1.1529	1.4317
1.4671	1.5988
1.7391	1.7446
2.0475	1.9171
2.3267	2.0804
2.6925	2.3017
2.9984	2.4899
3.2100	2.6197
3.5938	2.8542
4.0105	3.0167
4.5140	3.4103
5.0821	3.7538
5.7277	4.1463
6.3283	4.5134
7.1169	4.9961
7.8349	5.4355
8.7634	6.0034
9.9834	6.7497
11.4669	7.6581
13.0426	8.6238
14.7770	9.6869
16.5321	10.7630
18.9640	12.2540
25.0000	15.9572
50.0000	31.2952

SHOCK SHAPES FOR EQUILIBRIUM FLIGHT CONDITIONS

CASE 7
H = 64.0 km (210 KFT)
V_∞ = 6.096 km/sec (2000 FPS)
θ_C = 30°
R_N = 0.3048 m (1 FT)

X/R_N	Y/R_N
- .0545	0.0
- .0458	.1407
- .0206	.2777
.0194	.4079
.0745	.5344
.1406	.6510
.2083	.7489
.2840	.8419
.3862	.9484
.4880	1.0392
.6719	1.1777
.8311	1.2804
1.0642	1.4080
1.3046	1.5450
1.5627	1.6837
1.8859	1.8583
2.0700	1.9618
2.3787	2.1416
2.6886	2.3280
3.0567	2.5550
3.3656	2.7464
3.7178	2.9639
4.1599	3.2356
4.6841	3.5556
5.1032	3.8113
5.6589	4.1513
6.4679	4.6485
7.3166	5.1725
8.4471	5.8713
9.3050	6.4014
10.5718	7.1841
12.0089	8.0725
13.4334	8.9537
14.9929	9.9187
16.8527	11.0705
18.8034	12.2783
20.7800	13.5021
23.1513	14.9706
25.0000	24.2967
50.0000	39.7872

CASE 8
H = 64.0 km (210 KFT)
V_∞ = 4.876 km/sec (16000 FPS)
θ_C = 30°
R_N = 0.3048 m (1 FT)

X/R_N	Y/R_N
- .0660	0.0
- .0582	.1354
- .0356	.2665
- .0016	.3853
.0682	.5497
.1371	.6687
.2089	.7695
.2875	.8631
.3928	.9705
.5062	1.0704
.6550	1.1845
.8222	1.2970
1.0354	1.4236
1.2502	1.5423
1.5067	1.6830
1.8183	1.8555
2.1900	2.0692
2.4752	2.2411
2.9573	2.5400
3.3230	2.7707
3.7167	3.0194
4.1208	3.2736
4.6327	3.5942
5.1722	3.9314
5.7603	4.2992
6.3447	4.6657
7.1589	5.1778
8.2918	5.8920
9.0241	6.3542
10.4709	7.2673
12.1225	8.3099
13.2740	9.0370
15.0744	10.1742
25.0000	16.4493
50.0000	32.2548

CASE 9
H = 76.2 km (250 KFT)
V_∞ = 7.315 km/sec (24000 FPS)
θ_C = 40°
R_N = 0.6096 m (2 FT)

X/R_N	Y/R_N
- .0447	0.0
- .0361	.1385
- .0111	.2728
.0288	.4008
.0816	.5209
.1468	.6346
.2196	.7379
.3015	.8348
.4080	.9411
.5300	1.0447
.6526	1.1423
.7743	1.2400
.9203	1.3617
1.0483	1.4738
1.1870	1.5978
1.3088	1.7078
1.4499	1.8346
1.6061	1.9739
1.7942	2.1405
2.0438	2.3616
2.3286	2.6155
2.6384	2.8932
2.0576	3.1800
3.3493	3.5319
3.8628	3.9930
4.3048	4.3901
4.9770	4.5994
5.2465	5.2373
5.9916	5.9081
6.8675	6.6968
25.0000	18.8369
50.0000	35.7452

SHOCK SHAPES FOR EQUILIBRIUM FLIGHT CONDITIONS

CASE 10

H = 70.1 km (230 KFT)
V_∞ = 7.315 km/sec (24000 FPS)
θ_C = 40°
R_N = 0.6096 m (2 FT)

X/R_N	Y/R_N
- .0463	0.0
- .0376	.1391
- .0125	.2740
.0276	.4027
.0806	.5230
.1476	.6397
.2125	.7324
.2946	.8312
.4021	.9399
.5263	1.0466
.6427	1.1392
.7798	1.2496
.9194	1.3656
1.0640	1.4921
1.2281	1.6392
1.4069	1.8009
1.5737	1.9504
1.7676	2.1231
1.9994	2.3291
2.2575	2.5594
2.5564	2.8343
2.9042	3.1410
3.2275	3.4327
3.6212	3.7870
4.0082	4.1360
4.4610	4.5445
4.8995	4.9397
5.4146	5.4051
5.9018	5.8452
6.2860	6.1921
6.6324	6.5048
25.0000	23.3361
50.0000	45.7870

CASE 11

H = 64.0 km (210 KFT)
V_∞ = 6.096 km/sec (20000 FPS
θ_C = 40°
R_N = 0.6096 m (2 FT)

X/R_N	Y/R_N
- .0545	0.0
- .0458	.1407
- .0206	.2777
.0194	.4079
.0745	.5344
.1406	.6510
.2083	.7484
.2840	.8419
.3862	.9484
.4881	1.0392
.6007	1.1297
.7136	1.2197
.8553	1.3342
1.0228	1.4754
1.1717	1.6064
1.3451	1.7625
1.5308	1.9310
1.7425	2.1221
1.9900	2.3444
2.2712	2.5971
2.4942	2.7981
2.6314	2.9222
2.7409	3.0214
2.8301	3.1624
3.0205	3.2755
3.2438	3.3476
3.3615	3.5855
3.4250	3.6433
3.6743	3.8699
3.7565	3.9526
4.0251	4.1889
15.0000	14.1980
25.0000	23.3185
50.0000	46.5317

CASE 12

H = 64.0 km (210 KFT)
V_∞ = 4.876 km/sec (16000 FPS)
θ_C = 40°
R_N = 0.6096 m (2 FT)

X/R_N	Y/R_N
- .0660	0.0
- .0582	.1354
- .0356	.2665
- .0016	.3853
.0682	.5497
.1371	.6687
.1992	.7570
.2718	.8458
.3566	.9359
.4639	1.0352
.5866	1.1357
.7279	1.2486
.8779	1.3705
1.0568	1.5233
1.2206	1.6694
1.3202	1.7598
1.5208	1.9430
1.7904	2.1878
1.9977	2.3750
2.2024	2.5599
2.4456	2.7802
2.7008	3.0123
3.0364	3.3186
3.4517	3.6985
3.7852	4.0037
4.3357	4.5076
5.0088	5.1241
5.8292	5.8763
6.8204	6.7859
7.5928	7.4949
8.4465	8.2786
9.3960	9.1505
15.0000	14.2987
25.0000	23.4854
50.0000	46.4521

SHOCK SHAPES FOR EQUILIBRIUM FLIGHT CONDITIONS

CASE 13
H = 76.2 km (250 KFT)
V_∞ = 7.315 km/sec (24000 FPS)
θ_C = 40°
R_N = 0.3048 m (1 FT)

X/R_N	Y/R_N
- .0447	0.0
- .0361	.1385
- .0111	.2728
.0288	.4008
.0816	.5209
.1468	.6346
.2196	.7379
.3015	.8348
.4080	.9411
.5300	1.0447
.6526	1.1423
.7743	1.2400
.9203	1.3617
1.0483	1.4738
1.1870	1.5978
1.3088	1.7078
1.4499	1.8346
1.6061	1.9739
1.7942	2.1405
2.0438	2.3616
2.3286	2.6155
2.6384	2.8932
2.9576	3.1800
3.3493	3.5319
3.8628	3.9930
4.3048	4.3901
4.9770	4.5994
5.2465	5.2373
5.9916	5.9081
6.8675	6.6968
25.0000	18.8369
50.0000	35.7452

CASE 14
H = 70.1 km (230 KFT)
V_∞ = 7.315 km/sec (24000 FPS)
θ_C = 40°
R_N = 0.3048 m (1 FT)

X/R_N	Y/R_N
- .0463	0.0
- .0376	.1391
- .0125	.2740
.0276	.4027
.0806	.5230
.1476	.6397
.2125	.7324
.2946	.8312
.4021	.9399
.5263	1.0466
.6427	1.1392
.7798	1.2496
.9194	1.3656
1.0640	1.4921
1.2281	1.6392
1.4069	1.8009
1.5737	1.9504
1.7676	2.1231
1.9994	2.3291
2.2575	2.5594
2.5564	2.8343
2.9042	3.1410
3.2275	3.4327
3.6212	3.7870
4.0082	4.1360
4.6510	4.5445
4.8995	4.9397
5.4146	5.4051
5.9018	5.8452
6.2860	6.1921
6.6324	6.5048
25.0000	23.3361
50.0000	45.7870

CASE 15
H = 64.0 km (210 KFT)
V_∞ = 6.096 km/sec (20000 FPS)
θ_C = 40°
R_N = 0.3048 m (1 FT)

X/R_N	Y/R_N
- .0545	0.0
- .0458	.1407
- .0206	.2777
.0194	.4079
.0745	.5344
.1406	.6510
.2083	.7484
.2840	.8419
.3862	.9484
.4881	1.0392
.6007	1.1297
.7136	1.2197
.8553	1.3342
1.0228	1.4754
1.1717	1.6064
1.3451	1.7625
1.5308	1.9310
1.7425	2.1221
1.9900	2.3444
2.2712	2.5971
2.4942	2.7981
2.6314	2.9222
2.7409	3.0214
2.8301	3.1624
3.0205	3.2755
3.2438	3.3476
3.3615	3.5855
3.4250	3.6433
3.6743	3.8699
3.7565	3.9526
4.0251	4.1889
15.0000	14.1980
25.0000	23.3185
50.0000	46.5317

SHOCK SHAPES FOR EQUILIBRIUM FLIGHT CONDITIONS

CASE 16
H = 64.0 km (210 KFT)
V_∞ = 4.876 km/sec (16000 FPS)
θ_C = 40°
R_N = 0.3048 m (1 FT)

X/R_N	Y/R_N
- .0660	0.0
- .0582	.1354
- .0356	.2665
- .0016	.3853
.0682	.5497
.1371	.6687
.1992	.7570
.2718	.8458
.3566	.9359
.4639	1.0352
.5866	1.1357
.7279	1.2486
.8779	1.3705
1.0568	1.5233
1.2206	1.6694
1.3202	1.7598
1.5208	1.9430
1.7904	2.1878
1.9977	2.3750
2.2024	2.5599
2.4456	2.7802
2.7008	3.0123
3.0364	3.3186
3.4517	3.6985
3.7852	4.0037
4.3357	4.5076
5.0088	5.1241
5.8292	5.8763
6,8204	6.7859
7.5928	7.4949
8.4465	8.2786
9.3960	9.1505
15.0000	14.2987
25.0000	23.4854
50.0000	46.5121

SHOCK SHAPES FOR WIND TUNNEL CASES

AIR
γ = 1.4
M = 8.0
T_t = 810° K (1460° R)
θ_C = 30°

X/R_N	Y/R_N
- .1397	0.0
- .1371	.0821
- .0994	.3256
- .0521	.4775
.0098	.6201
.0832	.7517
.1420	.8409
.2236	.9482
.3053	1.0426
.3981	1.1380
.5354	1.2630
.7131	1.4043
.8772	1.5203
1.1087	1.6670
1.2755	1.7637
1.5302	1.9089
1.8123	2.0713
2.1101	2.2943
2.5548	2.5075
2.9100	2.7250
3.3023	2.9739
3.6659	3.2097
4.1641	3.5390
4.6405	3.8577
5.1482	4.1992
5.6235	4.5192
6.1729	4.8892
6.6951	5.2411
7.2950	5.6453
8.0244	6.1370
8.8061	6.6644
9.5075	7.1380
10.5053	7.8124
11.8646	8.7319
13.5593	9.8793
25.0000	17.6358
50.0000	34.5853

AIR
γ = 1.4
M = 8.0
T_t = 810° K (1460° R)
θ_C = 40°

X/R_N	Y/R_N
- .1397	0.0
- .1371	.0821
- .0994	.3256
- .0521	.4775
.0098	.6201
.0832	.7517
.1420	.8409
.2236	.9482
.3053	1.0426
.3980	1.1380
.5354	1.2630
.6804	1.3857
.8403	1.5255
1.0012	1.6699
1.1529	1.8101
1.3322	1.9820
1.5414	2.1876
1.7067	2.3526
1.9304	2.5779
2.1329	2.7828
2.4033	3.0571
2.6615	3.3196
2.9619	3.6255
3.2983	3.9687
3.6534	4.3315
4.0157	4.7020
4.3694	5.0640
4.7333	5.4367
5.2384	5.9544
5.7608	6.4901
6.3592	7.1037
7.2272	7.9941
8.0486	8.8369
9.0894	9.9047
10.6628	11.5196
12.3307	13.2327
25.0000	26.2415
50.0000	51.9115

SHOCK SHAPES FOR WIND TUNNEL CASES

N_2
$\gamma = 1.4$
$M = 20$
$T_t = 1645°$ K (2960° R)
$\theta_C^t = 30°$

X/R_N	Y/R_N
- .1303	0.0
- .1201	.1623
- .0904	.3200
- .0437	.4689
.0127	.6077
.0888	.7354
.1607	.8415
.2358	.9370
.3153	1.0262
.4244	1.1342
.5492	1.2426
.7112	1.3669
.9383	1.5185
1.1986	1.6698
1.4612	1.8141
1.7290	1.9621
2.0266	2.1274
2.3270	2.2969
2.7025	2.5145
3.0400	2.7190
3.3832	2.9324
3.8545	2.2330
4.3475	3.5531
4.8746	3.8975
5.3036	4.1780
5.7973	4.5005
6.4421	4.9214
7.0000	5.2854
7.6949	5.7392
8.5233	6.2280
9.5613	6.9608
10.9250	7.8519
12.1713	8.6736
13.8172	9.7542
15.4830	10.8487
25.0000	17.1085
50.0000	33.5522

N_2
$\gamma = 1.4$
$M = 20$
$T_t = 1645°$ K (2960° R)
$\theta_C^t = 40°$

X/R_N	Y/R_N
- .1303	0.0
- .1201	.1623
- .0904	.3200
- .0437	.4689
.0127	.6077
.0888	.7354
.1607	.8415
.2358	.9370
.3153	1.0262
.4244	1.1341
.5706	1.2601
.7193	1.3833
.8777	1.5182
1.0479	1.6672
1.2095	1.8142
1.3856	1.9800
1.5789	2.1661
1.7995	2.3818
1.9714	2.5508
2.2224	2.7981
2.3930	2.9664
2.6749	3.2451
3.0213	3.5881
3.3290	3.8935
3.6602	4.2226
3.9860	4.5467
4.3928	4.9519
4.8532	5.4107
5.3712	5.9270
5.9386	6.4931
6.5974	7.1506
7.4269	7.9786
8.2575	8.8377
9.3758	9.9245
10.4918	11.0397
12.0222	12.5645
14.3170	14.8616
25.0000	25.5285
50.0000	50.4910

SHOCK SHAPES FOR WIND TUNNEL CASES

He
$\gamma = 1.667$
$M = 20$
$T_t = 590°$ K (1060° R)
$\theta_C^t = 30°$

X/R_N	Y/R_N
- .198	0.0
- .1860	.1877
- .1503	.3697
- .0953	.5390
- .0260	.6929
.0517	.8295
.1115	.9190
.1873	1.0194
.3042	1.1539
.3987	1.2502
.5709	1.4050
.7067	1.5131
.9613	1.6934
1.2022	1.8438
1.4778	2.0002
1.8581	2.2205
2.2416	2.4485
2.5991	2.6654
3.0352	2.9375
3.4300	3.1935
3.9610	3.5500
4.5178	3.9337
5.7270	4.7839
6.6534	5.4400
7.7346	6.2066
8.7892	6.9546
9.9810	7.7998
10.8677	8.4288
12.1733	9.3551
13.4649	10.2716
14.8935	11.1285
16.7275	12.5868
25.0000	18.4600
50.0000	36.2092

He
$\gamma = 1.667$
$M = 20$
$T_t = 590°$ K (1060° R)
$\theta_C^t = 40°$

X/R_N	Y/R_N
- .1983	0.0
- .1860	.1877
- .1503	.3697
- .0953	.5390
.0260	.6929
.0517	.8295
.1115	.9190
.1873	1.0194
.2511	1.1022
.3700	1.2220
.5174	1.3593
.6674	1.4912
.8409	1.6541
1.0028	1.8115
1.1811	1.9911
1.3521	2.1702
1.5349	2.3667
1.5697	2.4046
1.7394	2.5905
1.8351	2.6961
1.9579	2.8323
2.0301	2.9127
2.1654	3.0638
2.2163	3.1208
2.3792	3.3033
2.4838	3.4207
2.5849	3.5340
2.8041	3.7809
3.0219	4.0263
3.3118	4.3528
3.5021	4.5673
3.6614	4.7546
15.0000	17.5218
25.0000	28.7818
50.0000	56.9318

SHOCK SHAPES FOR WIND TUNNEL CASES

CF_4
$\gamma = 1.12$
$M = 6.2$
$T_t = 700°$ K (1260° R)
$\theta_c^t = 30°$

X/R_N	Y/R_N
- .0644	0.0
- .0563	.1376
- .0328	.2717
.0055	.4004
.0590	.5235
.1205	.6409
.1892	.7441
.2650	.8406
.3518	.9356
.4580	1.0365
.6033	1.1558
.8203	1.3077
1.0214	1.4298
1.2754	1.5738
1.5958	1.7532
1.9800	1.9721
2.3269	2.1785
2.8282	2.4894
3.3341	2.8104
3.8610	3.1471
4.1851	3.3533
4.8173	3.7543
5.6746	4.2972
6.5427	4.8982
7.3142	5.3394
8.1843	5.8944
8.9572	6.3879
9.6248	6.8143
10.4689	7.3536
11.4652	7.9905
12.6996	8.7790
13.7795	9.4692
14.6425	10.0210
25.0000	16.6500
50.0000	32.8395

CF_4
$\gamma = 1.12$
$M = 6.2$
$T_t = 700°$ K (1260° R)
$\theta_c^t = 40°$

X/R_N	Y/R_N
- .0644	0.0
- .0563	.1376
- .0328	.2717
.0055	.4004
.0590	.5235
.1205	.6409
.1892	.7441
.2708	.8473
.3518	.9356
.4580	1.0365
.5829	1.1411
.7251	1.2574
.8770	1.3839
1.0461	1.5303
1.1909	1.6606
1.2588	1.7225
1.4465	1.8954
1.6765	2.1081
1.8767	2.2918
2.1420	2.5351
2.3801	2.7536
2.6737	3.0239
2.9859	3.3124
3.3710	3.6691
3.8531	4.1164
4.3365	4.5649
5.0283	5.2071
5.7925	5.9168
6.7783	6.8331
7.3547	7.3691
8.1977	8.1531
9.2193	9.1033
10.4557	10.7189
11.8195	11.5227
25.0000	23.7907
50.0000	47.0599

☆U.S. GOVERNMENT PRINTING OFFICE: 1975—635-048/62